

Philipp Ulbl, BSc

Effects of Resonant Magnetic Perturbations on the Suppression of Edge Localized Modes

MASTER'S THESIS

to achieve the university degree of
Diplom-Ingenieur

Master's degree programme: Technical Physics

submitted to

Graz University of Technology

Supervisor

Ass.Prof. Dipl.-Ing. Dr.techn. Winfried Kernbichler
Institute of Theoretical and Computational Physics

Co-Supervisor

Dipl.-Ing. Dr.rer.nat. Christopher Albert, BSc
Institute of Theoretical and Computational Physics
Max-Planck-Institut für Plasmaphysik, Garching

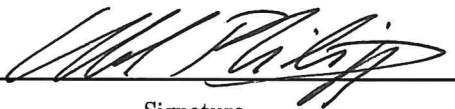
Graz, March 2020

Affidavit

I declare that I have authored this thesis independently, that I have not used other than the declared sources/resources, and that I have explicitly indicated all material which has been quoted either literally or by content from the sources used. The text document uploaded to TUGRAZonline is identical to the present master's thesis.

24.02.2020

Date



Signature

Abstract

The operational capability of future nuclear fusion experiments and reactors relies heavily on the durability of plasma facing components, especially the first wall and the divertor plates. Edge localized modes (ELMs) as seen in high confinement (H-mode) plasmas stress these components even further by applying large transient heat loads that are not tolerable in standard operation scenarios. Resonant magnetic perturbations (RMPs) have been successfully applied to reduce or even eliminate ELMs (mitigation, suppression) while maintaining the beneficial properties of H-mode. At small amplitudes RMPs are usually shielded by the plasma, whereas at larger amplitudes they undergo a bifurcation into an unshielded state where they significantly modify magnetic field topology. It is supposed that ELM mitigation and/or suppression occurs in this second state.

In this thesis, a quasilinear, kinetic estimation of the bifurcation threshold which accounts for mode coupling is presented. The interaction of RMPs with the plasma is covered on a basic level, especially the application of ideal MHD to RMPs, tearing mode theory and some properties of magnetic islands. The cylindrical MAXWELL solver KiLCA which takes kinetic plasma response into account is described and applied on test profiles. Finally, the physical and computational basics of the model as well as a qualitative explanation of bifurcation is presented.

The model is applied to selected ASDEX Upgrade shots, where indications are found that the difference between (1) ELM suppression, (2) ELM mitigation and (3) ELMy shots is due to the spatial location of particular resonant modes which enter a bifurcated state. These modes are: (1) modes on top of the pedestal, (2) modes further inside the plasma but still near the pedestal and (3) no bifurcated modes at all. Further, qualitative studies on the dependency of the bifurcation threshold on the form of the profiles and the amplitude of density and electron temperature are made.

Table of Contents

1	Introduction	8
1.1	High Confinement Mode	8
1.1.1	Edge Localized Modes	9
1.1.2	Resonant Magnetic Perturbations	10
1.2	Plasma Response to RMPs	14
1.2.1	Two-Fluid Estimation of the Shielding of RMPs	14
1.2.2	Physics of the Two-Fluid Estimation	16
1.2.3	Other Mechanisms of Bifurcation	16
1.3	Content of this Thesis	17
2	Linear Tearing Mode Theory	18
2.1	Ideal MHD Treatment	18
2.1.1	The Current Sheet	19
2.1.2	Normal Mode Analysis	20
2.1.3	Discontinuities	22
2.1.4	Solutions in the Outer Region	24
2.1.5	Application of a Toy Equilibrium	26
2.1.6	Magnetic Islands	29
2.1.7	Ideal Stability	32
2.2	Resistive MHD Treatment	35
2.2.1	Resistive Modifications	35
2.2.2	Discussion on the FKR Treatment	36
2.3	Summary on Tearing Mode Theory	37
2.4	More on Tearing Modes and Magnetic Island Growth	38
3	Linear Models in Cylindrical Approximation	40
3.1	Large Aspect Ratio Limit / Cylindrical Tokamak	40
3.2	Ideal MHD in the Cylindrical Tokamak	43
3.2.1	Cylindrical Equilibrium	43
3.2.2	Harmonic Perturbations	44
3.3	Kinetic Linear Model in Cylindrical Approximation	46
3.3.1	RMP Modelling	46
3.3.2	Vacuum Solutions	47
3.3.3	Kinetic Plasma Response	48
3.4	Application of KiLCA to a Test Case	50
3.4.1	Profiles & Equilibrium	50

3.4.2	Vacuum Perturbations & Plasma Response	50
3.4.3	Analysis of Shielding in the Test Case	52
3.4.4	Poincaré Plots	56
4	Estimation of the Bifurcation Threshold	61
4.1	Physical Model	61
4.1.1	Transport Equations	61
4.1.2	How RMPs Cause Bifurcation	63
4.1.3	Bifurcation Threshold	63
4.2	Computational Model	65
4.2.1	Equilibrium Preprocessing	67
4.2.2	Profile Preprocessing	67
4.2.3	Accounting for Effects of Toroidal Geometry	71
4.2.4	Estimation of the Anomalous Diffusion Coefficient	72
4.3	Application on AUG Shots	74
4.3.1	Investigation of Bifurcation Thresholds	74
4.3.2	Effect of Different Profiles	78
4.3.3	Density Scaling	82
4.3.4	Combined Density and Electron Temperature Scaling	82
5	Conclusion	84
5.1	Summary	84
5.2	Discussion and Further Suggestions	85
	References	86

List of Abbreviations

Notation	Description
ASDEX	Axially Symmetric Divertor Experiment (predecessor of AUG).
AUG	ASDEX Upgrade tokamak in Garching, DE.
BC	Boundary Conditions.
CXRS	Charge Exchange Recombination Spectroscopy (Diagnostics).
DIII-D	Tokamak in San Diego, US.
ECRH	Electron Cyclotron Resonance Heating.
ELM	Edge Localized Mode.
EM	Electromagnetic.
FKR	The authors: Furth, Killeen and Rosenbluth.
FLRE	Finite Larmor Radius Expansion.
GR	The authors: Goldston and Rutherford.
H-mode	High confinement mode.
ICRH	Ion Cyclotron Resonance Heating.
ITER	Next level tokamak currently built in Cadarache, FR (iter = latin "the way").
JET	Joint European Torus tokamak in Culham, UK.
KiLCA	Kinetic Linear Cylindrical Approximation.
L-mode	Low confinement mode.
MHD	Magnetohydrodynamics (i...ideal, r...resistive).
NBI	Neutral Beam Injection.
ODE	Ordinary Differential Equation.
RMP	Resonant Magnetic Perturbation.

Chapter 1

Introduction

The future of nuclear fusion as an energy source strongly depends on the overall energy gain of the fusion reaction. By the extended¹ LAWSON criterion [1, 2], the *triple product* of temperature T , density n and energy confinement time τ_E must exceed a certain value to achieve a break even situation. For practical use this triple product must be even higher to get a net energy gain. However, it should not exceed the ignition criterion where the heating is self-sustained by the produced alpha particles to maintain better control of the reaction.

Temperature is implicitly determined by the fusion reaction itself, i.e. by the maximum of the reaction cross section. Density has operational limits due to magnetohydrodynamic instabilities² and further empirical limits linked to disruptions, for example the GREENWALD limit [3]. Thus, energy confinement time is the parameter to tune to achieve a net power gain. This quantity describes how well energy is confined in the system. The higher the energy confinement time, the longer the energy stays inside the plasma.

The most obvious way to increase τ_E is to increase the size of the configuration. This is why fusion devices get bigger and bigger, reaching their temporary maximum with ITER³. The major radius of this device is about twice the one of the JET tokamak (the largest experiment up to today) and should be the first to demonstrate the possibility of a net energy gain out of the fusion reaction [4].

1.1 High Confinement Mode

The discovery of the *High Confinement Mode* (H-mode) in Neutral Beam Injection (NBI) experiments [5] on the ASDEX tokamak provided a new possibility to increase τ_E . Previously (Low Confinement Mode), profiles⁴ of density or temperature decreased steadily from the core to the edge of the plasma (figure 1.1, blue curve). In H-mode (red), these profiles are “shifted upwards” (pedestal) resulting in steep gradients in the edge region. This can be seen as a transport barrier preventing transport from flattening the profiles again.

¹The original LAWSON criterion only considered the product of density and energy confinement time.

²Precisely it is pressure which is limited but due to the more or less fixed temperature ranges, it boils down to a limit for the density.

³Tokamak currently built in Cadarache, FR.

⁴Profile means a 1D representation of a quantity along a certain axis in the cross section of a device. For example, from the magnetic axis in the center to the separatrix (last closed flux surface) at the edge with an angle of $\theta = 0$ (see e.g. figure 3.1 in section 3.1 for a better geometrical view). Along these lines one can take the intersection with flux surfaces of the configuration as a *flux surface label* ρ (usually normalized flux).

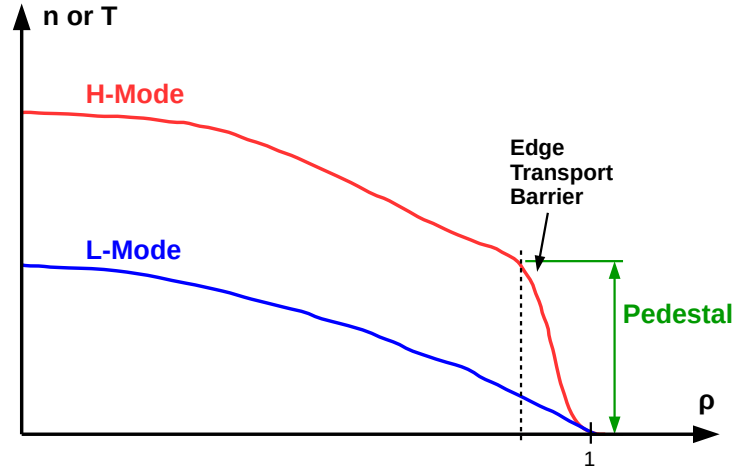


Figure 1.1. Profiles of density or temperature for L- and H-mode. L-mode is characterized by a steady decrease from the core to the edge. H-mode profiles are higher with a typical pedestal at the edge.

As implied by the name, H-mode plasmas have increased confinement time due to the edge transport barrier. Typically this is about twice as high as in L-mode. In the above context of power gain, this would mean a fair increase in performance. This is the reason why heavy research is undertaken to make H-mode the standard operational mode on future nuclear fusion reactors.

There are certain negative effects that accompany H-mode. For example, uncontrolled density increase, enhanced impurity confinement or decreased hydrogen recycling at the edge (\rightarrow α -particle build up in the core) [6]. To quote WESSON on the H-mode:

“The ultimate usefulness of the H-mode depends on whether the benefits of improved confinement can be achieved under controlled conditions without detrimental effects [...]”

1.1.1 Edge Localized Modes

Although the already mentioned problems of H-mode are crucial, there is one particular instability that is a possible game breaker. From the beginning of experiments the transition from L- to H-mode (short LH-transition) was accompanied by *Edge Localized Modes* (ELMs) [5]. These instabilities are characterized by periodic bursts that result in a degradation of confinement at the edge and consequently a reduction in density and temperature [6]. The exact cause of ELMs is not fully known but a magnetohydrodynamic origin is suspected [7].

One way to detect ELMs is the H_α -radiation⁵ emitted at the edge of the plasma. For deuterium plasmas one also calls this D_α -radiation. This radiation is (mostly) a result from core electrons travelling towards the edge and hitting neutral particles near the divertor plates [7]. During the event of an ELM, this radiation is increased greatly. A second way is to detect particles that are ejected towards the edge of the plasma. These will certainly hit the divertor plates or the first wall at some point. Increased heat loads result in a thermoelectric current in the divertor plates that can be taken as an indicator for ELMs [8]. Figure 1.2 shows both quantities, divertor current and D_α -radiation for an “ELMy” AUG (tokamak) shot.

⁵First spectral line in the BALMER series for hydrogen.

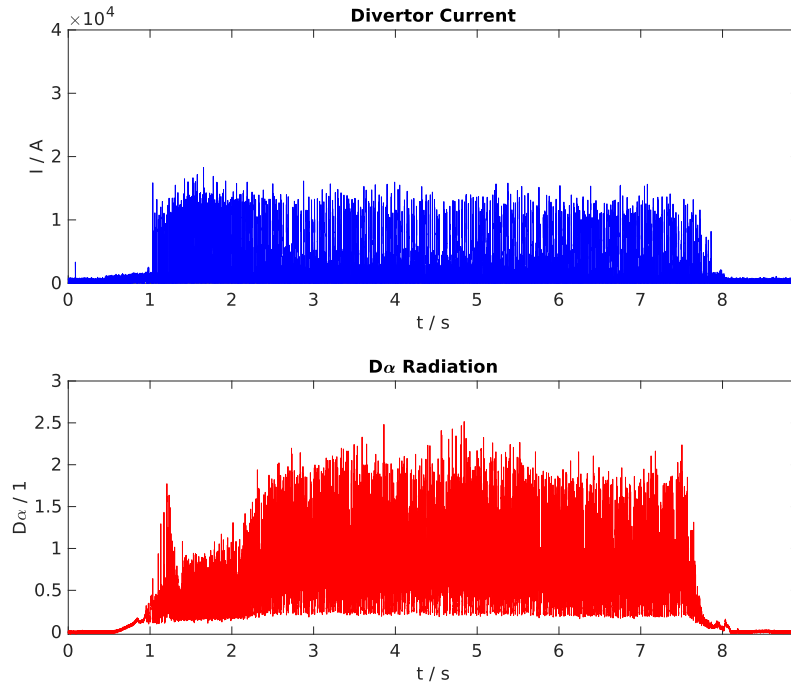


Figure 1.2. Divertor current and D_α -radiation for a typical ELMy AUG shot (33340). The LH-transition occurs at about 1s which can be seen from the onset of ELMs. Their burst-like structure results in the visible peaks.

The most problematic effect of ELMs is the large *transient* heat load released with each burst. For large ELMs this could be up 3 – 10% of the total plasma energy, released in few microseconds. The power load on the divertor of ITER can be estimated to be around $1 - 10 \text{ GW m}^{-2}$ whereas acceptable ones would be $1 - 3 \text{ GW m}^{-2}$ [9]. “Acceptable” hereby was taken to be about 3000 power cycles before a needed exchange of the divertor plates. This may be tolerable for experimental devices but for future nuclear fusion power plants this may not. Still, the expected heat load for ITER is too high, so there are two possibilities: Find another operational mode without ELMs (e.g. stay in L-mode) or try to mitigate or suppress ELMs (figure 1.3).

1.1.2 Resonant Magnetic Perturbations

One of the most promising ELM mitigation techniques are *Resonant Magnetic Perturbations* (RMPs). These *static* and *non-axisymmetric*, *small* perturbations are produced by an arrangement of toroidally distributed outer coils (called RMP or ELM coils) and are typically of the order $10^{-4} B_0$, where B_0 is the equilibrium field. For example the coil configuration for the AUG tokamak can be seen in figure 1.4. Non-axisymmetry is not only due to the discrete amount of coils in toroidal direction but furthermore due to different currents driven in each coil. An example can be seen in figure 1.5.

The effect of RMPs can be generally explained in simple terms. The magnetic field produced by the RMP coils penetrates into the plasma and hits *resonant surfaces*, located at positions where the plasma safety factor has rational numbers. This creates magnetic islands [10]. By choosing a specific magnetic field one can choose which resonances to stimulate. The safety factor profile is usually quite flat in the center of the plasma and diverges towards the last closed flux surface (separatrix). This means

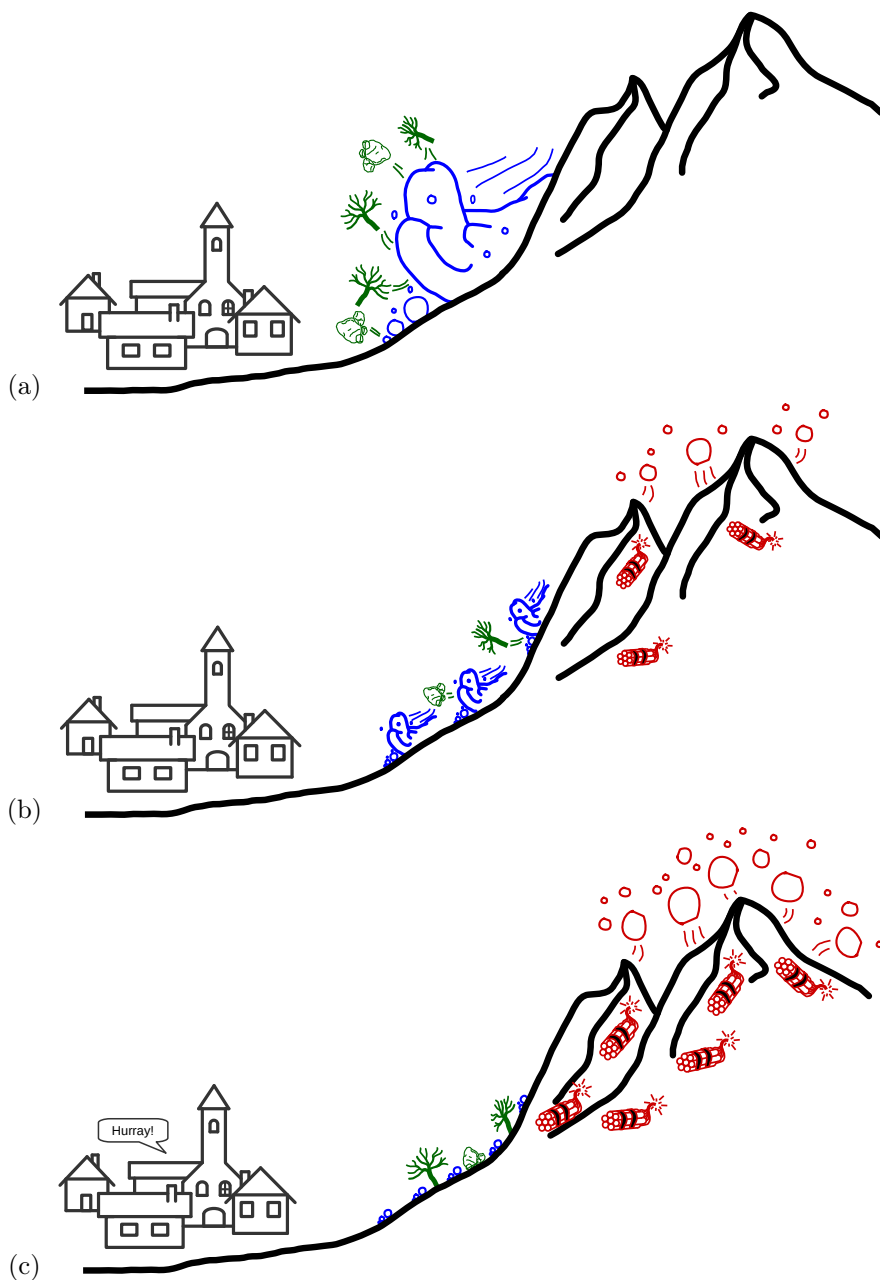


Figure 1.3. Cartoon to illustrate (a) ELMs, (b) ELM mitigation and (c) ELM suppression. ELMs can be viewed as avalanches (blue) that threaten a small mountain village (= first wall, divertor plates). Explosives (red) can trigger many smaller avalanches or no avalanches at all (= mitigation or suppression). The suppression could be anything, e.g. RMPs (section 1.1.2). Questions remain about the increased core impurity confinement (rubble, green) which is greatly reduced by ELMs and enhances overall performance. This would vanish together with suppressed ELMs.

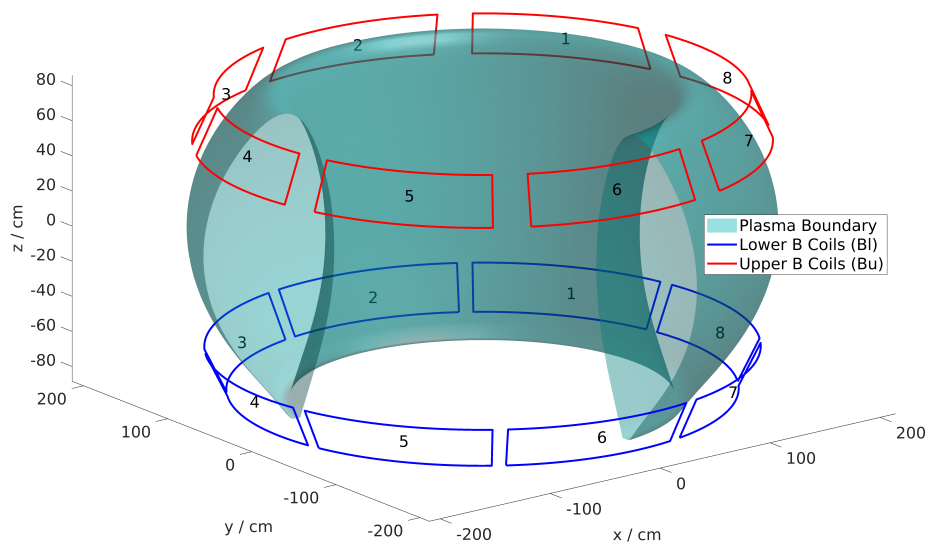


Figure 1.4. RMP coil configuration for the AUG tokamak. Shown are the upper and lower “B-coils” at their true position relative to the plasma boundary (last closed flux surface). The numbering of the coils is important as each one is driven with a different current in experiment.

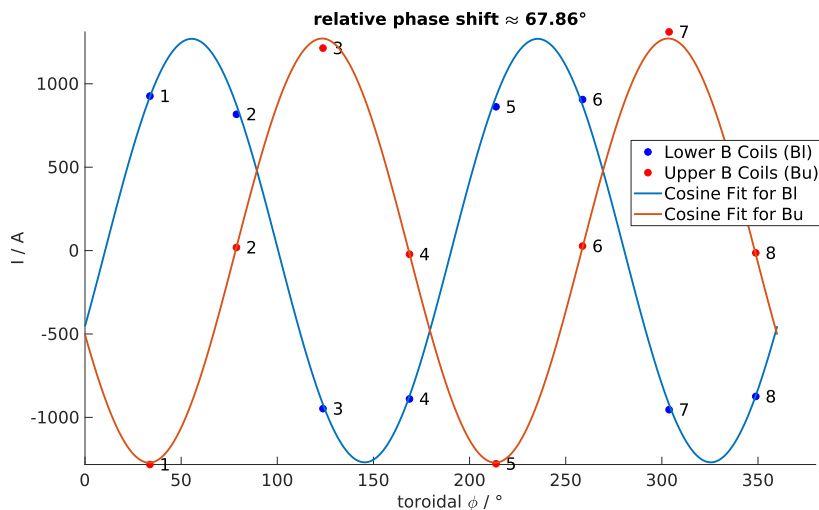


Figure 1.5. Example for currents driven in AUG B-coils in a typical ELM suppression experiment (shot 34548). The amplitude of the total current for each coil is plotted against the toroidal position of the center of the corresponding coil (points). Fits of cosines have been layed through the points to show the overall non-axisymmetric effect of the different coils with different currents. Note that in general there can be a phase shift between upper and lower coils.

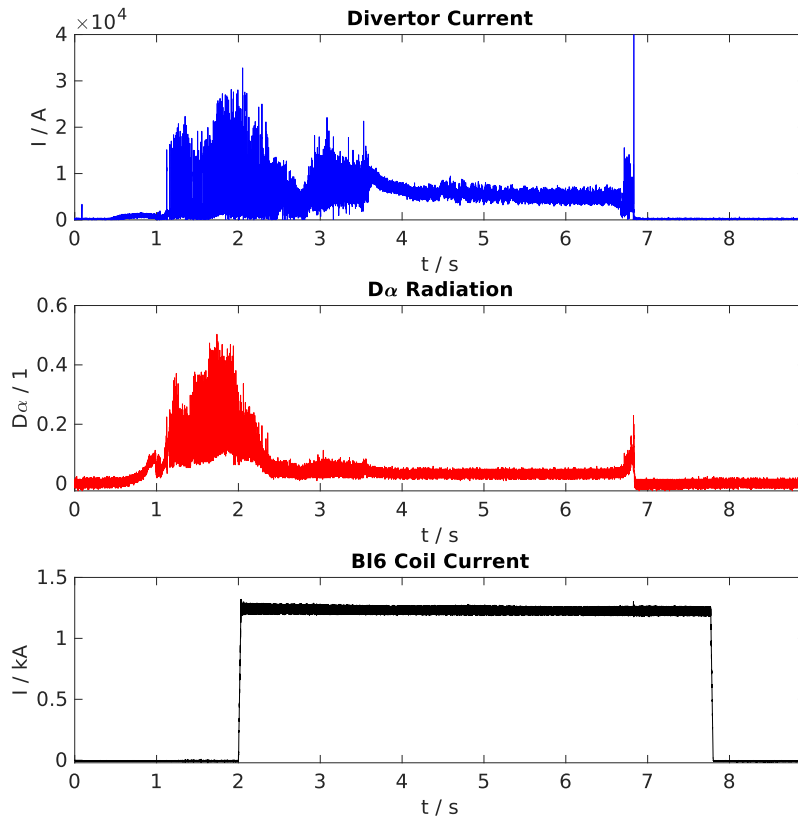


Figure 1.6. Divertor current, D_α -radiation and B16 coil current for a typical ELM suppression experiment on AUG (shot 33348). The RMP coils are switched on at about 2s. The ongoing ELMs (between 1s and 2s) are consequently suppressed which can be seen by the disappearance of spikes in the D_α -radiation.

that rational surfaces for higher safety factor are closer in space than ones for lower safety factor. Furthermore, resonances excited at the edge may lead to magnetic islands overlapping at some point which can be used to create a stochastic region at the edge of the plasma. The stochastic region was originally thought to cause ELM suppression or mitigation [11].

Experiments by EVANS, et al. [11, 12] have first shown the effectiveness of RMPs in terms of ELM suppression on the DIII-D tokamak. In favor for this technique was the fact that the transient ELM impurity transport was not completely lost but replaced by steady-state transport through the stochastic region at the edge⁶ whereas general properties of the density and temperature profiles remained. An example for ELM suppression can be seen in figure 1.6. In AUG, ELM mitigation was first seen in [13] and ELM suppression studies were summarized in [14]. The next section will deal with the implications of RMPs in more detail.

⁶Transport parallel to magnetic field lines is easy in contrast to perpendicular transport. Thus, a stochastic region replacing nested flux surfaces improves (radial) transport locally.

1.2 Plasma Response to RMPs

Plasma is a self-consistent medium which means that EM fields determine the motion of charged particles inside the plasma which in turn manifest themselves as currents that affect the EM fields. Upon applying RMPs, the expectation in vacuum would be the onset of large islands at the position of the corresponding resonant surface. The consideration of the plasma response to these external fields manifests itself in localized shielding currents that diminish the external perturbation inside the resonant surface and therefore the size of magnetic islands. In particular plasma rotation (or toroidal flow) has a crucial effect on this shielding [15, 16, 17].

Although the formation of magnetic islands will be suppressed for most resonant surfaces, there exist so-called *locked modes* which means that the RMP penetrates inside the plasma. These are characterized by the formation of magnetic islands (*full reconnection*). One speaks of bifurcated states, where there can be either locked modes or suppressed ones (*unreconnected state*). The transition between these states is called *bifurcation* [18].

Both, the bifurcation as well as the effect of plasma rotation has been in seen in experiments at the DIII-D tokamak [19].

1.2.1 Two-Fluid Estimation of the Shielding of RMPs

This simple model can be used to make qualitative explanations how the shielding current, produced by the plasma response to RMPs, affects the magnetic field perturbation itself. We start with the two-fluid momentum balance equation (e.g. [20])⁷,

$$m_\alpha n_\alpha [\partial_t \mathbf{v}_\alpha + (\mathbf{v}_\alpha \cdot \nabla) \mathbf{v}_\alpha] = n_\alpha q_\alpha (\mathbf{E} + \mathbf{v}_\alpha \times \mathbf{B}) - \nabla \cdot \mathbf{P}_\alpha + \sum_\beta \mathbf{R}_{\alpha\beta}, \quad (1.1)$$

where m and q denote mass and charge of the fluid elements, respectively. This equation describes the conservation of momentum for each particle species α (i.e. NEWTON'S 2nd law). On the left hand side we have inertial forces due to temporal or convective changes. On the right hand side we have forces acting on the fluids. From left to right these are the Lorentz force, internal forces described by the pressure tensor (pressure or viscosity) and a term which allows the momentum transfer from species α to species β .

For simplicity we neglect all inertial forces⁸ (left hand side = zero) and assume isotropic pressure without viscosity as well as an electrostatic field,

$$\mathbf{P}_\alpha = \mathbf{I} p_\alpha, \quad (1.2)$$

$$\mathbf{E} = -\nabla \Phi. \quad (1.3)$$

Thus, we get:

$$n_\alpha q_\alpha (-\nabla \Phi + \mathbf{v}_\alpha \times \mathbf{B}) - \nabla p_\alpha + \sum_\beta \mathbf{R}_{\alpha\beta} = 0. \quad (1.4)$$

Now we assume the plasma to be made of electrons and one species of ions. The term respecting transfer of momentum to electrons by electron-ion collisions can be written as [20]

⁷Units are SI or gaussian natural units.

⁸The convective term $(\mathbf{v} \cdot \nabla) \mathbf{v}$ can be estimated to be about 100 times smaller than the $\mathbf{v} \times \mathbf{B}$ term on the right and the explicit time derivative is even about 10^5 times smaller than the convective term.

$$\mathbf{R}_{ei} = -m_e n_e \nu_{ei} (\mathbf{v}_e - \mathbf{v}_i). \quad (1.5)$$

This momentum transfer is called friction force and scales with relative velocity $\mathbf{v}_e - \mathbf{v}_i$ and electron-ion collision frequency ν_{ei} .

The electron version of (1.4) is then:

$$-n_e e (-\nabla\Phi + \mathbf{v}_e \times \mathbf{B}) - \nabla p_e - m_e n_e \nu_{ei} (\mathbf{v}_e - \mathbf{v}_i) = 0. \quad (1.6)$$

We now write the magnetic field as an equilibrium field which we perturb externally,

$$\mathbf{B} = \mathbf{B}_0 + \tilde{\mathbf{B}}. \quad (1.7)$$

By multiplying (1.6) with \mathbf{B}_0 we can get rid of the gradient terms, since Φ and p_e are flux functions in 0th order (no perturbations), i.e. they are constant along a flux surface and thus, their gradient is perpendicular to the equilibrium field,

$$-n_e e \mathbf{B}_0 \cdot (\mathbf{v}_e \times \mathbf{B}) - m_e n_e \nu_{ei} \mathbf{B}_0 \cdot (\mathbf{v}_e - \mathbf{v}_i) = 0. \quad (1.8)$$

Evaluation of both terms individually yields

$$\mathbf{B}_0 \cdot (\mathbf{v}_e \times \mathbf{B}) = \mathbf{B}_0 \cdot \left(\mathbf{v}_e \times [\mathbf{B}_0 + \tilde{\mathbf{B}}] \right) = \tilde{\mathbf{B}} \cdot (\mathbf{B}_0 \times \mathbf{v}_e) = \tilde{\mathbf{B}} \cdot \mathbf{e}_r B_0 v_{e\perp} = \tilde{B}_r B_0 v_{e\perp},$$

$$\mathbf{B}_0 \cdot (\mathbf{v}_e - \mathbf{v}_i) = -\frac{1}{n_e e} \mathbf{B}_0 \cdot \mathbf{J} = -\frac{1}{n_e e} B_0 J_{\parallel},$$

where we used $\mathbf{J} = -n_e e (\mathbf{v}_e - \mathbf{v}_i)$ in the latter calculation. Finally we get

$$-n_e e \tilde{B}_r B_0 v_{e\perp} + m_e n_e \nu_{ei} \frac{1}{n_e e} B_0 J_{\parallel} = 0,$$

or

$$J_{\parallel} = \sigma v_{e\perp} \tilde{B}_r, \quad (1.9)$$

$$\sigma = \frac{n_e e^2}{m_e \nu_{ei}}. \quad (1.10)$$

This equation links the parallel plasma response current to the radial perturbed magnetic field via the SPITZER conductivity σ and the perpendicular electron flow velocity. Temperature dependence enters through the collision frequency, whereas density dependence will drop out since $\nu_{ei} \sim n_e T_e^{-3/2} \ln \Lambda$ (where the COULOMB logarithm $\ln \Lambda \approx \text{const.}$) [20]. We can clearly see that for lower temperatures the parallel current will decrease for fixed velocity and magnetic field perturbation.

1.2.2 Physics of the Two-Fluid Estimation

Now we can make a qualitative physical picture of the effect of RMPs on the plasma. The radial magnetic field perturbation from an RMP (which is driven by a current in the RMP coil) will produce a parallel current in the resonant layer (due to plasma response). This parallel current creates a magnetic field counteracting the external perturbation, thus annihilating the effect at the resonant surface and further inside the plasma (*shielding*). Due to 1.9, the parallel current diminishes its own driving mechanism but only to the point where it can be sustained by a very small magnetic field perturbation due to the generally high conductivity inside the plasma.

There are two general mechanisms that weaken shielding. First, the temperature drop at the edge will lead to increased collisionality and further to decreased conductivity (as mentioned before). Second, at locations where the perpendicular electron flow direction changes (sign change, $v_{e\perp} = 0$), the shielding current will become zero at all. This is called *fluid resonance*⁹. The screening of RMPs by flows as well as the simple picture derived above has been treated in [22].

The whole analysis of section 1.2.1 is only valid at the resonant surface because only there the parallel current can be constant along a field line (divergence-freeness can be fulfilled). Away from the resonant surface, the perturbations in the electrostatic potential will become too large to be neglected. The resulting parallel electric field will counteract the magnetic part of the LORENTZ force, thus preventing the occurrence of a parallel current.

1.2.3 Other Mechanisms of Bifurcation

In our two-fluid estimation we discovered the fluid resonance, where the perpendicular electron flow velocity was zero. We can decompose $v_{e\perp}$ into the electron diamagnetic velocity v_{ed} ¹⁰ and the $E \times B$ drift velocity,

$$v_{e\perp} = v_{ed} + v_{E \times B}, \quad (1.11)$$

$$v_{ed} = \frac{c}{enB} \partial_r p_e, \quad (1.12)$$

$$v_{E \times B} = \frac{cE_r}{B}, \quad (1.13)$$

to write the fluid resonance as the criterion

$$v_{E \times B} = -v_{ed}. \quad (1.14)$$

In the early investigations of [15] as well as in newer models [21] there appears a second resonance¹¹ at the point where the $E \times B$ drift velocity has a zero,

$$v_{E \times B} = 0. \quad (1.15)$$

In other words, the zero of the radial electric field E_r may be a crucial point when investigating the bifurcation point.

⁹A linear kinetic treatment (like in [21] but in first order) will result in a slight shift of the fluid resonance away from the point in two-fluid theory.

¹⁰Sometimes in literature this is also written as v_{e*} .

¹¹In the fluid theory of R. FITZPATRICK [15], also a third resonance was seen at the point where the ion perpendicular velocity was zero. This was not seen in investigations with the kinetic code KiLCA (private communication with S. V. KASILOV in 2020).

1.3 Content of this Thesis

In chapter 2 we investigate the effect of a sheet current in the framework of ideal magnetohydrodynamics in simple slab geometry. This is way simpler than the two-fluid estimation from above and it may become apparent that the model cannot handle currents that are concentrated in such narrow regions as resonant layers are. The effect of resistivity will “heal” the problems of the ideal model which results in the growth of magnetic islands at the location of the current sheet. This chapter only treats the effect of internal current sheets that may arise due to instabilities (tearing modes).

Chapter 3 will move on to more realistic geometry, i.e. the large aspect ratio approximation of a tokamak. In this geometry, the equilibrium will be shortly analyzed, as well as the effect of an external vacuum perturbation. For the plasma response the MAXWELL solver KiLCA will be used to demonstrate the effect of a kinetic plasma response.

A quasilinear estimation of the bifurcation threshold for RMPs will be given in chapter 4. It will describe the physical and computational model based on earlier work [21] and the improvements made in the scope of this thesis. It will include an application to experiments on the AUG tokamak and will investigate the effect of density and electron temperature on this threshold.

Finally, chapter 5 will try to link all topics presented here together and summarize each chapter individually. For the application on experiment, conclusions and suggestions for further improvements will be given.

Chapter 2

Linear Tearing Mode Theory

The aim of this chapter is to understand how the model called *magnetohydrodynamics* or MHD treats the occurrence of sheet-currents that flow only in a single, narrow region around some surface. Initially this was done by Furth, Killeen and Rosenbluth (FKR) [23] in a treatment including plasma resistivity. However, we will start with an ideal static equilibrium, analyze it rigorously and move further in complexity by including dynamics. In the end the effects of resistivity will be touched.

2.1 Ideal MHD Treatment

The model we use is commonly known as iMHD and essentially describes the plasma as a charged single particle species fluid with zero resistivity. The system of 15 iMHD equations is given by (see e.g. [24]):

$$\frac{\partial \rho}{\partial t} + \nabla \cdot (\rho \mathbf{v}) = 0, \quad (2.1)$$

$$\rho \frac{d\mathbf{v}}{dt} - \mathbf{J} \times \mathbf{B} + \nabla p = 0, \quad (2.2)$$

$$\frac{d}{dt} \left(\frac{p}{\rho^\gamma} \right) = 0, \quad (2.3)$$

$$\nabla \times \mathbf{E} + \frac{\partial \mathbf{B}}{\partial t} = 0, \quad (2.4)$$

$$\nabla \times \mathbf{B} - 4\pi \mathbf{J} = 0, \quad (2.5)$$

$$\nabla \cdot \mathbf{B} = 0, \quad (2.6)$$

$$\mathbf{E} + \mathbf{v} \times \mathbf{B} = 0. \quad (2.7)$$

The set of equations consists of two conservation laws for mass and momentum (from fluid mechanics), the energy equation (adiabatic evolution with $\gamma = 5/3$), three of the low-frequency MAXWELL equations and ideal OHM's law (in the limit of zero resistivity). The corresponding quantities are the mass density ρ , flow velocity \mathbf{v} , scalar pressure p , current density \mathbf{J} , electric field \mathbf{E} and magnetic field \mathbf{B} . *Gaussian* units with $c \equiv 1$ were chosen.

For now we will assume a static equilibrium where we can set time derivatives to zero. Thus, the only interesting equations left are (2.6), (2.5) and (2.7) which can be combined to

$$\nabla p = \mathbf{J} \times \mathbf{B} = \frac{1}{4\pi} (\nabla \times \mathbf{B}) \times \mathbf{B} = \frac{1}{4\pi} \left[(\mathbf{B} \cdot \nabla) \mathbf{B} - \frac{1}{2} \nabla B^2 \right]. \quad (2.8)$$

This equation is the *static pressure balance*. The last equality sign used a standard decomposition into magnetic tension and magnetic pressure given by simple vector identities¹.

2.1.1 The Current Sheet

The configuration we are interested in is given in figure 2.1. The equilibrium magnetic field has a y -component pointing towards positive y -direction on the side $x > x_0$ and vice-versa on the other side. Without loss of generality we can set $x_0 \equiv 0$. Additionally we can include a field component in z -direction. Thus we have

$$\mathbf{B}_0 = B_{0y}(x) \mathbf{e}_y + B_{0z}(x) \mathbf{e}_z. \quad (2.9)$$

AMPÈRES law (2.5) gives rise to a current²,

$$4\pi \mathbf{J}_0 = -\partial_x B_{0z} \mathbf{e}_y + \partial_x B_{0y} \mathbf{e}_z. \quad (2.10)$$

By momentarily setting the z -component of the equilibrium field to zero we can make the following inference: The equilibrium field as given in figure 2.1 is equally strong on both sides³ but differently directed. Thus we can think of it as a HEAVISIDE theta function. The current in z -direction is then given as the derivative of this which can be viewed as a DIRAC delta distribution. This means, the current is only located on the sheet-like layer $x = 0$ which separates the left and right region. The name *Current Sheet* is now apparent. In reality the field will not look like a HEAVISIDE theta function but differently. Still, the form will be similar in the way that the equilibrium field will be almost constant outside a narrow region around $x = 0$ and the difference will only imply a broadening of the current profile. We will then say the current is concentrated around the sheet-like layer.

Back to the general equilibrium field, the last quantity left in the iMHD equations is the equilibrium pressure which can be easily calculated using (2.8)

$$4\pi \partial_x p_0 = -\frac{1}{2} \partial_x B_0^2. \quad (2.11)$$

Now we finished analyzing the equilibrium and will move on with stability considerations.

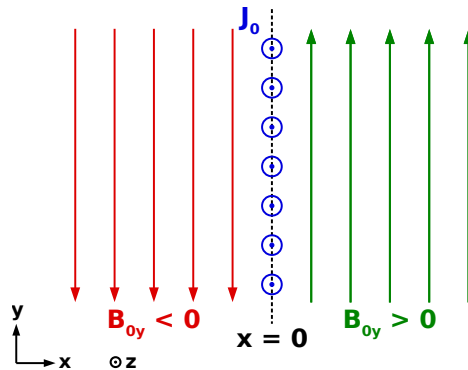


Figure 2.1. Sketch of the current sheet configuration. Only the y -component of the equilibrium field and the z -component of the equilibrium current is displayed.

¹One can find a summary of basically all needed identities for plasma physics in [25]

²I will use the notation $\partial_x \equiv \partial/\partial x$ for the rest of this work.

³The field strength B_{0y} is the density of field lines that point in y -direction which is uniform in figure 2.1.

2.1.2 Normal Mode Analysis

Since the equilibrium is fully known, the next logical step is to figure out if it is stable or not, or to be precise, at which conditions it is stable or not. However, we are merely interested in the form of perturbations rather than the stability of the equilibrium. No matter what aim our analysis has, we can use a common technique in the MHD framework. We apply small perturbations which are assumed to add up linearly to the equilibrium,

$$\mathbf{B} = \mathbf{B}_0 + \delta\mathbf{B}, \quad (2.12)$$

$$p = p_0 + \delta p. \quad (2.13)$$

Because of this, we can always cancel out the equilibrium-only quantities by applying this form to the MHD equations. We will also neglect terms of second order or higher. As an example, we can look at the right side of the static pressure balance (2.8):

$$\begin{aligned} (\mathbf{B} \cdot \nabla) \mathbf{B} - \frac{1}{2} \nabla B^2 &= \underbrace{(\mathbf{B}_0 \cdot \nabla) \mathbf{B}_0 - \frac{1}{2} \nabla B_0^2}_{\text{part of equilibrium eq.}} \\ &+ (\mathbf{B}_0 \cdot \nabla) \delta\mathbf{B} - \frac{1}{2} \nabla (\mathbf{B}_0 \cdot \delta\mathbf{B}) + (\delta\mathbf{B} \cdot \nabla) \mathbf{B}_0 - \frac{1}{2} \nabla (\delta\mathbf{B} \cdot \mathbf{B}_0), \\ &\underbrace{+ (\delta\mathbf{B} \cdot \nabla) \delta\mathbf{B} - \frac{1}{2} \nabla \delta B^2}_{\mathcal{O}(\delta^2)}. \end{aligned}$$

Only the second line will be used in the perturbed version of the initial equation. We assume the form of these perturbations to be described by FOURIER modes containing no time dependence (since we already restricted ourselves to make a static analysis using (2.8)),

$$\delta\mathbf{B} = \tilde{\mathbf{B}}(x) e^{i\mathbf{k} \cdot \mathbf{r}}, \quad (2.14)$$

$$\delta p = \tilde{p}(x) e^{i\mathbf{k} \cdot \mathbf{r}}, \quad (2.15)$$

$$\mathbf{k} = k_y \mathbf{e}_y + k_z \mathbf{e}_z, \quad (2.16)$$

were $\mathbf{r} = x\mathbf{e}_x + y\mathbf{e}_y + z\mathbf{e}_z$ is the position vector. We already used the symmetry of the current sheet configuration, as we wrote the perturbation only to depend on the x -direction. The modes correspondingly evolve in the yz -direction. The quantity \mathbf{k} is referred to as the wave-vector, although the perturbation does not have to form waves necessarily. It rather describes spatial periodicity of *any* perturbation. By taking typical scale lengths of the configuration, one can connect this to integer mode numbers

$$k_y = \frac{m}{L_y}, \quad k_z = \frac{n}{L_z}. \quad (2.17)$$

Since the dimensions of the current sheet are considered to be infinite we will not need this integer mode numbers here. Nevertheless, they will become important in the discussion of real geometries which represent systems of finite size e.g. slab-like, cylindrical or toroidal ones.

Going back to the application of small perturbations in the form of normal modes, the static force balance (2.8) becomes

$$4\pi (-i\partial_x \tilde{p} \mathbf{e}_x + \mathbf{k} \tilde{p}) = F \tilde{\mathbf{B}} - i \tilde{B}_x \partial_x \mathbf{B}_0 + i \partial_x (\mathbf{B}_0 \cdot \tilde{\mathbf{B}}) \mathbf{e}_x - \mathbf{k} (\mathbf{B}_0 \cdot \tilde{\mathbf{B}}). \quad (2.18)$$

We already used the form of the equilibrium given by (2.9) and introduced the quantity⁴

$$F := \mathbf{k} \cdot \mathbf{B}_0 = \mathbf{k} \cdot \hat{\mathbf{b}}_0 B_0 = k_{\parallel} B_0. \quad (2.19)$$

Note that the exponential of our FOURIER mode assumption gives rise to the factor of $i\mathbf{k}$ (derivative) and can be canceled afterwards because it appears in every term. The second equation we need, is the divergence-freeness of the perturbation,

$$\nabla \cdot \delta \mathbf{B} = 0. \quad (2.20)$$

Now we take the x -component of the perturbed pressure balance (2.18) and the scalar product of it with \mathbf{k} . We write both equations together with the explicit form of (2.20) to arrive at the central set of equations for this problem:

$$\partial_x \left(4\pi \tilde{p} + \mathbf{B}_0 \cdot \tilde{\mathbf{B}} \right) = iF \tilde{B}_x, \quad (2.21)$$

$$k^2 \left(4\pi \tilde{p} + \mathbf{B}_0 \cdot \tilde{\mathbf{B}} \right) = F \left(\mathbf{k} \cdot \tilde{\mathbf{B}} \right) - i\tilde{B}_x \partial_x F, \quad (2.22)$$

$$\partial_x \tilde{B}_x + i\mathbf{k} \cdot \tilde{\mathbf{B}} = 0. \quad (2.23)$$

We get an additional equation by taking the scalar product of \mathbf{B}_0 with the perturbed pressure balance(2.18),

$$4\pi F \tilde{p} = -i\tilde{B}_x \frac{1}{2} \partial_x^2 B_0^2. \quad (2.24)$$

This set of equations can be solved for the three components of the perturbed field⁵.

First, we substitute (2.23) into (2.22) and the result into (2.21) to get

$$\partial_x^2 \tilde{B}_x - \tilde{B}_x \left(k^2 + \frac{\partial_x^2 F}{F} \right) = 0. \quad (2.25)$$

By using the equilibrium pressure balance (2.11) in our fourth equation (2.24), we can relate the perturbed and equilibrium pressure by $F\tilde{p} = i\tilde{B}_x \partial_x p_0$. Inserted in (2.22) and further substituted together with (2.23) in (2.21) this leads to

$$\tilde{B}_z = \frac{ik_z \partial_x \tilde{B}_x}{k^2} - \frac{ik_y \tilde{B}_x}{\{\mathbf{k} \times \mathbf{B}_0\}_x} \left(\frac{\partial_x F}{k^2} + \frac{4\pi \partial_x p_0}{F} \right). \quad (2.26)$$

Now we got an ODE for \tilde{B}_x which upon solving defines \tilde{B}_z . The missing component is \tilde{B}_y which can be simply calculated using the perturbed divergence-freeness (2.20),

$$k_y \tilde{B}_y = i\partial_x \tilde{B}_x - k_z \tilde{B}_z. \quad (2.27)$$

If we look closely at these equations we can identify \tilde{B}_x to be purely real and \tilde{B}_y and \tilde{B}_z to be purely imaginary. For FOURIER amplitudes this means a phase shift of π between the components.

⁴This is the projection of the perturbation parallel to the equilibrium field.

⁵This also holds for the perturbed pressure which we are not interested in here.

2.1.3 Discontinuities

As has been shown in the previous section, the calculation of the perturbed magnetic field is more or less reduced to the solution of (2.25). Even without a rigorous mathematical analysis of this equation we can see that this equation does not have to necessarily behave well everywhere in x . Since the quantity

$$F = \mathbf{k} \cdot \mathbf{B}_0 = k_y B_{0y} + k_z B_{0z}, \quad (2.28)$$

appears in the denominator we encounter singularities everywhere, where $F = 0$. Now thinking back of the initial discussion of the current sheet, we can once again momentarily set the z -component of the equilibrium field to zero. The problem is now apparent: since B_{0y} points in different directions on both sides of the sheet-like layer, there must be a zero exactly at this plane $x = 0$. The singularity occurs at this point and our equation (2.25) *breaks down*. For the rest of the work we want to keep this case, thus we assume the other term $k_z B_{0z}$ to shift the functional form of F but not destroy the appearance of the singularity (the x -value where this occurs will then shift). The result: we have to concede with our use of iMHD.

We can still do some kind of restricted analysis, since we do not have singularities everywhere, instead only at one point in x . We can avoid facing this by restricting our domain to $x \in (0^\pm, \pm\infty)$. In this so called *Outer Region* we can apply our iMHD model, whereas in the other part or *Inner Region*, we have to find more suitable equations describing our configuration.

Since we split our domain into two distinct areas with two distinct solutions, we will later have to think about how to glue these two together at the boundaries. We can derive some general properties of the solutions by considering two small scenarios around the sheet-like layer which were done by Goldston and Rutherford (GR) in their book[20].

We can integrate the divergence-freeness (2.23) over the volume of a small box with size $x \in [0^-, 0^+]$, $y \in [y_1, y_2]$ and $z \in [z_1, z_2]$ centered around the sheet-like layer and apply GAUSS' theorem,

$$\int_{V_{\text{Box}}} \nabla \cdot \tilde{\mathbf{B}} dV = \oint_{S=\partial V_{\text{Box}}} \tilde{\mathbf{B}} \cdot \mathbf{nd}S = 0. \quad (2.29)$$

The margins $y_{1,2}$ and $z_{1,2}$ can be chosen arbitrarily, with $\Delta y = y_2 - y_1$ and $\Delta z = z_2 - z_1$. The closed surface integral can be evaluated as a sum of integrals over the six enclosing surface planes (because it is a box). The three positive directed ones are given in figure 2.2. As a result of the components of the perturbed field to only have spatial dependence in x , this evaluates to

$$\begin{aligned} \oint_S \tilde{\mathbf{B}} \cdot \mathbf{nd}S &= \sum_i \oint_{S_i} \tilde{\mathbf{B}} \cdot \mathbf{n}_i dS_i, \\ &= \Delta z \Delta y \left[\tilde{B}_x(0^+) - \tilde{B}_x(0^-) \right], \end{aligned} \quad (2.30)$$

or with (2.29):

$$\tilde{B}_x(0^+) = \tilde{B}_x(0^-). \quad (2.31)$$

This means that the x -component of the perturbed field is *continuous* at the sheet-like layer.

In the second consideration we integrate the perturbed current density $4\pi\tilde{\mathbf{J}} = \nabla \times \tilde{\mathbf{B}}$ over the xy -plane. The left side yields the total current in z -direction,

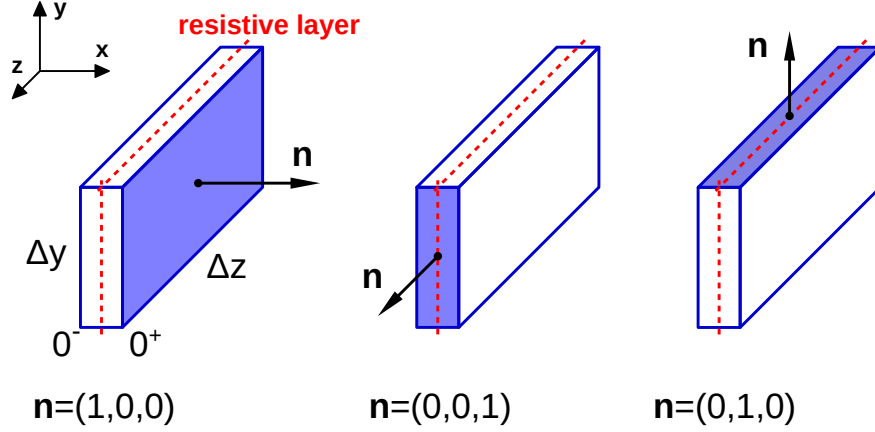


Figure 2.2. Positive oriented surfaces on the specified box around the sheet-like layer.

$$\iint_S \mathbf{dS} \cdot \tilde{\mathbf{J}} = \tilde{I}_z. \quad (2.32)$$

On the other hand, we get a contour integral using STOKES' theorem,

$$\iint_S \mathbf{dS} \cdot \nabla \times \tilde{\mathbf{B}} = \oint_{C=\partial S} \mathbf{ds} \cdot \tilde{\mathbf{B}}. \quad (2.33)$$

Again, this can be split into different parts now given by the contours in figure 2.3. Our special configuration leads to similar results as above:

$$\begin{aligned} \oint_C \mathbf{ds} \cdot \tilde{\mathbf{B}} &= \sum_i \oint_{C_i} \tilde{\mathbf{B}} \cdot \mathbf{ds}_i, \\ &= \Delta y \left[\tilde{B}_y(0^+) - \tilde{B}_y(0^-) \right]. \end{aligned} \quad (2.34)$$

Further, because this time the left side of the equation is *non-zero*, we have

$$\tilde{B}_y(0^+) - \tilde{B}_y(0^-) = \frac{4\pi\tilde{I}_z}{\Delta y}. \quad (2.35)$$

This means there is a *discontinuity* in the y -component of the perturbed field, that can be associated with the total current in z -direction. This current is located in a thin region around the sheet-like layer and therefore called a *surface current*⁶.

Because the divergence-freeness of the magnetic field (2.23) relates the x -derivative of \tilde{B}_x with \tilde{B}_y , a discontinuity in this derivative is implied. This (relative) discontinuity is commonly defined as⁷

$$\Delta' := \left[\frac{\partial_x \tilde{B}_x}{\tilde{B}_x} \right]_{0^-}^{0^+} = \frac{\partial_x \tilde{B}_x}{\tilde{B}_x} \Big|_{x=0^+} - \frac{\partial_x \tilde{B}_x}{\tilde{B}_x} \Big|_{x=0^-}. \quad (2.36)$$

This quantity plays a central role and we will continue this section by finding solutions to the set of equations (2.25)-(2.27) and consecutively calculating Δ' .

⁶One can see this for e.g. constant current density where $I_z = j_z \Delta x \Delta y$. For the derived expression Δy cancels and the current flows only in the region Δx which was taken to be infinitesimal small.

⁷This can also be seen as the discontinuity in the logarithmic derivative: $\partial_x \ln(A) = \frac{1}{A} \partial_x A$.

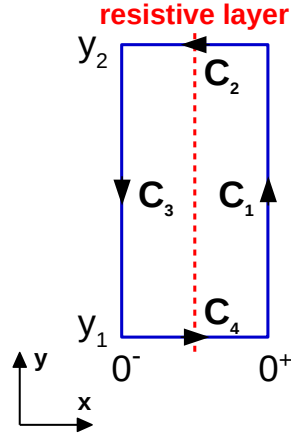


Figure 2.3. Contours in the xy -plane around the sheet-like layer.

2.1.4 Solutions in the Outer Region

As has been indicated before, the only difficulty lies in solving the equation for the x -component of the perturbed field. Once this has been done, all other quantities can be calculated. We start with \tilde{B}_x by rewriting (2.25) into a slightly different form:

$$\partial_x^2 \tilde{B}_x - k^2 \tilde{B}_x = q, \quad (2.37)$$

$$q := \tilde{B}_x \frac{\partial_x^2 F}{F}. \quad (2.38)$$

Eq. (2.37) now has the form of a simple ODE with some perturbative term q (that is dependent on the solution itself).

Short wavelength limit: First we want to consider the limit $k \gg 1$ in which case we can neglect the contribution by q . Then we have a simple ODE with solutions

$$\tilde{B}_x = C e^{-k|x|}, \quad (2.39)$$

where C is a constant and the absolute value in the exponent results from the fact that we already applied boundary conditions on both sides of the sheet-like layer: $\tilde{B}_x(x \rightarrow \pm\infty) = 0$. By the reason of symmetry we implied the assumption that $\tilde{B}_x(-x) = \tilde{B}_x(x)$. Using this solution in (2.36) we get the discontinuity as

$$\Delta' = -2k. \quad (2.40)$$

This is due to the inner derivative of the absolute value of x giving an extra $\text{sign}(x)$, making this quantity non-zero.

Long wavelength limit: In this case we have $k \ll 1$ and one can expand the solution for \tilde{B}_x in terms of (2.39). This has been done by FKR [23] in their treatment of the outer region. We are only interested in the k -dependence of the asymptotic solution for the discontinuity that is given by

$$\Delta' \sim \frac{1}{k}. \quad (2.41)$$

One can see that for small k values we get positive Δ' and for large k values negative Δ' . In a realistic configuration only certain values of k are allowed as it will be linked to integer mode numbers, thus some modes will have positive Δ' and others will have negative Δ' . The implication of this fact will become clear when advancing to the end of this section.

Full solution: We now treat the full ODE for the x -component of the perturbation given in (2.37). We can consider the short wavelength solution (2.39) as the homogenous solution of the ODE leaving us with the task to find a particular solution. We can apply the method called *Variation of Constants*⁸ (on the solution without applied boundary conditions) using the ansatz

$$\tilde{B}_x = C_+(x) e^{kx} + C_-(x) e^{-kx}. \quad (2.42)$$

The procedure is now to compute the first derivative, insert it into the ODE (2.37), obtain an expression for $\partial_x C_{\pm}(x)$ and integrate this to get $C_{\pm}(x)$ itself. Then, a particular solution has been found and we get the general solution by adding this to the homogenous one. This general solution is

$$\tilde{B}_x = \begin{cases} \frac{e^{kx}}{2k} \int_{-\infty}^x dx' q(x') e^{-kx'} + e^{-kx} \left(C_- - \frac{1}{2k} \int_{-\infty}^x dx' q(x') e^{kx'} \right), & x > 0^+, \\ e^{kx} \left(C_+ + \frac{1}{2k} \int_{-\infty}^x dx' q(x') e^{-kx'} \right) - \frac{e^{-kx}}{2k} \int_{-\infty}^x dx' q(x') e^{kx'}, & x < 0^-. \end{cases} \quad (2.43)$$

Since the quantity q is dependent on \tilde{B}_x itself this is an implicate solution for \tilde{B}_x and must be solved numerically in an iterative way. The same symmetry reasons that have been used for the homogenous equation $\tilde{B}_x(-x) = \tilde{B}_x(x)$, lead to the result that both constants are the same, i.e. $C_+ = C_- \equiv C$.

We can use this formal solution in (2.36) to get an analytical expression for the discontinuity,

$$\Delta' = -2k - \frac{1}{B_1} \int_{-\infty}^{\infty} \tilde{B}_x \frac{F''}{F} e^{-kx'} d'x', \quad (2.44)$$

where $B_1 = \tilde{B}_x \Big|_{x=0^{\pm}}$ and d' denotes that the integral has to be taken *non-continuously* over $x' = 0$. This is the main result of FKR [23] in the outer region. Before giving an example calculation in the next section, one can write the general solution given in (2.43) in a different way:

$$\tilde{B}_x = \begin{cases} \frac{e^{kx}}{2k} \int_{-\infty}^x dx' q(x') e^{-kx'} + e^{-kx} \left(B_1 + \frac{1}{2k} \int_0^{\infty} dx' q(x') e^{-kx'} - \frac{1}{2k} \int_0^x dx' q(x') e^{kx'} \right), & x > 0^+, \\ e^{kx} \left(B_1 + \frac{1}{2k} \int_0^{\infty} dx' q(x') e^{-kx'} + \frac{1}{2k} \int_0^x dx' q(x') e^{-kx'} \right) - \frac{e^{-kx}}{2k} \int_{-\infty}^x dx' q(x') e^{kx'}, & x < 0^-. \end{cases} \quad (2.45)$$

This may look more complicated but it turned out that it is numerically more stable to solve this iterative equation than (2.43). It also has the advantage to contain the perturbed field at the boundary B_1 instead of the constant C . This can be set to a typical perturbation strength which must be specified anyway.

⁸Often also called *Variation of Parameters*.

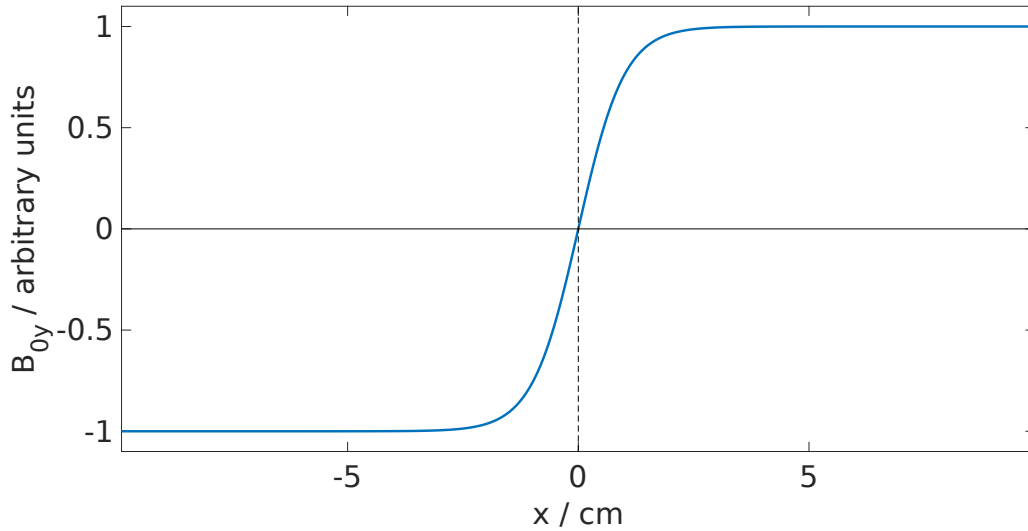


Figure 2.4. Chosen toy model for the equilibrium field configuration.

2.1.5 Application of a Toy Equilibrium

Solving the central iMHD equations we arrived at a solution that looks not so friendly but should behave quite stable when implemented numerically. We will start exploiting this by choosing a “toy” equilibrium and solve these equations. An analytically nice model to study is a hyperbolic tangent one (figure 2.4)⁹,

$$B_{0y} \equiv \tanh(x). \quad (2.46)$$

Even at $x = 0$ there is an existing value for $q \sim F''/F$. Parameters left to specify are the perturbation strength and the wavevector respectively. The first one can be set by the following thought: by the given form of (2.46) we have limiting amplitudes of ± 1 for the equilibrium field. Because the perturbation we apply must be small by assumption, a typical value that can be chosen is

$$B_1 \equiv 10^{-4}. \quad (2.47)$$

For the latter quantity a pseudo-realistic approach is used. Despite the fact that we do not have a real configuration, we use integer mode numbers and typical lengths. We associate the y -direction to be poloidal and the z -direction to be toroidal,

$$k_y = \frac{m}{L_y}, \quad L_y \equiv 10 \text{ cm}, \quad (2.48)$$

$$k_z = \frac{n}{L_z}, \quad L_z \equiv 170 \text{ cm}. \quad (2.49)$$

The integers m and n are then the poloidal and toroidal mode numbers, respectively. Further, we restrict the toroidal mode number to the single value

$$n \equiv 2, \quad (2.50)$$

⁹This form implies the use of normalized units for the magnetic field strength.

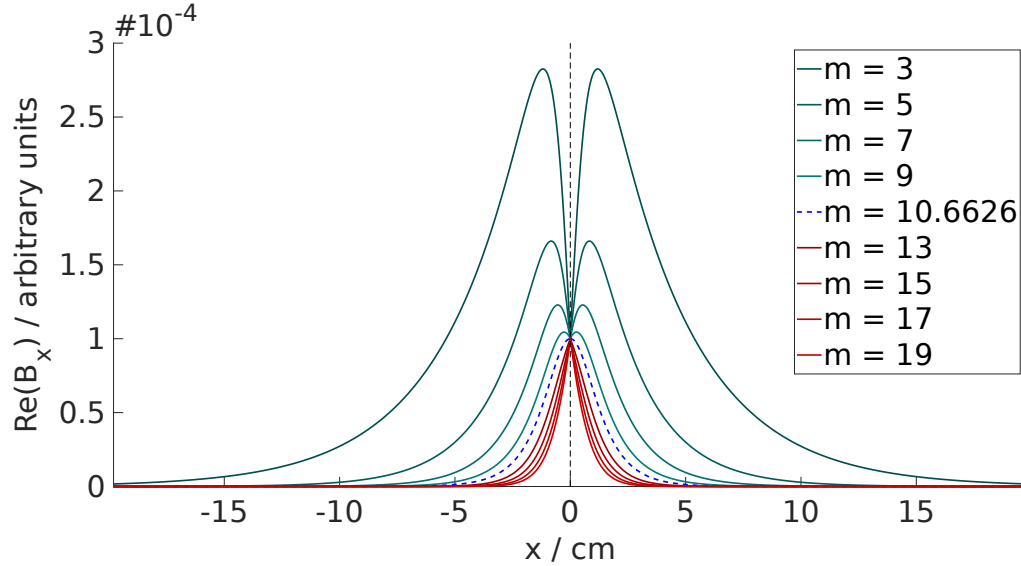


Figure 2.5. Solutions for the x -component of the perturbed magnetic field for different poloidal mode numbers (real part).

and only vary the poloidal mode number m instead.

The field components are then calculated first, by using our general solution for \tilde{B}_x (2.45) and second, by afterwards applying (2.26) and the divergence-freeness (2.27). The solutions for different mode numbers can be seen in figure 2.5, 2.6 and 2.7 respectively.

As has been discussed before, \tilde{B}_x is purely real and \tilde{B}_y and \tilde{B}_z are purely imaginary¹⁰. The second observation is the continuity of \tilde{B}_x and the discontinuity of its derivative (kink of \tilde{B}_x), together with \tilde{B}_y and \tilde{B}_z (jump). It is nice to see the previous considerations match with the numerical results. The third thing to discuss is the color-coding of the different considered mode numbers. This has been done by calculating the discontinuity Δ' using either (2.36) or (2.44) and checking its sign afterwards. “Green-ish” corresponds to $\Delta' > 0$ and “red-ish” to $\Delta' < 0$. There is a slight color-gradient indicating the magnitude of Δ' , but generally we are interested in its behaviour. The blue curve is a limiting case, where beforehand the analytical model was solved for k with $\Delta' = 0$. It would not occur for our choice of scale lengths because mode number m is not an integer for this curve.

The values for Δ' for the different mode numbers can be seen in figure 2.8. Additionally to the calculated values of Δ' a solid red curve is shown which is the exact analytical solution for this model that has been calculated by FKR [23]¹¹.

The last thing to discuss is the functional form of the discontinuity Δ' . One can clearly see that for large k it starts to be linearly decreasing, with an approximate slope of 2 which fits perfectly to our limiting calculation (2.40) (it can be seen even better when advancing to higher mode numbers). For small k it is harder to see, but there is a trend towards a singular behaviour at $k = 0$. This point can clearly not be reached since our mode numbers are limited by the smallest positive integer which is 1. The plot even starts at a k value that corresponds to $m = 3$ which was chosen to be the smallest mode considered, because of deeper reasons in real configurations¹².

¹⁰This is the reason one only sees the corresponding non-vanishing components in the plots.

¹¹The thin black line is called “stability criterion” which will be apparent when advancing to the end of this section (section 2.2).

¹²In cylindrical or toroidal geometry it turns out that positions where such sheet currents arise are located where

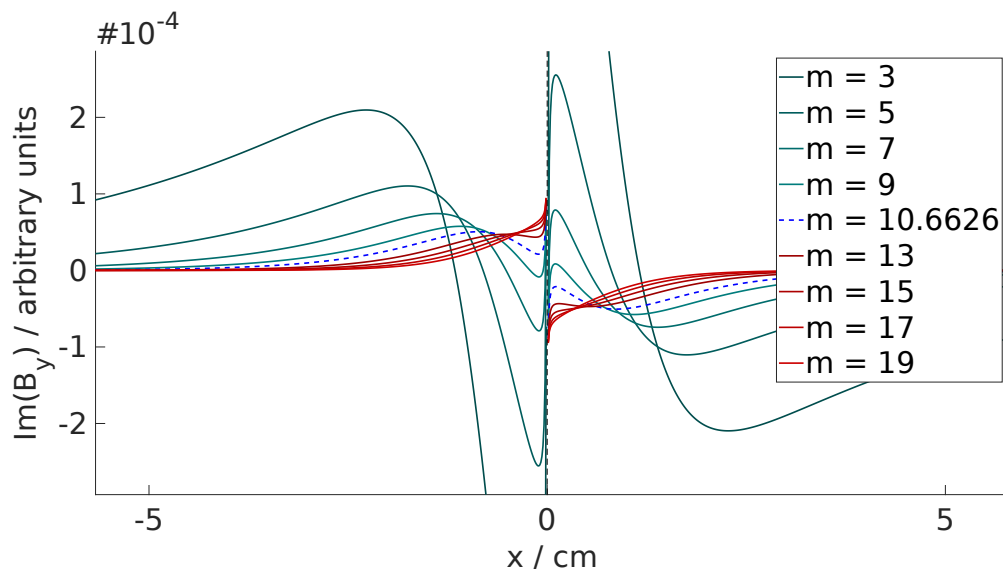


Figure 2.6. Solutions for the y -component of the perturbed magnetic field for different poloidal mode numbers (imaginary part).

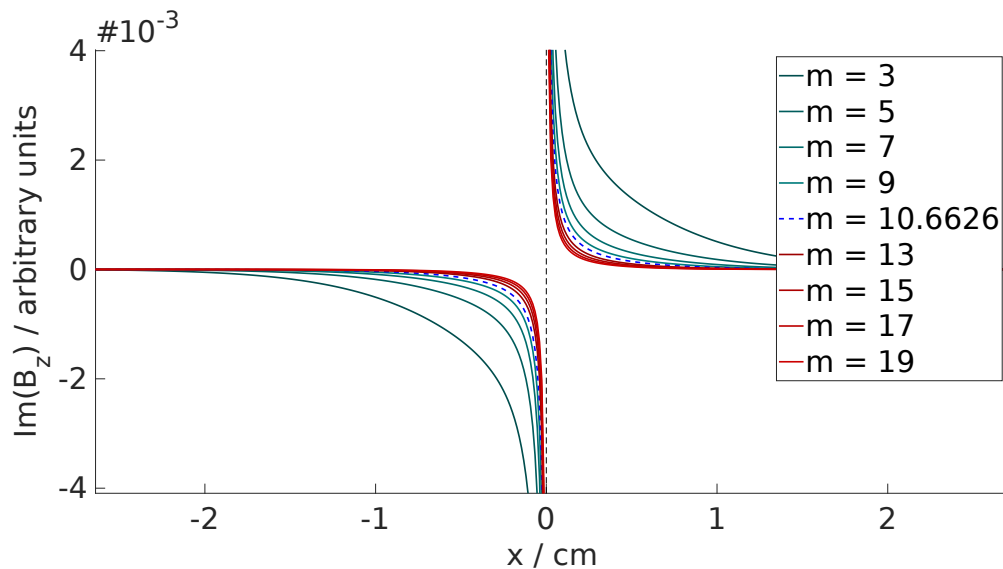


Figure 2.7. Solutions for the z -component of the perturbed magnetic field for different poloidal mode numbers (imaginary part).

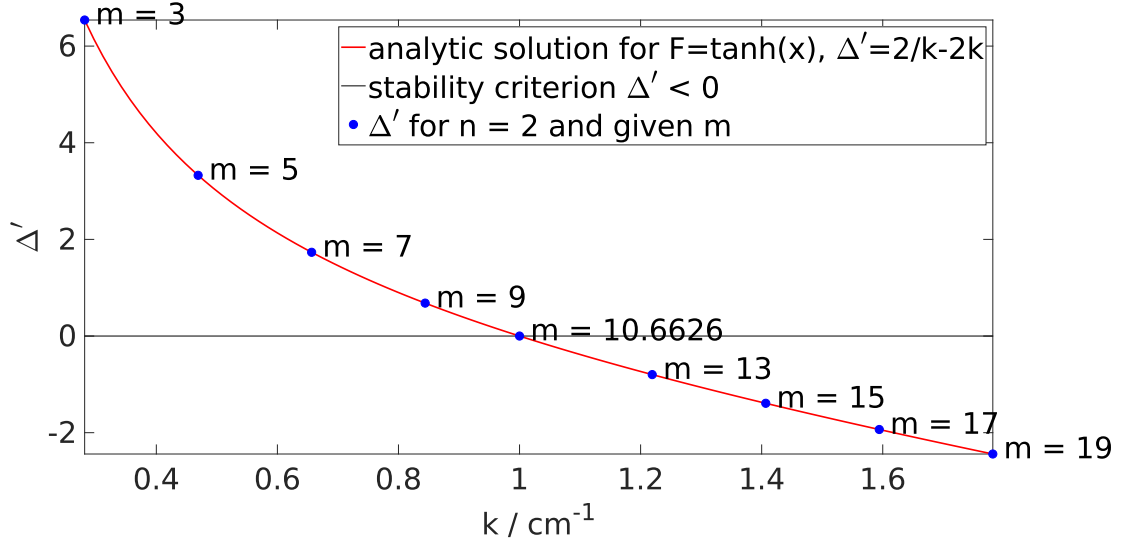


Figure 2.8. Calculated Δ' corresponding to the solutions given in figure 2.5 together with the corresponding analytical solution and the “stability criterion” described in the main text.

2.1.6 Magnetic Islands

With the solution given in (2.45), we can consider the problem in the outer region to be solved. Nevertheless, there is still one thing remaining as we can look at the form of the magnetic field lines. Since the perturbation is small we expect something similar to our equilibrium field shown in figure 2.1.

The following considerations can be found partially in the book of GR [20]. To look at lines of constant magnetic field strength, one has to solve the field line equation (see e.g. the book of D’HAESELEER [26]). In the xy -plane this reads as

$$\frac{dx}{B_x} = \frac{dy}{B_y}. \quad (2.51)$$

This can be rewritten and integrated giving

$$\int B_y dx - \int B_x dy = \text{const.} \quad (2.52)$$

We want to consider the effect of a general perturbation to the equilibrium that still corresponds to our given geometry (γ represents a potential growth rate),

$$\delta B_\alpha = \tilde{B}_\alpha e^{ik_y y + \gamma t}. \quad (2.53)$$

Since the x -component consists only of the perturbation, the second integral (2.52) can be evaluated immediately, yielding

$$\int \delta B_x dy = -i \frac{\delta B_x}{k_y}. \quad (2.54)$$

the safety factor q reaches rational numbers which are given by the fraction m/n . Because of basic iMHD stability considerations we need $q > 1$ everywhere to avoid crucial instabilities. This means that $m > n$ and i.e. for integers $m > 1$.

The *phase* of the solution can be chosen arbitrarily,

$$\text{Im} \left(\int B_{0y} dx + \int \tilde{B}_y dx e^{ik_y y + \gamma t} + i \frac{\tilde{B}_x}{k_y} e^{ik_y y + \gamma t} \right) = \text{const.} \quad (2.55)$$

In this section we have already shown that \tilde{B}_y is purely imaginary, i.e. $\tilde{B}_y = i \text{Im}(\tilde{B}_y)$ which can be used to give the general equation for this configuration¹³:

$$B_E + \cos(k_y y) e^{\gamma t} B_P = \text{const.}, \quad (2.56)$$

$$B_E = \int B_{0y} dx, \quad (2.57)$$

$$B_P = \int \text{Im}(\tilde{B}_y) dx + \frac{\tilde{B}_x}{k_y}. \quad (2.58)$$

This form has split the field line equation into an equilibrium part and a modification due to the perturbation.

Ref. [20] treats the problem only in a narrow region around $x = 0$. This means one can approximate the equilibrium field by its derivative and the perturbed field as constant,

$$B_y \approx [\partial_x B_{0y}]_{x=0} x, \quad (2.59)$$

$$\tilde{B}_x \approx B_1. \quad (2.60)$$

Eq. (2.56) can then be solved explicitly to give

$$\frac{1}{2} [\partial_x B_{0y}]_{x=0} x^2 + \frac{B_1}{k_y} \cos(k_y y) e^{\gamma t} = \text{const.} \quad (2.61)$$

As long as the region that is affected by the perturbation is small, it does not matter whether we use (2.56) or (2.61). For example, we can plug in our previous numerical solutions for the perturbed magnetic field into one of the field line equations and look at the resulting contour lines (figure 2.9). As one can see immediately, the shape of our initial current sheet equilibrium has changed dramatically. Near the sheet-like layer the topology of straight field lines¹⁴ has broken up and instead *magnetic islands* have formed. The current sheet has split up into current filaments. Outside the *separatrix* (last closed flux surface of the island) the field line topology has not changed, instead there are only small perturbations to the “straightness” of the lines.

The main question that arises is related to the size of these magnetic islands. Do they become macroscopically large, affecting the equilibrium and stability of our whole configuration or do they stay small, maybe even infinitesimal?

¹³With $i = e^{i\frac{\pi}{2}}$ the term containing \tilde{B}_x could be simplified by

$$\text{Im} \left(i e^{ik_y y} \right) = \text{Im} \left(e^{i(k_y y + \frac{\pi}{2})} \right) = \sin \left(k_y y + \frac{\pi}{2} \right) = \cos(k_y y).$$

¹⁴Which are nested flux surfaces in real configurations.

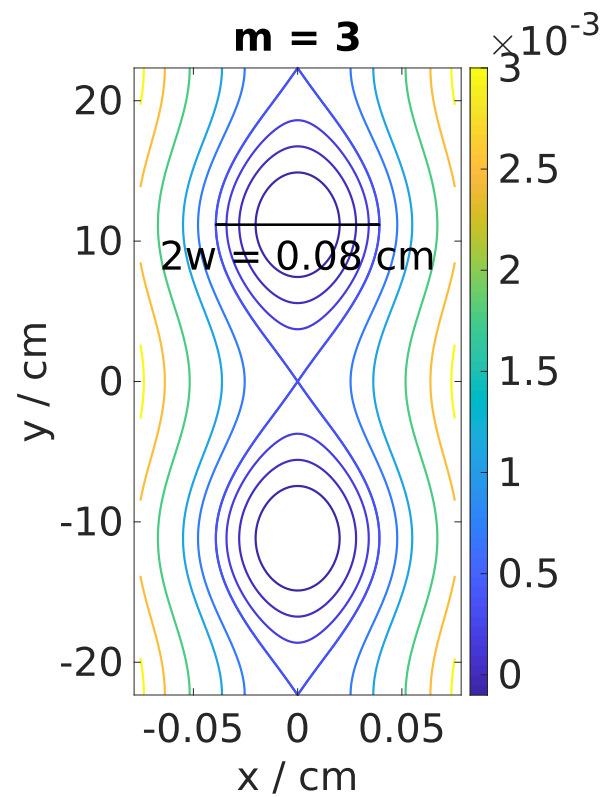


Figure 2.9. Magnetic islands resulting for the given equilibrium field and the applied perturbation for mode $m = 3$. The width of the island has been numerically calculated and included in the plot.

Properties of magnetic islands: Either (2.56) or (2.61) indicate a periodic structure in y -direction that leads consequently to a repetition of magnetic islands with period

$$h = \frac{2\pi}{k_y}, \quad (2.62)$$

which is referred as the *height* of the island. At the maximum of the cosine function ($y = \pi/k_y$), the island will have its largest extent in x -direction which is the *island width* w . To get this value one can trace the corresponding field line (*separatrix*) back to $y = 0$ where $x = 0$. At this point the cosine is 1 and the equation reads

$$\frac{B_1}{k_y} e^{\gamma t} = \text{const.} \quad (2.63)$$

It must hold for the same field line everywhere so back at the point $y = \pi/k_y$ and $x = w$ we have

$$\frac{1}{2} [\partial_x B_{0y}]_{x=0} w^2 - \frac{B_1}{k_y} e^{\gamma t} = \frac{B_1}{k_y} e^{\gamma t}. \quad (2.64)$$

Solving for the width yields

$$w = 2e^{\gamma t/2} \sqrt{\frac{B_1}{k_y [\partial_x B_{0y}]_{x=0}}}. \quad (2.65)$$

This has been done using the analytically simpler form (2.61) instead of the general one (2.56)¹⁵.

These are basically all relevant properties of magnetic islands¹⁶. One can see that the island width (which is basically the only relevant parameter) grows exponentially in time, given a positive real growth rate.

2.1.7 Ideal Stability

Throughout most of this section we assumed static equations. However, discussing magnetic islands we suddenly introduced a growth rate in our assumed form of the perturbation and discovered the islands to possibly grow in time. For determining this growth rate we have to go back to the beginning and change our initial equations to include dynamic effects.

Using dynamic equations will force us to use introduce the flow velocity in our equations. We will assume zero flow in equilibrium:

$$\mathbf{v}_0 = 0, \quad (2.66)$$

$$\mathbf{v} = \delta \mathbf{v}. \quad (2.67)$$

¹⁵For the general case of (2.56), at $x = 0$ and $y = 0$ one has $B_E = 0$ and $\cos(k_y y) = 1$:

$$e^{\gamma t} B_P|_{x=0} = \text{const.}$$

This results in an equation for w :

$$e^{-\gamma t} B_E(w) - B_P(w) - B_P|_{x=0} = 0.$$

This is similar to the special case (2.65), but instead with a slightly distorted parabola.

¹⁶For the sake of completeness: the choice of phase will only affect the \pm shift in y -direction.

Part of the dynamics will still be neglected, i.e. convective effects in the inertial terms of the pressure balance. This means we replace the total by the partial time derivative of the velocity,

$$\nabla p = \frac{1}{4\pi} \left[(\mathbf{B} \cdot \nabla) \mathbf{B} - \frac{1}{2} \nabla B^2 \right] - \rho \partial_t \mathbf{v}. \quad (2.68)$$

The temporal change of the magnetic field is then given by FARADAY'S law (2.4) and is linked to the velocity by ideal OHM'S law (2.7),

$$\partial_t \mathbf{B} = -\nabla \times \mathbf{E} = \nabla \times (\mathbf{v} \times \mathbf{B}) = (\mathbf{B} \cdot \nabla) \mathbf{v} - (\mathbf{v} \cdot \nabla) \mathbf{B}. \quad (2.69)$$

The last equality used some vector calculus, the divergence-freeness of the magnetic field (2.6) and additionally

$$\nabla \cdot \mathbf{v} = 0. \quad (2.70)$$

This equation describes what we know as *incompressible flow*, which is maybe not strictly true but in good approximation useable. In our normal mode analysis we then use time dependent perturbations,

$$\delta f = \tilde{f}(x) e^{i\mathbf{k} \cdot \mathbf{r} - i\omega t}, \quad (2.71)$$

where f is a scalar or vector quantity and ω is generally a complex number. For purely imaginary ω we have exponential growth with growth rate

$$\gamma = \text{Im}(\omega), \quad (2.72)$$

with $\gamma > 0$ meaning growth and $\gamma < 0$ decrease. For purely real omega these perturbations describe *waves*. The goal of *stability analysis* is to identify the exact value of ω .

The application of linear perturbations to (2.69), keeping only linear terms results in the following expression,

$$\partial_t \delta \mathbf{B} = (\mathbf{B}_0 \cdot \nabla) \delta \mathbf{v} - (\delta \mathbf{v} \cdot \nabla) \mathbf{B}_0, \quad (2.73)$$

or using normal modes

$$-\omega \tilde{\mathbf{B}} = F \tilde{\mathbf{v}} + i \tilde{v}_x \partial_x \mathbf{B}_0. \quad (2.74)$$

The last equation connects the magnetic field with the flow velocity and can be viewed as a the *frozen flux condition* of ALFVÉN in some sense. Later we will need the x -component of this equation:

$$-\omega \tilde{B}_x = F \tilde{v}_x. \quad (2.75)$$

Dynamic modifications: In the pressure balance (2.18) we have to add one term,

$$4\pi (\partial_x \tilde{p} \mathbf{e}_x + i\mathbf{k}\tilde{p}) = iF\tilde{\mathbf{B}} + \tilde{B}_x \partial_x \mathbf{B}_0 - \partial_x (\mathbf{B}_0 \cdot \tilde{\mathbf{B}}) \mathbf{e}_x - i\mathbf{k} (\mathbf{B}_0 \cdot \tilde{\mathbf{B}}) + 4\pi i \omega \rho_0 \tilde{\mathbf{v}}. \quad (2.76)$$

The new set of central equations will then look like:

$$\partial_x (4\pi \tilde{p} + \mathbf{B}_0 \cdot \tilde{\mathbf{B}}) = iF\tilde{B}_x + 4\pi i \omega \rho_0 \tilde{v}_x, \quad (2.77)$$

$$k^2 (4\pi \tilde{p} + \mathbf{B}_0 \cdot \tilde{\mathbf{B}}) = F (\mathbf{k} \cdot \tilde{\mathbf{B}}) - i\tilde{B}_x \partial_x F + 4\pi \omega \rho_0 (\mathbf{k} \cdot \tilde{\mathbf{v}}), \quad (2.78)$$

$$\partial_x \tilde{B}_x + i\mathbf{k} \cdot \tilde{\mathbf{B}} = 0, \quad (2.79)$$

$$\partial_x \tilde{v}_x + i\mathbf{k} \cdot \tilde{\mathbf{v}} = 0. \quad (2.80)$$

The last equation is simply the incompressibility of the perturbed flow velocity which is formally the same as the divergence-freeness of the perturbed magnetic field. Our “simple” ODE for \tilde{B}_x (left hand side) is then modified by inertial terms introduced by the velocity perturbation (right hand side),

$$\partial_x^2 \tilde{B}_x - \tilde{B}_x \left(k^2 + \frac{\partial_x^2 F}{F} \right) = -\frac{4\pi \omega}{F} (\partial_x (\rho_0 \partial_x \tilde{v}_x) - k^2 \rho_0 \tilde{v}_x). \quad (2.81)$$

This equation can be combined with the previously derived connection of \tilde{B}_x and \tilde{v}_x (2.75), to give either an equation only for \tilde{B}_x or \tilde{v}_x . We will choose the latter one as it turned out to be much simpler than the other one. Namely

$$\partial_x ([F^2 - 4\pi \omega^2 \rho_0] \partial_x \tilde{v}_x) - k^2 [F^2 - 4\pi \omega^2 \rho_0] \tilde{v}_x = 0. \quad (2.82)$$

A slightly different form of this equation can also be found in the book of GR [20].

Stability analysis: We do not want to solve (2.82), instead we multiply it by the complex conjugate of the velocity \tilde{v}_x^* and integrate it over the whole domain $-\infty < x < \infty$ ¹⁷. We can apply partial integration since the perturbed flow velocity must vanish at the boundaries $\tilde{v}_x(x \rightarrow \pm\infty) = 0$, to get

$$\int_{-\infty}^{+\infty} dx (F^2 - 4\pi \omega^2 \rho_0) (|\partial_x \tilde{v}_x|^2 + k^2 |\tilde{v}_x|^2) = 0. \quad (2.83)$$

This equation is essential in our stability analysis. It gives a general condition for ω^2 :

$$\omega^2 = \frac{F^2}{4\pi \rho_0} \stackrel{(2.19)}{=} \frac{B_0^2}{4\pi \rho_0} k_{\parallel}^2 = v_A^2 k_{\parallel}^2. \quad (2.84)$$

Because the right side is purely positive, we can immediately see that ω must be purely real. This means that we have oscillatory modes or *waves* (shear ALFVÉN waves) and our equilibrium configuration is stable. Furthermore, this means that there are no macroscopic magnetic islands produced by the current sheet in this particular iMHD treatment.

¹⁷Of course we must exclude the narrow region around the sheet-like layer.

2.2 Resistive MHD Treatment

It was already mentioned several times that the initial iMHD equations are not valid throughout the whole domain of the current sheet. In the inner region we need to use different, non-singular equations to investigate the stability of the current sheet. This could be any model that describes the plasma more or less accurately, e.g. kinetic theory or *resistive Magnetohydrodynamics*. As has been stated in the beginning, the latter one was used by FKR [23]. This section will connect their work to the previous analysis (section 2.1) and will discuss some of the main results.

2.2.1 Resistive Modifications

We will use the same assumptions and the same configuration as in the section before. The main difference lies in OHM's law which introduces a *resistivity* or equivalently inverse conductivity $\eta = \sigma^{-1}$ in the equations:

$$\mathbf{E} + \mathbf{v} \times \mathbf{B} = \eta \mathbf{J}. \quad (2.85)$$

This can now be applied to the remaining rMHD equations that coincide to the iMHD ones. The procedure is exactly the same as in section 2.1.7. Resistive OHM's law (2.85) will link the magnetic field perturbation with the velocity, but in a different way as the frozen flux condition has done,

$$-i\omega \tilde{B}_x = iF\tilde{v}_x + \frac{\eta_0}{4\pi} \left(\partial_x^2 \tilde{B}_x - k^2 \tilde{B}_x \right). \quad (2.86)$$

Slightly rewritten and put together with the perturbed momentum equation we arrive at the central set of equations:

$$\partial_x^2 \tilde{B}_x - k^2 \tilde{B}_x = -\frac{4\pi i}{\eta_0} \left(\omega \tilde{B}_x + F\tilde{v}_x \right), \quad (2.87)$$

$$\partial_x^2 \tilde{B}_x - \tilde{B}_x \left(k^2 + \frac{\partial_x^2 F}{F} \right) = -\frac{4\pi\omega}{F} \left(\partial_x (\rho_0 \partial_x \tilde{v}_x) - k^2 \rho_0 \tilde{v}_x \right). \quad (2.88)$$

These two equations correspond to the dimensionless equations (13, 14) derived by FKR¹⁸. At this point we will end this resistive MHD treatment, because the complexity of the problem rises beyond the expected reward of fully solving it. This is due to the fact that our interest will be more in the difference of inner and outer region which has been already discussed and not in the growth rates and resistive stability itself. For the sake of completeness a short summary of some of the main results of the work of FKR is given in the next section.

¹⁸They included additionally x -dependent resistivity and gravitational effects and have the x and y axis switched. Additionally their frequency ω corresponds to a growth rate γ in this notation.

2.2.2 Discussion on the FKR Treatment

Solving the rMHD equations in the inner region of the current sheet is a tedious work. FKR assumed many quantities almost constant in the narrow region except \tilde{B}_x and \tilde{v}_x . A solution for the latter one could be found in terms of normalized HERMITE functions, leaving only the first one to be identified. In the end the “*constant- ψ approximation*”¹⁹ was used which means that \tilde{B}_x is approximately constant in the inner region. This can be taken to be valid for almost all k , except for those which correspond to wavelengths smaller than the size of the inner region²⁰.

Given all these approximations FKR managed to find an analytical expression for the growth rate (2.71), (2.72)²¹:

$$\gamma = 4\Omega^{4/5} \left(\frac{\eta_0^3 |\partial_x F|_{x=0}^2}{(4\pi)^4 \rho_0} \right)^{1/5}. \quad (2.89)$$

They used the abbreviation Ω for a quantity that can be connected to the discontinuity Δ' we encountered in (2.36),

$$\Omega \approx \frac{1}{12} \Delta' + \mathcal{O}(\eta'). \quad (2.90)$$

The second term can be neglected because it only exists for non-constant resistivity which we do not assume here²². Using this in the above expression for the growth rate (2.89) we find

$$\gamma \approx 0.55 \left(\frac{\Delta'^4 \eta_0^3 |\partial_x F|_{x=0}^2}{(4\pi)^4 \rho_0} \right)^{1/5}. \quad (2.91)$$

This is a remarkable result²³ as all quantities on the right side are known and the growth rate is now fully determined. One may legitimately ask where to get Δ' from, but we already found it as a solution in the treatment of the outer region. As this quantity was defined at the boundary of both regions it must be the same in the whole domain, thus we can calculate it with (2.44).

The second thing which can be immediately seen, is the fact that all quantities on the right side are defined as *positive* except Δ' which can be either positive or negative. For exponential growth we need $\gamma > 0$ which leads us to the condition for the tearing instability to occur:

$$\Delta' > 0. \quad (2.92)$$

Last thing to mention is the resistivity dependency of the growth rate. As γ is proportional to some power of η , the growth rate gets smaller the smaller the resistivity gets. At $\eta \rightarrow 0$ we have $\gamma \rightarrow 0$ and we get stability back²⁴.

Finally we can also state an expression for the sheet-like layer thickness which is analytically linked to the growth rate and thus given by

¹⁹The name comes from the fact that in their notation $\psi \equiv \tilde{B}_x$.

²⁰This will hold for $m = 1$ modes in cylindrical and toroidal configurations.

²¹Equations were taken from the work of FKR and translated into the notation used here.

²²Inclusion of this term leads to a quadratic equation in Ω which still can be solved and inserted in (2.89).

²³Exactly the same result can be found in the book of GR [20] who did the treatment of the inner region in a different (and simplified) way compared to FKR.

²⁴This is somehow evident as $\eta \rightarrow 0$ corresponds to the iMHD limit and thus to stability as has been shown in section 2.1.7. Of course we have to again exclude the inner region in that case.

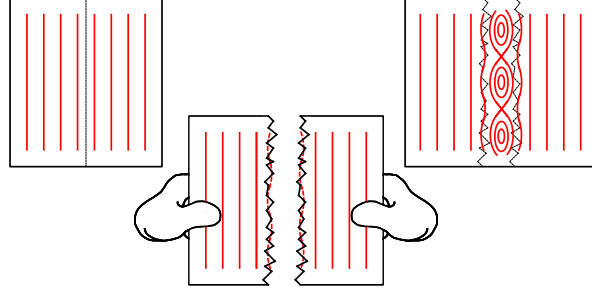


Figure 2.10. Cartoon to show the origin of the name *tearing* instability. One can think of the instability tearing the original straight field line equilibrium apart, leaving room for magnetic islands to form.

$$d = \left(\frac{\gamma \eta_0 \rho_0}{4 |\partial_x F|_{x=0}^2} \right)^{1/4} \stackrel{(2.91)}{\approx} 0.61 \left(\frac{\eta_0^2 \rho_0 \Delta'}{4\pi |\partial_x F|_{x=0}^2} \right)^{1/5}. \quad (2.93)$$

This quantity only makes sense for the case of (2.92) to be true. Same as for γ , the thickness of the sheet-like layer gets smaller for smaller resistivity, arriving at a single sheet for $\eta_0 \rightarrow 0$.

2.3 Summary on Tearing Mode Theory

In the previous sections we did a quite detailed iMHD treatment of the current sheet equilibrium. From the basic equations we applied linear perturbations and did a normal mode analysis to find a singular behaviour of the equations defining the perturbed magnetic field \tilde{B}_x . We resolved this by splitting the domain into inner and outer region. At the boundary a short analysis has shown that the \tilde{B}_y has a discontinuity and due to the divergence-freeness $\partial_x \tilde{B}_x$ which was linked to the relative discontinuity Δ' .

In the outer region we solved the equations to find all components of $\tilde{\mathbf{B}}$ and a value for Δ' . A numerical toy model was used to show all the features of the solution. Dependent on the wavevector (or mode number) we got positive or negative values for Δ' . The first for small k and the latter for large ones. An investigation of the magnetic field line structure has shown a potential development of magnetic islands that would grow in time given a positive growth rate which was, however, not defined to that point.

For this reason we did the whole analysis again for the dynamic case which gave us a slight modification of our defining equations for \tilde{B}_x , introducing the perturbed flow velocity component \tilde{v}_x . We have found an equation for the latter quantity that could be rewritten to show that the growth rate is in fact imaginary (i.e. a frequency) giving us waves and stability.

Still having in mind that we did not solve anything in the inner region at all, we turned to the original FKR treatment using rMHD to find a real growth rate that is linked to Δ' . For positive ones we have the tearing instability that is characterized by exponential growth.

Combining both treatments we can summarize that small perturbation mode numbers *may* lead to the equilibrium being tearing unstable, resulting in exponentially growing magnetic islands. At this point one can imagine the origin of the name *tearing instability*: it can be viewed as the mechanism that *tears* the equilibrium, i.e. the straight field line configuration apart, leaving room for magnetic islands to form (figure 2.10) which lower the overall magnetic energy of the configuration.

2.4 More on Tearing Modes and Magnetic Island Growth

This section shall provide a short overview of the basic works on tearing mode theory and furthermore on magnetic island growth. In no way this should be considered a full list of all relevant publications.

The basic work on tearing mode theory starts with the work of FKR [23] treating the current sheet configuration. An extension to cylindrical geometry and a more rigorous stability analysis for different current profiles can be found in the subsequent work of FURTH together with RUTHERFORD and SELBERG [27]. Application to toroidal systems was made by GLASSER, GREENE and JOHNSON [28, 29].

Non-linear theories: A new area on this topic was opened by the work of RUTHERFORD [30] who did a non-linear treatment of the problem and could show that the exponential growth of the tearing instability was replaced by algebraic (quadratic) growth of the perturbation as the size of the magnetic island approaches the thickness of the sheet-like layer. He could write an ODE (now often called RUTHERFORD equation):

$$\frac{\partial w}{\partial t} \propto \Delta' \eta. \quad (2.94)$$

for the time evolution of the island width that is linked to Δ' as the source of the tearing instability. The main cause of the weakened growth was found to be third-order non-linear forces that overcome inertia as the main opposing mechanism in island growth.

Based on this work, WHITE, et al. [31] could show in a quasi-linear analytical treatment that the island size may saturate for weakly unstable modes (Δ' positive but not large). Technically, the RUTHERFORD equation is then modified

$$\frac{\partial w}{\partial t} \propto [\Delta'(w) - \alpha w] \eta. \quad (2.95)$$

This means that the driving term Δ' is not constant for a given mode, but furthermore depends on the actual size of the island. The growth itself is also decreased by a restraining term. The square bracket may possess a zero for some width and therefore may saturate.

Magnetic Island Growth: The RUTHERFORD equation was then applied to magnetic islands in general without requiring them to be created by the tearing instability. For example, HAHM and KULSRUD [32] studied the effect of a boundary perturbation on magnetic islands and FITZPATRICK [33] the interaction with external structures in cylindrical geometry. Based on the first one, FITZPATRICK and HENDER [15] also considered the interaction of *Resonant Magnetic Perturbations* with the plasma, which links this topic to RMPs.

Neoclassical tearing modes: The work of CARRERA, et al. [34], has shown that a kinetic treatment of the island evolution can lead to different behaviour. Particularly the bootstrap current modifies the dynamics of tearing modes. Further it was found that radial diffusion, finite orbit width effects, electrostatic potentials, etc. do modify the evolution of islands as well. This has been summarized in the term “Neoclassical Tearing Modes”. A discussion with more references of the stated effects can be found in the overview paper by WILSON [35]. It is worth to note that all described effects do result in a modification of the RUTHERFORD equation discussed above.

Books on tearing modes: Often cited in this work is the book of GR [20] which treats the same configuration as FKR although a bit differently in a simplified version. The book of WHITE [36] discusses tearing modes in cylindrical geometry (or equivalently a large aspect ratio tokamak) and uses an approach with the helical flux instead of the perturbed field [27], simplifying equations a lot. The same holds for the standard book *tokamaks* by WESSON [6] which additionally puts the topic in a whole context of MHD instabilities.

Chapter 3

Linear Models in Cylindrical Approximation

This chapter is dedicated to introduce the cylindrical approximation where we treat the tokamak as a cylinder. After the initial considerations on geometry we will derive an equation similar to the “infinite conductivity equation” of FKR in section 2.1. This equation will hold for the outer regions of our boundary problem. For the inner region the *Kinetic Linear Cylindrical Approximation* is introduced. At the end of the section, an existing code will be used to analyze perturbations from the view of kinetics.

3.1 Large Aspect Ratio Limit / Cylindrical Tokamak

One of the most intuitive choices of a coordinate system to represent toroidal geometry are *quasi-toroidal coordinates*, defined by the transformation laws

$$\begin{aligned}x &= R \cos(\varphi), \\y &= R \sin(\varphi), \\z &= Z,\end{aligned}\quad \text{with} \quad \begin{aligned}R &= R_0 + r \cos(\theta), \\Z &= r \sin(\theta).\end{aligned}\quad (3.1)$$

The transformation is made via an intermediate cylindrical coordinate system (R, φ, Z) . The cylindrical R (large radius) and Z are represented by polar variables r, θ that have their origin on the major radius R_0 . Hence we get a system (r, θ, φ) which we call quasi-toroidal¹ (figure 3.1). The angles $\theta \in [0, 2\pi]$ and $\varphi \in [0, 2\pi]$ are called *poloidal* and *toroidal* respectively and $r \in [0, a]$ is the small radius (a is the minor radius). One can immediately see, that lines of constant r form nested tori, lines of constant θ form ribbons and lines of constant φ form circles (cross sections).

In a tokamak (generally also in a toroidal device) we can define the *aspect ratio* as the ratio between major and minor radius [24]:

$$A = \frac{R_0}{a}. \quad (3.2)$$

¹The word *quasi* is used to distinguish this system from the ordinary torus coordinates.

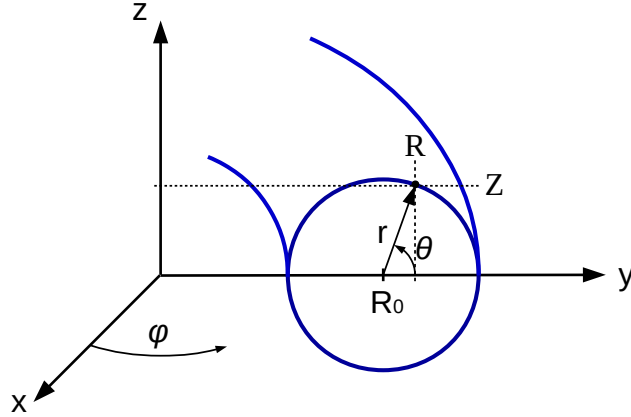


Figure 3.1. Sketch of quasi-toroidal coordinates. Blue represents the toroidal system.

For example spherical tokamaks have a very low aspect ratio ($A \rightarrow 1$) whereas conventional tokamaks have typically larger ones $A = 2 \sim 10$ [24]. The extreme case would be $A \rightarrow \infty$ which corresponds to a *cylinder* (figure 3.2). In this case, the cylinder height² z corresponds to the toroidal direction. The physical component of the toroidal magnetic field \hat{B}_φ can then be approximated by the z -component of a field in cylindrical geometry B_z ³.

Technically we can approximate a tokamak with major radius R_0 in *large aspect ratio limit* by a cylinder with $z \in [0, 2\pi R_0]$ that must be periodically continued infinitely in the toroidal direction. This is also known as the *Cylindrical Tokamak*.

The MHD equilibrium [24] of such a configuration will have nested flux surfaces in the form of concentric circles around the magnetic axis which is located at R_0 . The combination of toroidal and poloidal field will cause a winding of field lines around the cylinder which can be quantified by the rotational transform $\iota/2\pi$, or (more common for tokamaks) its inverse, the *safety factor* (see figure 3.3),

$$q = \frac{r B_z}{R B_\theta}. \quad (3.3)$$

This is a common definition as the ratio between toroidal ($= z$) and poloidal field. It is usually an approximation for the exact q , but in fact, it is exact for circular cross sections [26]. Whenever a field line closes upon itself after an integer amount of toroidal windings, one speaks of it being on a rational surface which is written as⁴

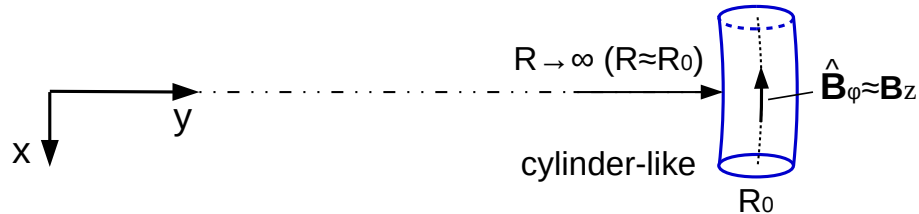


Figure 3.2. Sketch of large aspect ratio limit. Blue represents the toroidal system.

²The lower case letter z is chosen intentionally to not confuse it with Z from the cylinder system above.

³In the following, the hat on physical coordinates is omitted as long as no other coordinates are used (especially the covariant ones).

⁴Absolute value of q because the sign is a matter of convention.

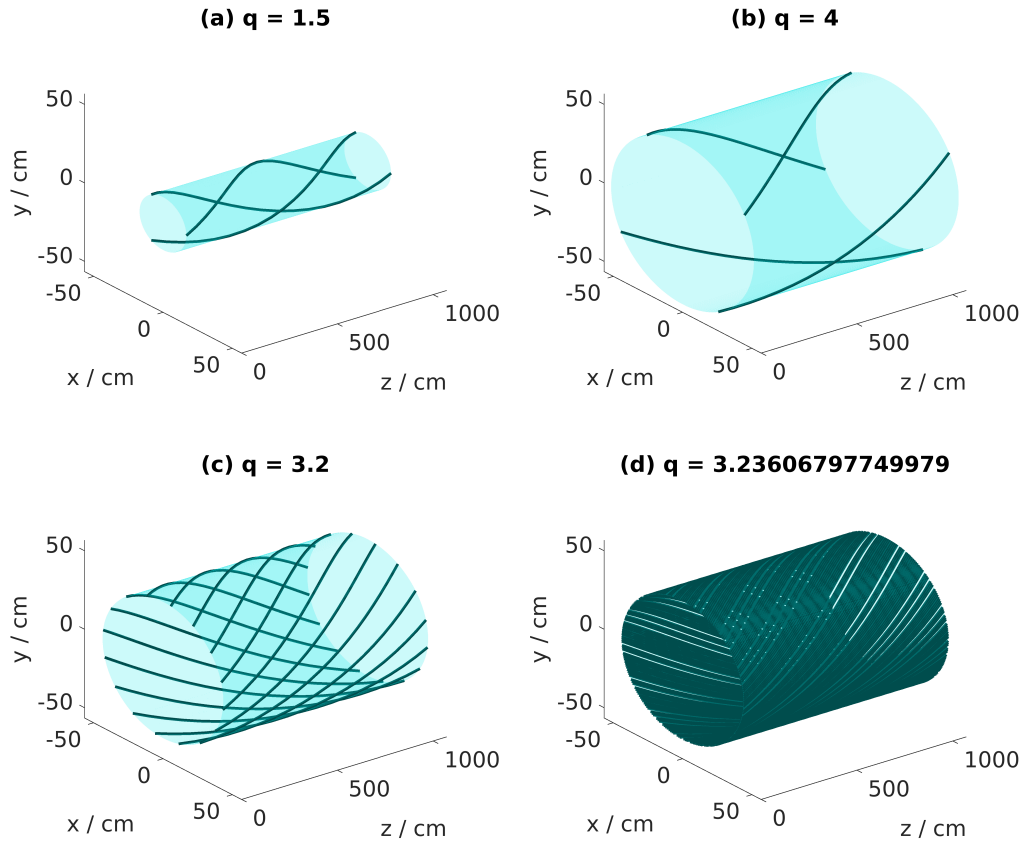


Figure 3.3. Magnetic field lines for different safety factors and 200 toroidal (z) turns. (a, b) show low rational field lines that close themselves after few toroidal transits. (c) shows a rather high rational field lines with 10 poloidal turns for 32 toroidal turns. (d) was taken twice the golden ratio ϕ (highly irrational) to represent the effect of irrational field lines. Although the absolute numerical value is not so different from the lower left figure, the irrational field line will map the whole cylinder surface whereas the other one will stay at a finite amount of lines.

$$|q| = q_r = \frac{m}{n}. \quad (3.4)$$

The safety factor on this flux surface is a rational number of two integer numbers m and n which characterize the amount of poloidal and toroidal windings done. For example $m = 5$ and $n = 3$ we have three poloidal turns done upon five toroidal turns until the field line closes.

This should complete all the essential geometric considerations and allow the analysis of the configuration in terms of iMHD in the next section.

3.2 Ideal MHD in the Cylindrical Tokamak

Based on the already established geometric considerations we will first look at the equilibrium and at the perturbation afterwards. In the end we will identify the locations of resonant regions, where we have to use the split up of outer and inner region from chapter 2.

3.2.1 Cylindrical Equilibrium

The symmetry of the cylinder gives us no other choice as to consider the following general form for the equilibrium magnetic field:

$$\mathbf{B}_0 = B_{0\theta}(r) \mathbf{e}_\theta + B_{0z}(r) \mathbf{e}_z. \quad (3.5)$$

The divergence-freeness follows naturally and the current can be computed using AMPÈRES law⁵,

$$4\pi \mathbf{J}_0 = (-\partial_r B_{0z}) \mathbf{e}_\theta + \left(\frac{1}{r} \partial_r [r B_{0\theta}] \right) \mathbf{e}_z. \quad (3.6)$$

The static pressure balance gives us the pressure gradient:

$$4\pi \nabla p_0 = - \left(B_{0z} \partial_r B_{0z} + B_{0\theta} \frac{1}{r} \partial_r [r B_{0\theta}] \right) \mathbf{e}_r. \quad (3.7)$$

We can see, that the magnetic field which has only poloidal and toroidal components gives rise to only poloidal and toroidal currents. The pressure gradient points radially outwards and is perpendicular to both current and magnetic field. The pressure decreases with radially increasing magnetic fields and vice versa. Constant pressure surfaces, as well as the magnetic field and the current lie on the circular cross sectioned flux surfaces (figure 3.4).

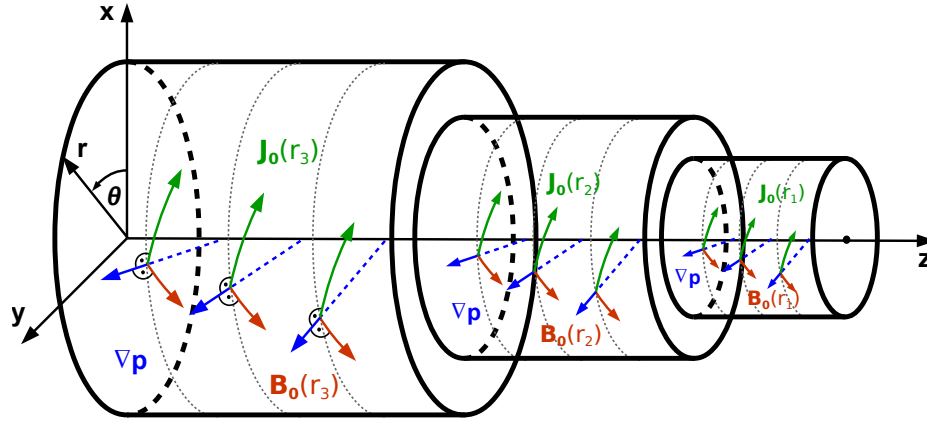


Figure 3.4. Sketch of the equilibrium situation. Three nested flux surfaces are drawn in cylindrical coordinates in 3D (for better visibility they are “pulled out” of each other). Current and magnetic field lie on this flux surface whereas the pressure gradient points outwards. For illustration purposes \mathbf{B}_0 and \mathbf{J}_0 are drawn with a large angle between them. Usually they are almost parallel.

⁵Note that we have to use vector calculus in cylindrical coordinates, see ref. [25].

3.2.2 Harmonic Perturbations

The perturbation of the equilibrium will be done in the same way as in the treatment in slab-geometry, namely (2.12)

$$\mathbf{B} = \mathbf{B}_0 + \delta\mathbf{B}.$$

The decomposition into FOURIER modes is a bit more tricky,

$$\delta\mathbf{B} = \tilde{\mathbf{B}}e^{i(m\theta+k_z z)}, \quad (3.8)$$

with

$$\mathbf{k} = k_\theta \mathbf{e}_\theta + k_z \mathbf{e}_z, \quad (3.9)$$

$$k_\theta = \frac{m}{r}, \quad (3.10)$$

$$k_z = \frac{n}{R_0}. \quad (3.11)$$

As usual, we denote m and n as the poloidal and toroidal mode numbers respectively. The components of the “wave vector” \mathbf{k} are then given by the ratio of the mode number and the corresponding length scale. As a result of k_θ having a radial dependence, we will only use m instead of k_θ in the exponential (3.8). This is still convenient, as can be shown by calculating the divergence of the perturbed magnetic field:

$$\begin{aligned} \nabla \cdot \delta\mathbf{B} &= \frac{1}{r} \partial_r (r \delta B_r) + \frac{1}{r} \partial_\theta \delta B_\theta + \partial_z \delta B_z, \\ &= \left[\frac{1}{r} \partial_r (r \tilde{B}_r) + i (\mathbf{k} \cdot \tilde{\mathbf{B}}) \right] e^{i(m\theta+k_z z)}. \end{aligned}$$

In cylindrical coordinates we have to use the corresponding divergence operator which gives us a prefactor of $1/r$ for the θ derivative. Applying this to the exponential we can write this as a scalar product of \mathbf{k} with the perturbed field. Generally we just have to keep in mind, that k_θ and \mathbf{k} have a radial dependence.

The divergence-freeness can be written immediately using our sample calculation above:

$$\frac{1}{r} \partial_r (r \tilde{B}_r) + i (\mathbf{k} \cdot \tilde{\mathbf{B}}) = 0. \quad (3.12)$$

The goal of this section is to use iMHD to derive an equation similar to (2.25). To achieve this, we again start at the perturbed ideal static pressure balance,

$$4\pi \nabla \delta p = (\mathbf{B}_0 \cdot \nabla) \delta\mathbf{B} + (\delta\mathbf{B} \cdot \nabla) \mathbf{B}_0 - \nabla (\mathbf{B}_0 \cdot \delta\mathbf{B}) + \mathcal{O}(\delta^2),$$

and apply our equilibrium (3.5) and our perturbation (3.8) to it. By defining the abbreviation

$$\mathbf{W} \equiv (\mathbf{B}_0 \cdot \nabla) \delta\mathbf{B} + (\delta\mathbf{B} \cdot \nabla) \mathbf{B}_0, \quad (3.13)$$

$$\mathbf{W} = \tilde{\mathbf{W}} e^{i(m\theta+k_z z)}, \quad (3.14)$$

we get

$$4\pi\nabla\delta p = \mathbf{W} - \nabla(\mathbf{B}_0 \cdot \delta\mathbf{B}). \quad (3.15)$$

The components of \mathbf{W} are given by evaluation of (3.13) in cylindrical coordinates:

$$\widetilde{W}_r = i\widetilde{B}_r(\mathbf{k} \cdot \mathbf{B}_0) - \frac{2}{r}B_{0\theta}\widetilde{B}_\theta, \quad (3.16)$$

$$\widetilde{W}_\theta = i\widetilde{B}_\theta(\mathbf{k} \cdot \mathbf{B}_0) + \frac{1}{r}B_{0\theta}\widetilde{B}_r + \widetilde{B}_r\partial_r B_{0\theta}, \quad (3.17)$$

$$\widetilde{W}_z = i\widetilde{B}_z(\mathbf{k} \cdot \mathbf{B}_0) + \widetilde{B}_r\partial_r B_{0z}. \quad (3.18)$$

The trick is now to apply the curl operator on (3.15). Since two terms are given as gradients of a scalar function, they vanish by a fundamental rule of vector calculus, leading to

$$\nabla \times \mathbf{W} = 0. \quad (3.19)$$

We evaluate this curl to get

$$k_\theta\widetilde{W}_\theta - k_z\widetilde{W}_z = 0, \quad (3.20)$$

$$ik_z\widetilde{W}_r - \partial_r\widetilde{W}_z = 0, \quad (3.21)$$

$$\frac{1}{r}\partial_r(r\widetilde{W}_\theta) - ik_\theta\widetilde{W}_r = 0. \quad (3.22)$$

This is now the central set of equations to solve. As for the slab-like case, one can extract an equation for the radial component of the magnetic field perturbation,

$$\partial_r\left(\frac{r}{k^2}\partial_r\widetilde{B}_r\right) - r\widetilde{B}_r\left[1 - \partial_r\left(\frac{1}{rk^2}\right) + F_p\right] = 0, \quad (3.23)$$

with the quantity

$$F_p = \frac{4\pi}{F}r\partial_r\left(\frac{1}{rk^2}\{\mathbf{k} \times \mathbf{J}_0\}_r\right) + \frac{2}{rk^2F}\left(\frac{4\pi k_z^2}{F}\partial_r p_0 + k_z\partial_r B_{0z}\right), \quad (3.24)$$

and the familiar scalar product

$$F = \mathbf{k} \cdot \mathbf{B}. \quad (3.25)$$

This equation was first given by FURTH, RUTHERFORD and SELBERG in [27]. The version found there can be converted into this one by some algebra. Exactly this version can also be found in the work of HEYN, et al. [37].

We can further evaluate (3.25):

$$F = k_\theta B_{0\theta} + k_z B_{0z} = \frac{m}{r}B_{0\theta} + \frac{n}{R}B_{0z} = \frac{nB_{0\theta}}{r}\left(\frac{m}{n} + \frac{rB_{0z}}{RB_{0\theta}}\right).$$

The second term in the bracket is exactly our definition of the safety factor (3.3) in this geometry. Since F is in the denominator of (3.24), we can write the condition for $F = 0$ as⁶

⁶Note that the exact relation depends on the sign of q which is defined by the convention used. This will determine if positive or negative mode numbers are resonant.

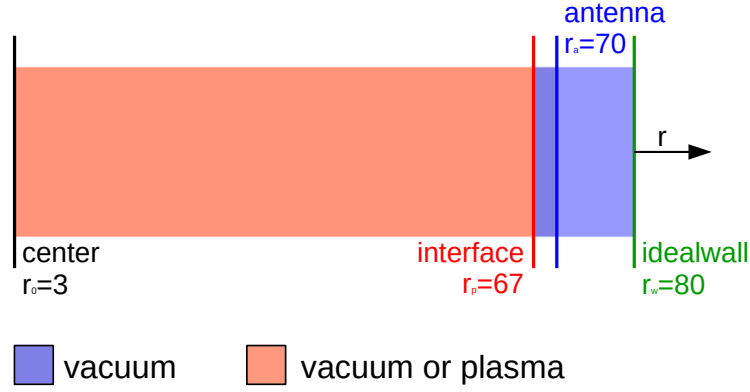


Figure 3.5. Configuration as described in the main text. All values are given in cm.

$$q_s = q|_{r=r_s} = -\frac{m}{n} = -q_r. \quad (3.26)$$

This means that we encounter singularities at surfaces $r = r_s$ where q is rational. We call this singularity *surface resonance*.

3.3 Kinetic Linear Model in Cylindrical Approximation

In the previous section we analyzed the perturbed equilibrium in terms of iMHD and found, as expected, singularities in the equations. The locations of these singularities coincide with the location of rational surfaces in terms of the safety factor. After the investigation of the slab-like case, the next logical step would be to divide our domain into outer and inner regions.

Instead of iMHD we will apply a *kinetic* model to the configuration to get a more precise understanding of the underlying physics. Furthermore we want to model static RMPs which we do by applying external perturbations to the system (antenna). At last, we will make our model more “realistic” by using appropriate boundary conditions (BC). An ideal wall ($\sigma \rightarrow \infty$) is placed at the very edge of the configuration. The used setup is shown in figure 3.5⁷. We call the different regions in the configuration *zones*.

3.3.1 RMP Modelling

The effect of static RMPs can be modeled by virtually putting a coil outside the plasma which we call “antenna” [37]. In the antenna a sheet-like current will flow and create the external perturbation field. The coil is modelled infinitesimal thin, which means that we only have poloidal and toroidal components in a single sheet:

$$\mathbf{J}^A = (J_\theta^A \mathbf{e}_\theta + J_z^A \mathbf{e}_z) e^{i(m\theta + k_z z)}, \quad (3.27)$$

$$J_\theta^A = I_\theta^A \delta(r - r_a), \quad (3.28)$$

$$J_z^A = I_z^A \delta(r - r_a). \quad (3.29)$$

⁷We exclude the most inner region near the magnetic axis because we have a singularity in our coordinate system there. The solution there should be replaced by the analytical solution of (3.23) in plasma away from resonances. This is similar to the vacuum solution that is shortly discussed in section 3.3.2.

This current is also decomposed into FOURIER modes since it is a perturbation to the equilibrium. It has to be divergence-free ($\nabla \cdot \mathbf{J}^A = 0$, RMPs are static), thus we get a relation between the components,

$$k_\theta J_\theta^A + k_z J_z^A = 0. \quad (3.30)$$

We include it into our analysis in AMPÈRE'S law,

$$\frac{1}{4\pi} \nabla \times \delta \mathbf{B} = \delta \mathbf{J} + \mathbf{J}^A, \quad (3.31)$$

which modifies our central equation (3.19):

$$\nabla \times \mathbf{W} = 4\pi i (J_\theta^A B_{0z} - J_z^A B_{0\theta}) (k_z \mathbf{e}_\theta - k_\theta \mathbf{e}_z) e^{i(m\theta + k_z z)}. \quad (3.32)$$

In the end (3.23) will get an additional inhomogeneity on the right hand side,

$$\partial_r \left(\frac{r}{k^2} \partial_r \tilde{B}_r \right) - r \tilde{B}_r \left[1 - \partial_r \left(\frac{1}{rk^2} \right) + F_p \right] = \frac{4\pi r}{ik_\theta} J_z^A. \quad (3.33)$$

3.3.2 Vacuum Solutions

First we want to consider solutions in vacuum which correspond to the standard case in the outer zones and to *no* plasma in the innermost zone. There we can take the iMHD equation (3.33) and set all “plasma-quantities” to zero. This means $F_p = 0$, since there is no current or pressure in vacuum (the r -derivative of B_{0z} is connected to a current via AMPÈRE'S law). We do not consider the antenna current directly in the equation but rather split the domain into “inside” and “outside” the antenna. The solutions for the magnetic field in these regions are then connected by a jump condition at the antenna due to the current. Thus, the equation for \tilde{B}_r in vacuum is

$$\partial_r \left(\frac{r}{k^2} \partial_r \tilde{B}_r \right) - r \tilde{B}_r \left[1 - \partial_r \left(\frac{1}{rk^2} \right) \right] = 0. \quad (3.34)$$

This equation is BESSEL-like but does not have the standard form and to find a corresponding solution will be quite sophisticated. Thus we can make a shortcut by starting again from magnetostatic MAXWELL'S equations in vacuum,

$$\nabla \times \delta \mathbf{B} = 0, \quad (3.35)$$

$$\nabla \cdot \delta \mathbf{B} = 0. \quad (3.36)$$

The first one yields three relations for all the field components:

$$k_\theta \tilde{B}_z - k_z \tilde{B}_\theta = 0, \quad (3.37)$$

$$ik_z \tilde{B}_r - \partial_r \tilde{B}_z = 0, \quad (3.38)$$

$$\frac{1}{r} \partial_r (r \tilde{B}_\theta) - ik_\theta \tilde{B}_r = 0. \quad (3.39)$$

The second one can be combined with (3.37) and (3.38) to directly yield a *modified* BESSEL equation in *standard form* for \tilde{B}_z in the variable $k_z r$:

$$r^2 \partial_r^2 \tilde{B}_z + r \partial_r \tilde{B}_z - (m^2 + r^2 k_z^2) \tilde{B}_z = 0. \quad (3.40)$$

Solutions *inside* the antenna are given by e.g. ref. [38] (§10.25) and by (3.37) and (3.38):

$$\tilde{B}_z = CI_m(k_z r), \quad \tilde{B}_\theta = C \frac{k_\theta}{k_z} I_m(k_z r), \quad \tilde{B}_r = -C \frac{i}{k_z} \partial_r I_m(k_z r). \quad (3.41)$$

The function I_m is a modified BESSEL function of first kind,

$$I_m(k_z r) = \left(\frac{1}{2} [k_z r]\right)^m \sum_{k=0}^{\infty} \frac{\left(\frac{1}{4} [k_z r]^2\right)^k}{\Gamma(k+1) \Gamma(k+m+1)}, \quad (3.42)$$

with complex constant C which has to be identified to match the BCs. The last thing we want to consider is the small argument limit⁸ that should hold approximately since k_z is very small and r is limited by the small radius a . Via recursion relations one can define the derivative of I_m (see [38] §10.29) as the sum of the two “neighbouring” (with next smaller and next larger m) modified BESSEL functions⁹. Keeping only the first terms of both series expansions (3.42) we get

$$\tilde{B}_r \approx C_1 r^{m+1} + \frac{C_2}{r} r^m \xrightarrow{k_z r \rightarrow 0} \propto r^{m-1}. \quad (3.43)$$

Both $C_{1,2}$ are again complex constants. This shows that \tilde{B}_r follows an approximate $m-1$ power-law in vacuum. In the above treatment we implicitly assumed our domain *inside* the antenna. Outside, also the modified BESSEL functions of second kind K_m are allowed¹⁰. In general these have an exponentially decreasing behaviour.

By now we only considered the general structure of the solutions in vacuum. One can get the full solution by matching BCs and splitting the domains. In plasma (3.34) can be solved outside the resonances by reintroducing F_p . The exact details are not relevant for this work and will not be sketched here.

3.3.3 Kinetic Plasma Response

The model that will be briefly described here was developed in [39, 40] and implemented in a code with the name *KiLCA* (Kinetic Linear Cylindrical Approximation). A short overview shall be given.

The starting point is the plasma kinetic equation,

$$\frac{\partial f}{\partial t} + \mathbf{v} \cdot \nabla_{\mathbf{r}} f + \frac{e}{m} (\mathbf{E} + \mathbf{v} \times \mathbf{B}) \cdot \nabla_{\mathbf{v}} f = \left(\frac{\partial f}{\partial t}\right)_{\text{col}}, \quad (3.44)$$

for a particle distribution function $f = f(\mathbf{r}, \mathbf{v}, t)$. In the round brackets, the LORENTZ-force is considered to act on the particles. The left side corresponds to the total time derivative of f which can only change by collisions, described by the right side. The collisions are commonly modeled by different collision operators,

$$\left(\frac{\partial f}{\partial t}\right)_{\text{col}} = L_{\text{col}} f, \quad (3.45)$$

⁸This is especially good for large m modes, because the second term in the bracket of (3.40) can then be neglected and we get an EULER ODE for \tilde{B}_z .

⁹For completeness $\partial_r I_m(k_z r) = I_{m+1}(k_z r) + \frac{m}{k_z r} I_m(k_z r)$ was used here.

¹⁰These would diverge at zero and thus are no solution inside the antenna.

where the choice of the collision operator will generally affect the physics of the problem (whether the operator conserves particle number, energy, momentum, etc. nor not).

The collision operator first used in KiLCA was the KROOK collision operator that conserves neither particles, energies or momenta (but it is simple) [39]. Especially it violates GALILEAN invariance which turned out to be problematic because the code did calculations in a moving frame (reasons will follow). In ref. [40] the operator was changed to a FOKKER-PLANCK type collision operator which conserves particle number and keeps GALILEAN invariance of the distribution function.

Solution of the Kinetic Equation: The kinetic equation (3.44) can be analytically solved in linearized form to yield the perturbed distribution function defined by $f = f_0 + \tilde{f}$. The solution includes a source term $\tilde{Q} = \tilde{Q}(\tilde{\Phi}, \tilde{\mathbf{A}})$ that depends on the perturbed potentials. Using *radiation gauge*, one can set $\tilde{\Phi} = 0$ and the electric field solely depends on the perturbed vector potential (which is again decomposed into separated harmonics) by

$$\tilde{\mathbf{E}} = i\omega\tilde{\mathbf{A}}, \quad (3.46)$$

$$\tilde{\mathbf{A}} = \tilde{\mathbf{A}}(r) e^{i(m\theta + k_z z - \omega t)}. \quad (3.47)$$

The external perturbations are *static* ($\omega = 0$) which does not allow us to solve for the electromagnetic fields. By reason of this, one can switch to a *moving frame* (in z) where the fields are again time-dependent. This velocity is chosen non-relativistic, thus the transition is done by GALILEAN transformation. In the end the current has to be transformed back to the laboratory frame which forces the use of an GALILEAN invariant collision operator.

Given $\tilde{\mathbf{A}}$, the formal expression for \tilde{Q} contains $\tilde{\mathbf{E}}$ which can be expanded in terms of finite LARMOR radii (FLRE)¹¹. Next, the perturbed distribution function can be found and the first moment in velocity space¹² yields the perturbed current density $\tilde{\mathbf{J}} = \tilde{\mathbf{J}}(\boldsymbol{\sigma})$, where $\boldsymbol{\sigma}$ is the *conductivity operator*. KiLCA will first compute the conductivity operator $\boldsymbol{\sigma}$ and then $\tilde{\mathbf{J}}$.

Electromagnetic Field: Once the plasma response current has been evaluated, the remaining task is to compute the EM field perturbation by using MAXWELL'S equations (in FOURIER space):

$$\nabla \times \tilde{\mathbf{E}} = i\omega\tilde{\mathbf{B}}, \quad (3.48)$$

$$\nabla \times \tilde{\mathbf{B}} = -i\omega\tilde{\mathbf{E}} + 4\pi(\tilde{\mathbf{J}}_p + \tilde{\mathbf{J}}_a). \quad (3.49)$$

The difference to the usual form of these equations is the extra term in AMPÈRE'S law that now includes the plasma response current $\tilde{\mathbf{J}}_p$ and additionally the external antenna current $\tilde{\mathbf{J}}_a$. In the cylinder, these equations boil down to ODEs for the single harmonics, dependent on r . They are solved together with the BC at the antenna, ideal wall, center and at the interface between plasma and vacuum (last closed flux surface).

¹¹This is done to include effects that are perpendicular to the direction of the magnetic field. Otherwise the integration over the gyrophase in the end would not include such effect when the position is evaluated at the gyrocenter only.

¹²The integration over the gyrophase has to be done by introducing a second FLRE. The result will contain two expansions.

3.4 Application of KiLCA to a Test Case

To investigate some general properties of the solutions in this configuration, a simple artificial test case was constructed. This should exclude additional effects of real shots like the pedestal region or fluid resonances. These will be used in the next section.

3.4.1 Profiles & Equilibrium

The profiles were generated as parabolic decreasing profiles for temperatures and density with real magnitudes and geometric parameters for AUG shots. The following functional form was used,

$$n = n_0 \left(1 - \left(\frac{r}{r_0} \right)^2 \right), \quad T_e = T_{e0} \left(1 - \left(\frac{r}{r_0} \right)^2 \right), \quad T_i = T_{i0} \left(1 - \left(\frac{r}{r_0} \right)^2 \right), \quad (3.50)$$

with $n_0 = 3.5 \cdot 10^{13} \text{ cm}^{-3}$, $T_{i0} = 5 \text{ keV}$, and $T_{e0} = 7 \text{ keV}$ (corresponding to values at the center). The plasma radius is $r_0 = 67 \text{ cm}$, antenna radius $r_a = 70 \text{ cm}$, ideal wall radius $r_w = 80 \text{ cm}$ and large torus radius $R_0 = 170 \text{ cm}$. The safety factor has a quadratic increasing form (starting at 1) with overall negative sign due to the used coordinate convention¹³,

$$q = - \left(1 + q_0 \left(\frac{r}{r_0} \right)^2 \right), \quad (3.51)$$

with $q_0 = 5^{14}$. Radial electric field profile was set to zero everywhere and the equilibrium velocity components were calculated by the code consistently with the other inputs. All profiles can be seen in figure 3.6. The perpendicular electron velocity is given additionally, to show that no fluid resonances ($v_{e\perp} = 0$) occur for our test profiles.

The equilibrium magnetic field and current density components can be seen in figure 3.7 and 3.8 respectively. The toroidal magnetic field magnitude at the center was chosen to be $\approx -1.7 \cdot 10^4 \text{ G}$. The sign matches the coordinate convention.

3.4.2 Vacuum Perturbations & Plasma Response

Now the antenna can be switched on. The configuration was chosen as in figure 3.5 and the total current in the antenna $I_0 = 150 \text{ statA}$ in units of c (1.5 kA). In the first run we want to consider the case with vacuum in the most inner zone. Results for the magnetic field and current density perturbations can be seen in figure 3.9 and 3.10 respectively.

Inside the antenna the perturbed magnetic field components increase by approximately a power law from the center up to the antenna (3.43). Since there is no plasma in these runs, there is no effect of the resonance. At the outside of the antenna, \tilde{B}_r falls off and matches the classical EM BC at the ideal wall, namely the normal magnetic field must vanish. The other components have a discontinuity at the antenna that is due to the current in the coils. These currents can be seen in figure 3.10. In the rest of the vacuum regions, all components of the current can be seen as zero.

The situation changes when putting plasma inside the innermost zone (figure 3.11). Inside the antenna, first all components fall off again (\tilde{B}_θ and \tilde{B}_z feel the transition between vacuum and plasma near

¹³This will lead to resonances appearing at $q = +\frac{m}{n}$.

¹⁴The parameter q_0 is linked to q at the plasma radius by: $q_0 = q(r_0) - 1$.

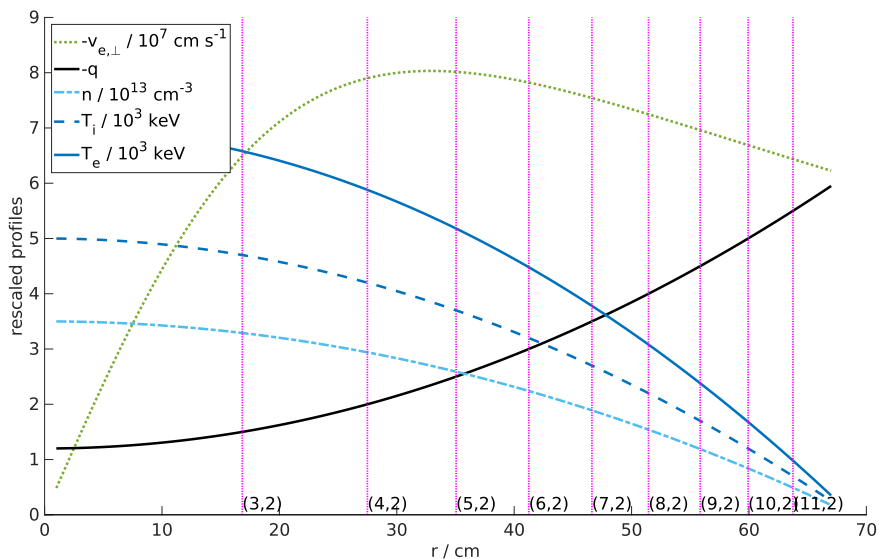


Figure 3.6. test profiles used for KiLCA runs. Quantities were rescaled by their succeeding exponentials to cover only one order of magnitude in the plot. Safety factor and perpendicular electron fluid velocity is shown as its negative. Vertical lines show the positions of the main rational surfaces for $n = 2$ given the safety factor profile.

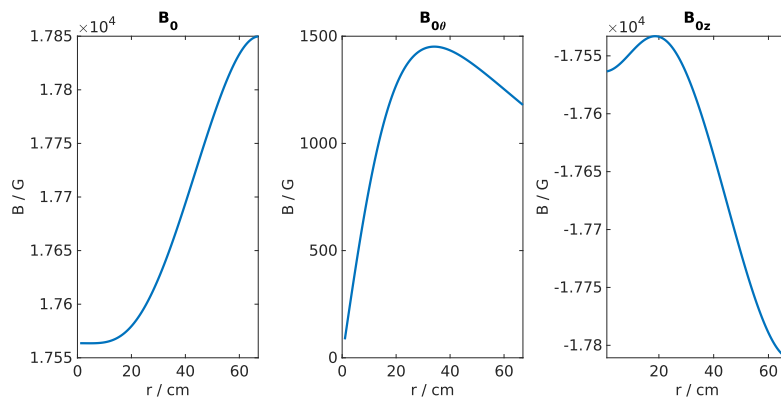


Figure 3.7. Equilibrium magnetic field for given test profiles. Shown is the magnitude, the poloidal and toroidal component of \mathbf{B}_0 respectively.

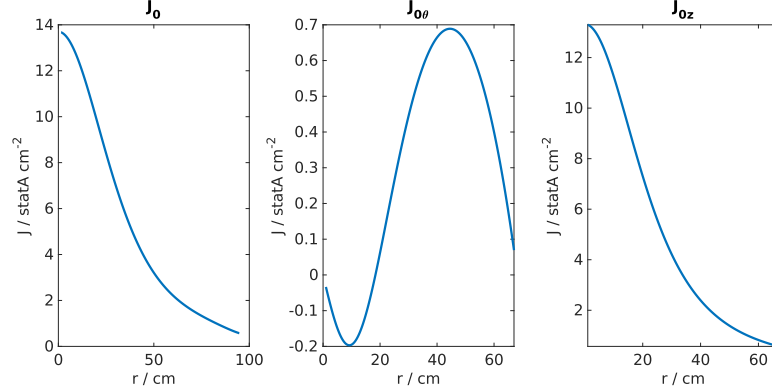


Figure 3.8. Equilibrium current density for given test profiles. Shown is the magnitude, the poloidal and toroidal component of \mathbf{J}_0 respectively.

the antenna¹⁵). Further inside, the magnetic field gets shielded by sheet-like currents on the resonant surface (figure 3.12). The radial field stays continuous whereas \tilde{B}_θ and \tilde{B}_z tend to have¹⁶ a discontinuity there¹⁷. Inside the resonant surface there is hardly any effect of the external perturbation present. The magnitude of the radial current is some orders smaller than the other components because it is substantially harder to move particles against the (equilibrium) magnetic field lines than along them.

3.4.3 Analysis of Shielding in the Test Case

The previously described shielding is of great interest. For this test case we can make at least a qualitative analysis by plotting both, the vacuum and plasma response radial fields for different modes (figure 3.13). All calculated modes are shielded in this case. A better figure of merit is the *form factor* evaluated at the position of the resonant surface,

$$T_s = \frac{\left| \tilde{B}_r^{\text{plas}} \right|}{\left| \tilde{B}_r^{\text{vac}} \right|} \Bigg|_{r=r_s}. \quad (3.52)$$

We can plot these values for different modes at the location where the resonance occurs (figure 3.14). This confirms our initial observation that all modes are strongly shielded (factor 100 here). At the edge, shielding decreases due to the higher collisionality. This matches to the simple two-fluid estimation we did in the introduction (1.9).

¹⁵This is due to the rapid change of finite density to $n = 0$ in the vacuum.

¹⁶They cannot have a “real” discontinuity because the model of KiLCA is not iMHD and the current sheet has finite width.

¹⁷There are some oscillations, probably due to ALFVÉN resonances near the surface resonance.

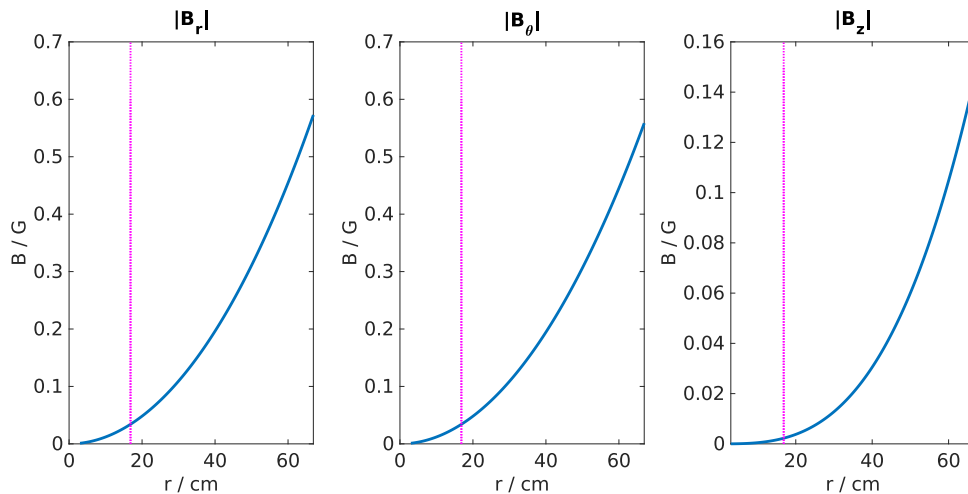


Figure 3.9. Vacuum magnetic field perturbation for $m = 3, n = 2$. Shown is the absolute value of all components (blue) and the location of the resonant region (pink).

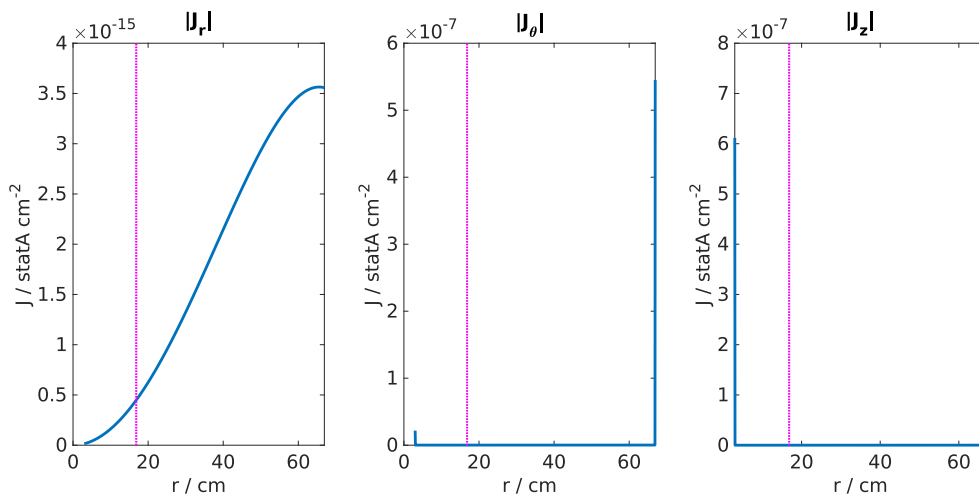


Figure 3.10. Vacuum current density perturbation for $m = 3, n = 2$. Shown is the absolute value of all components (blue) and the location of the resonant region (pink).

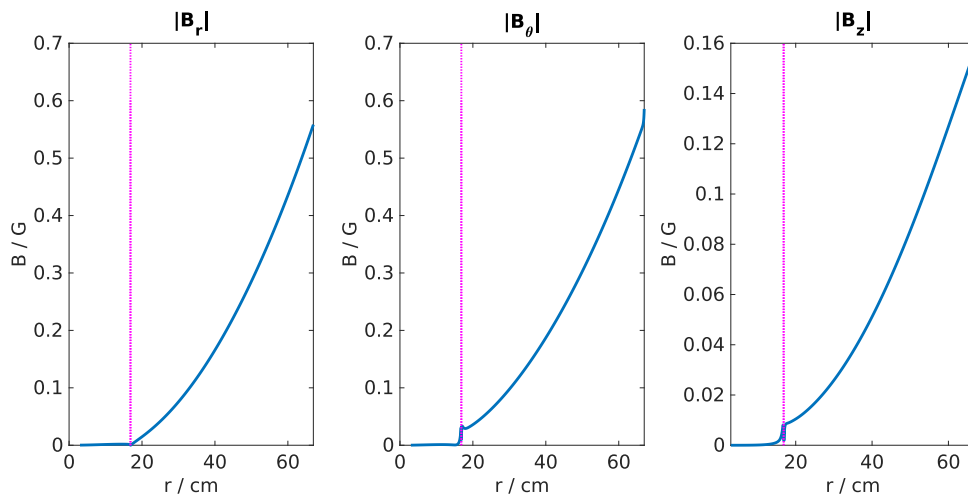


Figure 3.11. Total magnetic field perturbation with plasma response for $m = 3, n = 2$. Shown is the absolute value of all components (blue) and the location of the resonant region (pink).

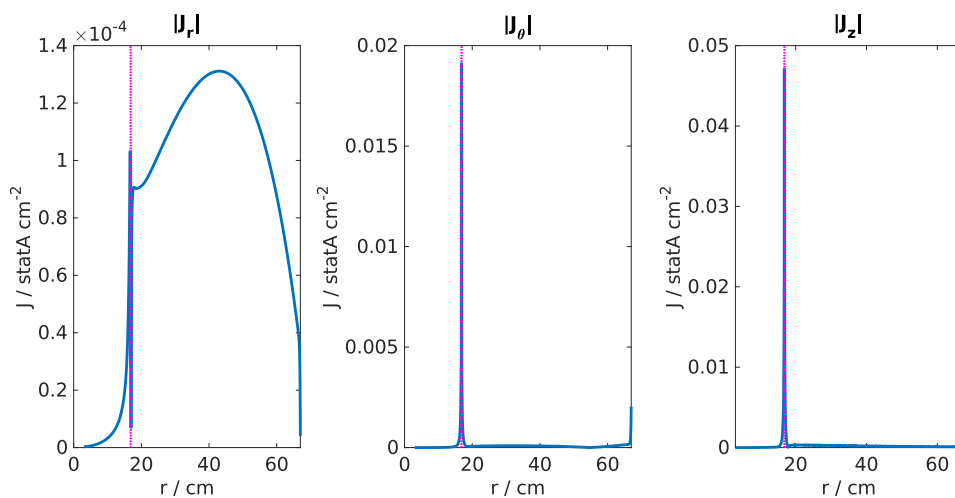


Figure 3.12. Total current density perturbation with plasma response for $m = 3, n = 2$. Shown is the absolute value of all components (blue) and the location of the resonant region (pink). The plots for the poloidal and toroidal components are zoomed in to see the rather smaller sheet currents.

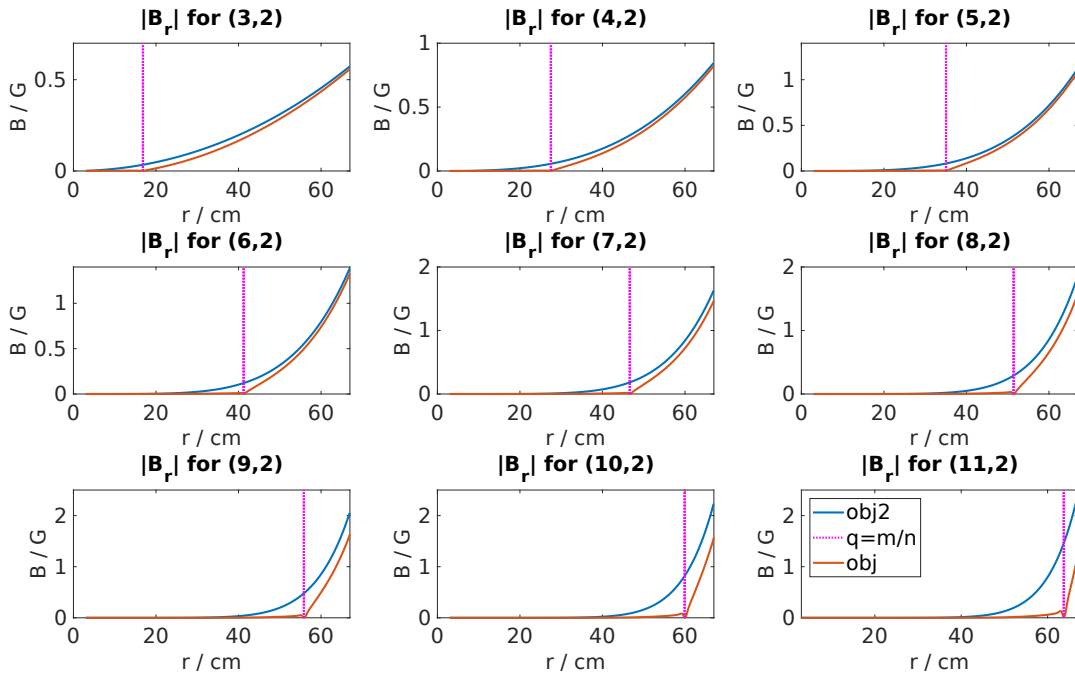


Figure 3.13. Absolute radial magnetic field perturbation in vacuum and with plasma response for different poloidal modes and $n = 2$. The vertical line shows the location of the resonant surface.

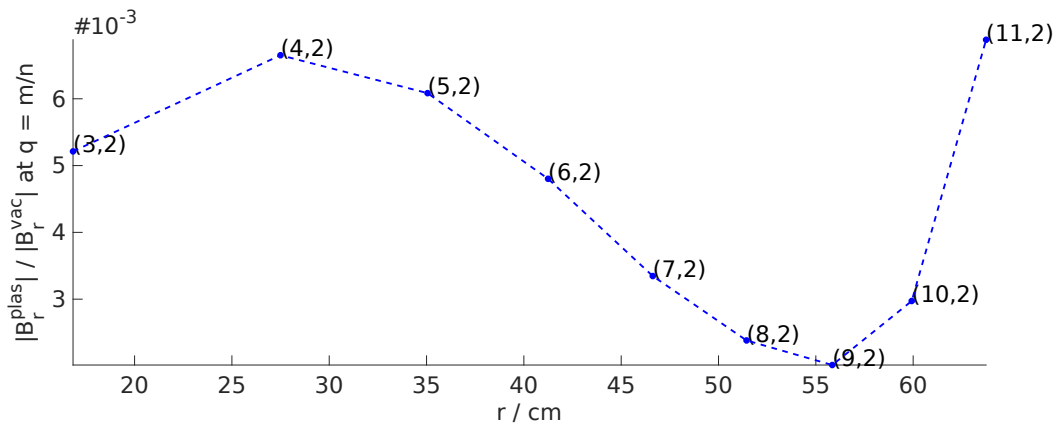


Figure 3.14. Form factors at the position of the resonant surface for different poloidal modes and $n = 2$. Strong shielding (about factor 100) can be observed.

3.4.4 Poincaré Plots

These kind of plots represent cuts through real space where particles move along their trajectories. The result are points where these trajectories cross the plane that is cut through. To do this, we put test particles inside the cylinder and let them move along the magnetic field lines. Each time the particle reaches the end of the cylinder $z = 2\pi R_0$, we put it back at $z = 0$ and save the radial and poloidal position of it as a point. We do this for different starting positions and map until a certain number of turns is reached.

Mapping: To do the field line tracing, we start again with the equation of a magnetic field line (section 2.1.6, [26]), now in cylindrical coordinates:

$$\frac{dr}{B^r} = \frac{d\theta}{B^\theta} = \frac{dz}{B^z}. \quad (3.53)$$

Notice that we have to use the contravariant components of the vector field \mathbf{B} since they do not coincide with the physical ones as in slab-like geometry. They are related by

$$\hat{B}_r = B^r, \quad \hat{B}_\theta = rB^\theta, \quad \hat{B}_z = B^z. \quad (3.54)$$

We can write two equations for the r - and θ -coordinate of the field line as

$$\frac{dr}{dz} = \frac{\hat{B}_r}{\hat{B}_z}, \quad \frac{d\theta}{dz} = \frac{\hat{B}_\theta}{r\hat{B}_z}. \quad (3.55)$$

First we will consider only the equilibrium. In that case we have $\hat{B}_r = 0$ and we can write using the definition of the safety factor (3.3),

$$\frac{dr}{dz} = 0, \quad \frac{d\theta}{dz} = \frac{1}{qR_0}. \quad (3.56)$$

Integrated over z we get the equilibrium mapping as

$$r = r_0, \quad \theta = \theta_0 + q^{-1} \frac{z}{R_0}. \quad (3.57)$$

This means that the field line will stay on the same radius forever, and the poloidal angle will turn with increasing z according to the toroidal winding number $\iota = 2\pi q^{-1}$. The Poincaré plot will only contain nested circles. This fits perfectly with our expectations for the equilibrium.

Now we will treat the full magnetic field that consists of the equilibrium field and the perturbed field. Our field line equations read:

$$\frac{dr}{dz} = \frac{\delta B_r}{B_{z0} + \delta B_z}, \quad \frac{d\theta}{dz} = \frac{B_{\theta0} + \delta B_\theta}{r(B_{z0} + \delta B_z)}. \quad (3.58)$$

Formally we can write the mapping by integration as

$$r = r_0 + \int dz \frac{\delta B_r}{B_{z0} + \delta B_z}, \quad \theta = \theta_0 + \int dz \frac{B_{\theta0} + \delta B_\theta}{r(B_{z0} + \delta B_z)}. \quad (3.59)$$

Practically we have to evaluate these integrals numerically. There are two important things to consider when doing this. First, the perturbed field components are generally complex numbers where the

imaginary part represents a phase shift between the quantities. When taking the physical fields as written above, we have to choose a particular phase¹⁸,

$$\operatorname{Re}(\delta B_r) = \operatorname{Re}\left(\tilde{B}_r e^{i(m\theta + k_z z)}\right) = \operatorname{Re}\left(\tilde{B}_r\right) \cos(m\theta + k_z z) - \operatorname{Im}\left(\tilde{B}_r\right) \sin(m\theta + k_z z).$$

Second, all quantities in the mapping do have explicit z -dependence in the trigonometric functions only. Naïvely integrating the field line equation (3.58) at once does result in the exact same plot as in the equilibrium case. This is because the contributions from the trigonometric functions do cancel upon integration over one full interval. The correct way to do this is considering the implicit z -dependence of the quantities in (3.58). Since r and θ will change for each z -step according to (3.59), the fields themselves have to be evaluated gradually when integrating along z . We have to follow the field line and recalculate the map each time we reach a new point.

Application: Poincaré plots for both, vacuum and plasma response can be seen in figure 3.15 and 3.16 ($z = 0$). The magnetic field off all modes has been superposed together with the equilibrium field for these calculations. Hence, we can see magnetic islands at different radii that can be counted along the circles to get the corresponding perturbation mode number¹⁹. Since the magnetic field perturbation increases radially outwards, the width of the islands does too (remember section 2.1.6, (2.65)). At the border of the plasma, the perturbation gets so strong that field lines start to become ergodic.

For the case of a responding plasma, islands vanish. This is perfectly consistent with the shielding of the perturbation found in the last section.

Toroidal Behaviour: The Poincaré plots shown before represent the cut-through of magnetic field lines for a particular z -plane. The topology in the r, θ -plane was found to be nested circles with or without magnetic islands in between. In 3D the nested circles will form nested cylinders. Magnetic islands instead, will form “tubes” that wind around the cylinder with radius $r = r_s$.

This can be seen in figure 3.17, where the test particles that trace the field lines are drawn in 3D. For better visibility this was done only for a single mode $m = 3$, $n = 2$ starting from the resonant surface $r = r_s$ ²⁰. To see the toroidal behaviour, the islands at $z = 0$ have been fitted and combined with a winding in z -direction. The resulting surfaces have been drawn, together with the described underlying cylinder, additionally to the points. Note that a cut through any $z = \text{const.}$ surface results in an individual Poincaré plot.

¹⁸The last equality sign can be evaluated by writing both \tilde{B}_r and the exponential in their complex form using real and imaginary part.

¹⁹There is a detail concerning even mode numbers: it can be the case, that half of the islands are topologically disconnected from the other ones. By putting only one particle per radius in, only half of the islands will be traced. To get the other half one has to put in a second particle which is shifted by $\frac{m\pi}{2}$ in angle. This has been done for these plots to get all islands.

²⁰To see only the effect of the equilibrium field, one can have a look at figure 3.3 which was used to show the meaning of the safety factor (section 3.1).

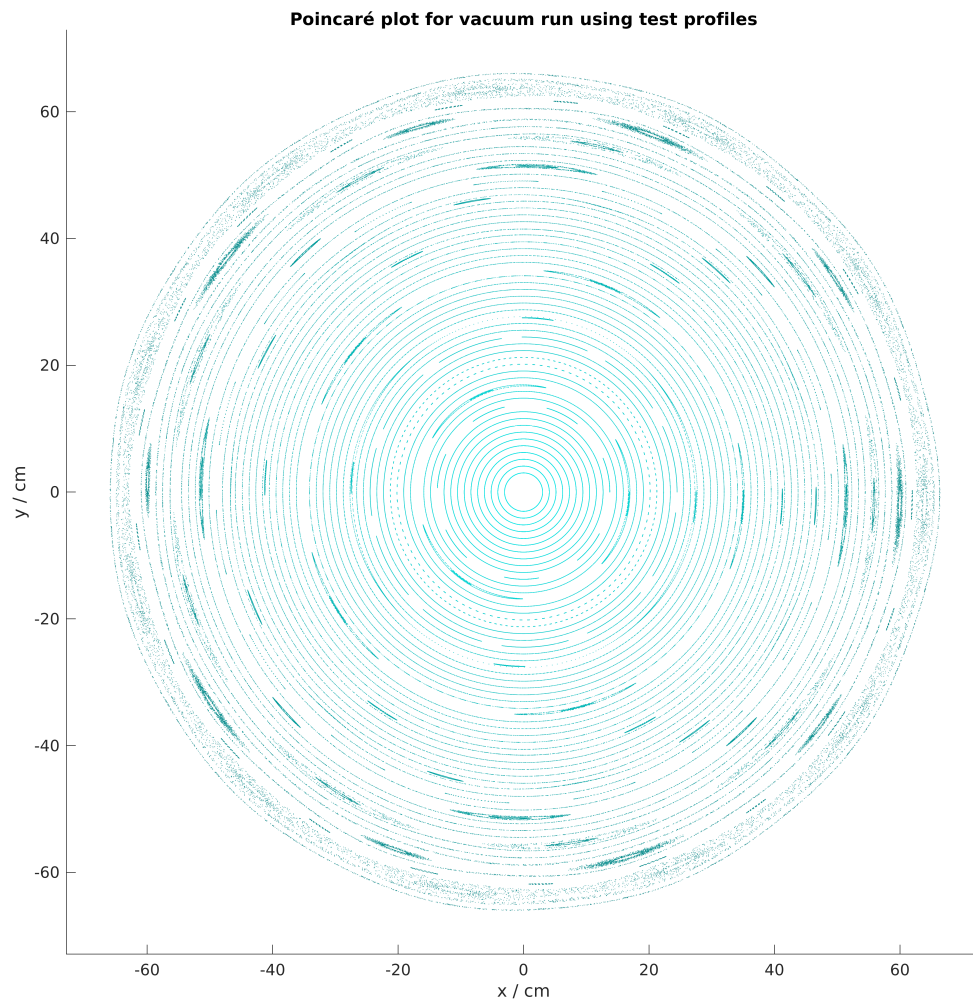


Figure 3.15. Poincaré plot for vacuum perturbation with modes $m \in [3, 11]$ and $n = 2$ (3000 mappings).

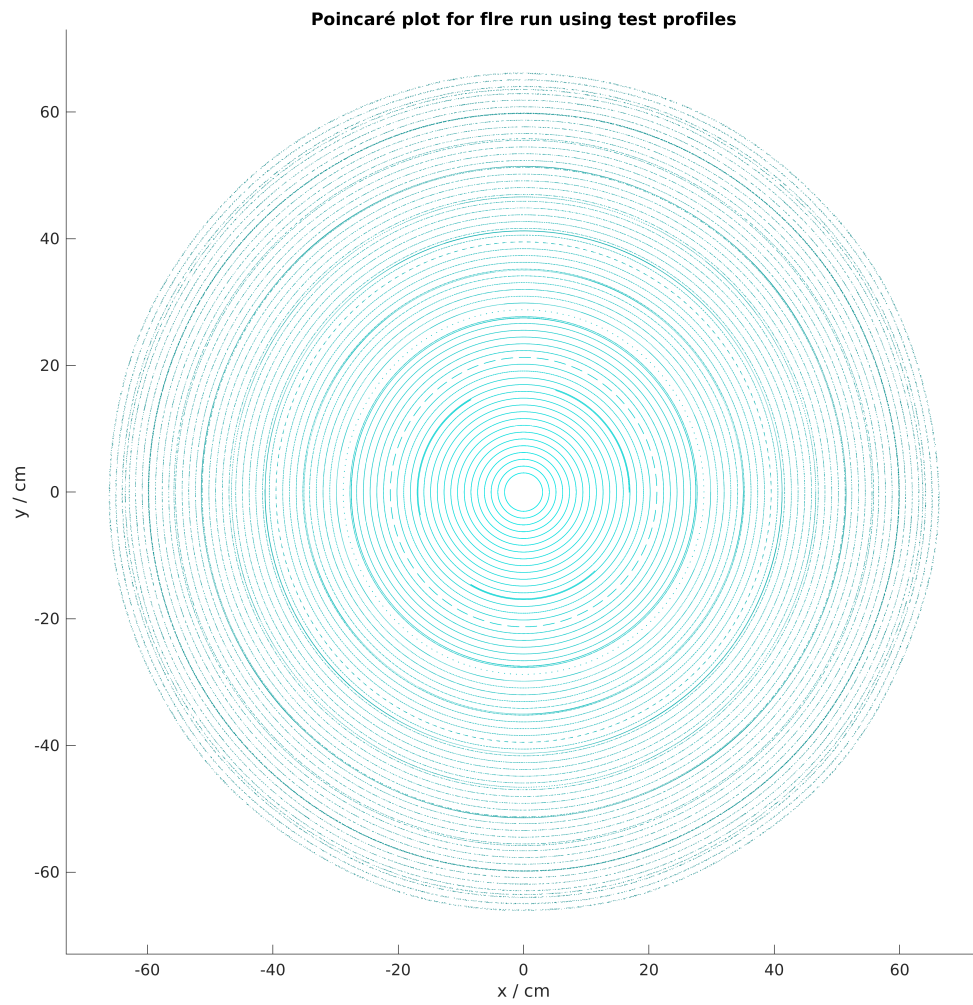


Figure 3.16. Poincaré plot for plasma response with modes $m \in [3, 11]$ and $n = 2$ (3000 mappings).

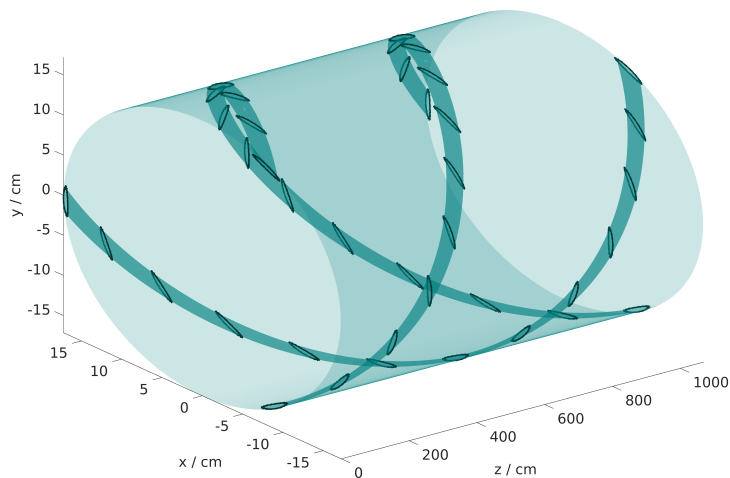


Figure 3.17. 3D plot of test particles tracing the magnetic field lines for a single mode $m = 3, n = 2$, starting from the resonant surface. The underlying cylinder has been included, as well as the tubes described in the main text. The size of the magnetic islands was amplified by a factor 100 for better visualization in this plot.

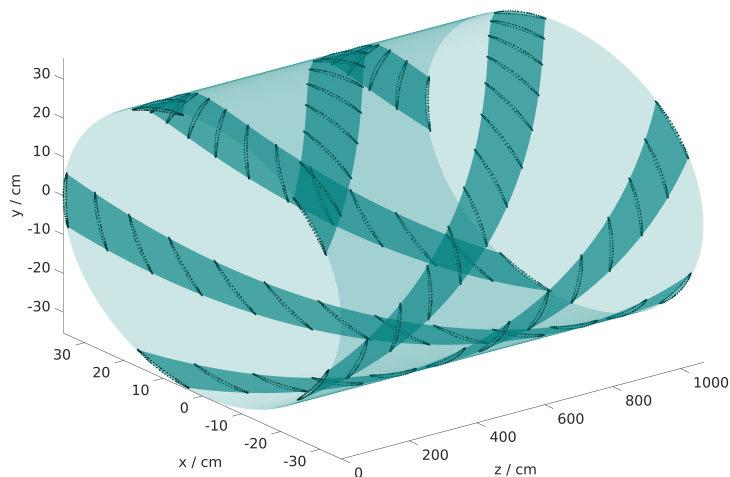


Figure 3.18. Same as figure 3.17 for $m = 5, n = 2$.

Chapter 4

Estimation of the Bifurcation Threshold

In previous unpublished work by M. F. HEYN and S. V. KASILOV it was seen that a ramp up of the coil current in their quasilinear model causes a bifurcation at a level of the quasilinear diffusion coefficient close to the anomalous diffusion coefficient, $D_{e22}^{\text{QL}} \approx 0.6D_{e22}^a$ ¹.

The rest of this thesis is dedicated to further investigate the occurrence of bifurcations and to find a criterion if bifurcation has happened or not. First, the physical as well as the computational model will be discussed. Afterwards, it will be applied to experimental data on selected AUG shots.

4.1 Physical Model

The model presented here is based on a quasilinear approach previously done in [21]. Quasilinear means, that the kinetic equation is expanded in terms of a small perturbation. The 0th order equation coincides with the equilibrium equation which solution is (usually) taken as a drifting Maxwellian. In the linear order, currents and charges are computed which are inserted into the MAXWELL equations. Finally, second order gives quasilinear equations which are of diffusive type and quadratic in amplitude of the perturbation. Solving these yields the evolution of the equilibrium in time.

4.1.1 Transport Equations

Transport equations are conservation laws that link the time evolution of density, temperature and other quantities with fluxes. The fluxes I_k can further be linked to the gradients of these quantities by diffusion coefficients D_{kj} [41],

$$I_k = -n \sum_j D_{kj} A_j, \quad (4.1)$$

where A_j denote *thermodynamic forces*. If we are not interested in the parallel flow, we can write the physical fluxes as

¹Private conversation with S. V. KASILOV in 2019.

$$I_1 = \Gamma, \quad I_2 = \frac{Q}{T}, \quad (4.2)$$

where Γ and Q are particle and heat flux respectively. The thermodynamic forces² are:

$$A_1 = \frac{\partial_r n}{n} - \frac{eE_r}{T} - \frac{3}{2} \frac{\partial_r T}{T}, \quad A_2 = \frac{\partial_r T}{T}. \quad (4.3)$$

Equations (4.1) are valid for both, electron and ion fluxes and thermodynamic forces. A quick view at (4.2) and (4.3) tells us that the diffusion coefficient D_{e22} links the electron heat flux with the electron temperature gradient,

$$Q_e \sim n D_{e22} \partial_r T_e. \quad (4.4)$$

We are interested in D_{e22} in particular, because the electron temperature gradient profile determines the electron diamagnetic velocity (1.12) which in turn changes the perpendicular electron fluid velocity by (1.11).

According to (1.9), the perpendicular electron fluid velocity plays an important role in the shielding of RMPs. The evolution of the temperature profile given by the transport equations may shift this velocity further to a point of the fluid resonance where the shielding current breaks down.³

Total Diffusion Coefficients: In ref. [21], quasilinear diffusion coefficients are calculated from the electromagnetic field. The diffusion coefficient D_{e22} is written as the sum of a quasilinear and an anomalous part:

$$D_{e22}^{\text{tot}} = D_{e22}^{\text{QL}} + D_{e22}^a. \quad (4.5)$$

One of the main results of quasilinear theory is the link of the diffusion coefficient with the square of the perturbed radial magnetic field amplitude:

$$D_{e22}^{\text{QL}} \sim \tilde{B}_r^2. \quad (4.6)$$

The overall calculation can be sketched as follows: The EM fields are computed for given profiles by KiLCA (section 3.3). This yields the quasilinear part of the total diffusion coefficients which adds up to the total diffusion coefficient D_{e22}^{tot} which furthermore is used in the transport equations for the time evolution of the background profiles n, T_e, T_i and v_z . These in turn change the EM fields, which change D_{e22}^{QL} again. This calculation can be resumed as long as the perturbations do not become too large for the quasilinear approach to break down. The described process matches with the qualitative picture that bifurcation occurs at a point where $D_{e22}^{\text{QL}} \sim D_{e22}^a$.

²Here we neglect the third thermodynamic force A_3 .

³Note that this is not the only mechanism that may happen according to section 1.2.3.

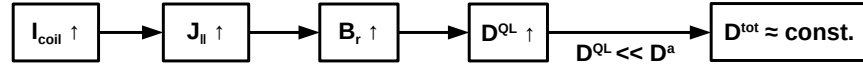
4.1.2 How RMPs Cause Bifurcation

The effect of an RMP as modelled in the quasilinear analysis can essentially be divided into three different phases. We assume that the RMP has been established and a shielding current has been generated by the plasma to diminish the effect of the external field perturbation (unbifurcated state). Governing relations for this are (1.9) $(J_{\parallel} = \sigma v_{e\perp} \tilde{B}_r)$, (4.6), (4.5) and $v_{e\perp} \sim \partial_r T_e, \partial_r n, \partial_r \Phi$ (from (4.1) for given profiles and fluxes). The three phases of bifurcation are:

- a) In the ramp up phase, the current in the RMP coils is ramped up from its initial value. Because there is still no bifurcation, this has very limited effect on the perturbed magnetic field. The quasilinear diffusion coefficient is very small compared to the anomalous one, thus the total diffusion coefficient stays approximately constant.
- b) At some point the feedback phase starts. The quasilinear diffusion coefficient becomes comparable to the anomalous one and the total diffusion coefficient starts to grow. This leads to decreased gradients, which in turn decrease the perpendicular electron fluid velocity. Because the shielding current stays approximately constant in this phase, the decrease in $v_{e\perp}$ results in an *positive feedback loop* as of 1.9, the perturbed field can increase further. This mechanism can shortly become very strong thus leading to an abrupt transition to the bifurcated state (one can imagine that $v_{e\perp}$ is brought closer to the fluid resonance in each turn of the feedback loop).
- c) Finally, the non-linear phase starts as the shielding current will break down and magnetic islands grow to a size comparable to the resistive layer width.

The non-linear phase limits the applicability of our model, thus we can only describe the *set on* of the bifurcation (phase (a) + (b)). A flow chart summarizing both relevant phases is given in figure 4.1.

a) Ramp-up phase:



b) Feedback phase: $B_r > B_{crit}, D^{QL} \sim D^a$

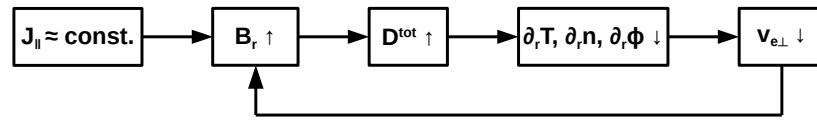


Figure 4.1. Flow chart describing phase (a) and (b) of the bifurcation.

4.1.3 Bifurcation Threshold

We can describe the abrupt change from the ramp up phase to the feedback phase (the bifurcation) by the following model for the perpendicular electron fluid velocity:

$$v_{e\perp} = v_{e\perp 0} \frac{D_{e22}^a}{D_{e22}^a + D_{e22}^{QL}}. \quad (4.7)$$

For $D_{e22}^{QL} \ll D_{e22}^a$ (ramp up phase), this stays approximately constant whereas for $D_{e22}^{QL} \geq D_{e22}^a$ it starts to decrease. With the quasilinear result of (4.6) we can rewrite this model in terms of the radial magnetic field perturbation,

$$v_{e\perp} = v_{e\perp 0} \frac{1}{1 + \left(\frac{\tilde{B}_r}{B_{\text{crit}}}\right)^2}, \quad (4.8)$$

where B_{crit} gives a critical amplitude for bifurcation to occur. In our simple two-fluid estimation (1.9), this links the magnetic field perturbation of two succeeding time steps k by

$$\tilde{B}_r^{(k+1)} = \frac{J_{\parallel}}{\sigma v_{e\perp 0}} \left[1 + \left(\frac{\tilde{B}_r^{(k)}}{B_{\text{crit}}}\right)^2 \right]. \quad (4.9)$$

For the ramp up phase, succeeding time steps will change \tilde{B}_r only marginally, thus we can assume $\tilde{B}_r^{(k+1)} \approx \tilde{B}_r^{(k)}$ and write:

$$b_r = \frac{\tilde{B}_r}{B_{\text{crit}}}, \quad (4.10)$$

$$\beta = \frac{B_{\text{crit}} \sigma v_{e\perp 0}}{2J_{\parallel}}, \quad (4.11)$$

$$0 = b_r^2 - 2\beta b_r + 1. \quad (4.12)$$

The quadratic equation has the following solutions:

$$b_r = \beta \left(1 \pm \sqrt{1 - \frac{1}{\beta^2}} \right). \quad (4.13)$$

We have two asymptotic solutions as $\beta \rightarrow \infty$, namely

$$b_r = 2\beta \rightarrow \infty, \quad (4.14)$$

$$b_r = 0. \quad (4.15)$$

These correspond to the initial phase (4.15) and the fully penetrated phase (4.14). At the point $\beta = 1$ we obtain the connection point of the two different branches of the solution. A sketch of the solutions are given in figure 4.2.⁴

⁴To get the behaviour at this point, we can expand the square root into a LAURENT series,

$$\sqrt{1 - \frac{1}{\beta^2}} \approx 1 - \frac{1}{2\beta^2} + \mathcal{O}(\beta^{-3}).$$

Then we get

$$b_r = 2\beta - \frac{1}{2\beta}, \quad b_r = \frac{1}{2\beta},$$

for the feedback phase and the ramp up phase respectively.

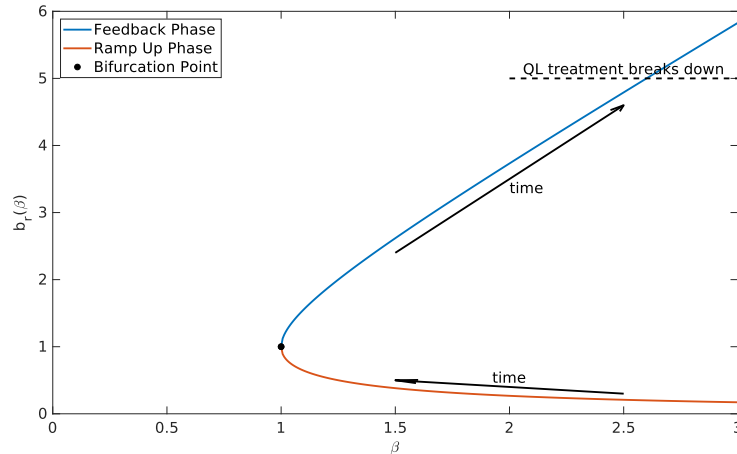


Figure 4.2. Solutions of the quadratic equation (4.13) with arrows indicating the evolution in time by a ramp up of the current in the RMP coils. The bifurcation point is the border between two qualitative different solutions. The limit for the breakdown of the quasilinear treatment has been indicated though its position was set arbitrarily.

4.2 Computational Model

The base for the computational model is previous work in [21] that can be sketched as

1. Calculation of the antenna field.
2. Field line integration and calculation of FOURIER modes for the vector potential \mathbf{A} .
3. Profile preprocessing.
4. Run of the balance code⁵ with MAXWELL solver KiLCA. Calculation of quasilinear diffusion coefficients.
5. Rescaling D_{e22}^{QL} with *form factors* (ratio of antenna field and vacuum field).
6. Comparison of D_{e22}^{QL} with the anomalous diffusion coefficient $D_{e22}^a \approx 10^4 \text{ cm s}^{-1}$.

This thesis introduces some changes to the model. Most important is the rescaling to toroidal geometry which is changed to include effects of mode coupling. So far this is done with the help of the code GPEC [42, 43, 44] which computes perturbed iMHD equilibria in toroidal geometry. Doing so, step 1 of the list above is not necessary anymore, since the information of the RMP coils goes straight into this code. Second, the anomalous coefficient is estimated via consideration of heating power. Third, profiles do not necessarily have to come already preprocessed as it is now possible to fit experimental data on our own using the AUG tool AUGPED. Additionally, the whole computational model has been automated (except for the hand fitting with AUGPED and the run of the code GPEC since both have an external origin). This brings the possibility to make extensive studies on the effects of different profiles, equilibria, parameters, etc..

The whole model is sketched in figure 4.3, the profile preprocessing is quite sophisticated and given in figure 4.4. All parts of the computational model will be successively described in the following subsections.

⁵The name comes from a different nomenclature, where transport equations were referred as balance equations.

Estimation of the Bifurcation Threshold:

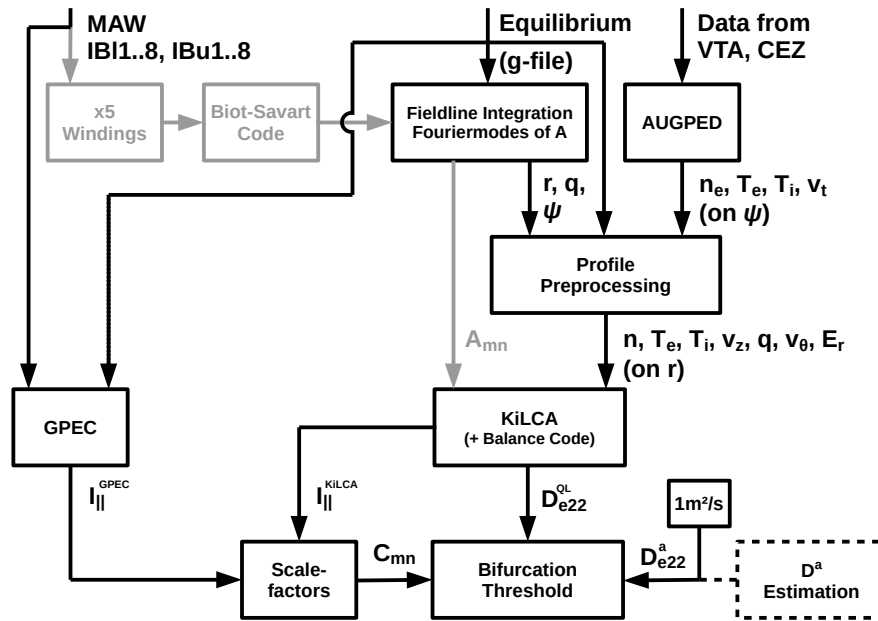


Figure 4.3. Flow chart describing the full computational model for the estimation of the bifurcation threshold. Grey boxes are not necessary anymore but were used in the old model.

Profile Preprocessor:

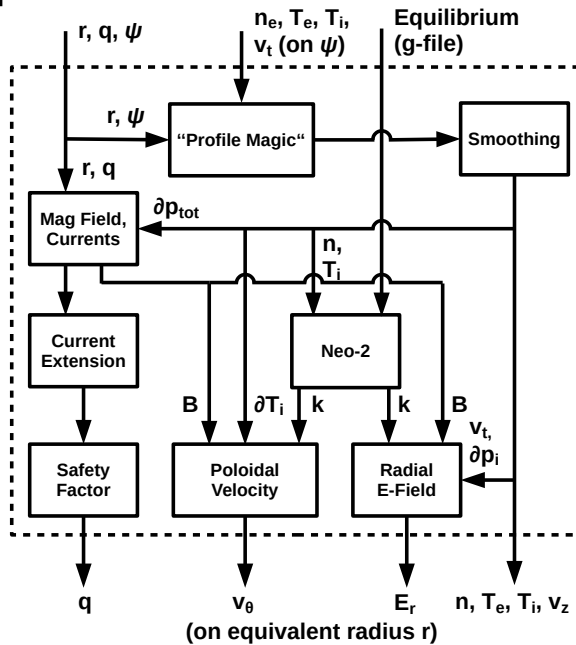


Figure 4.4. Flow chart describing the profile preprocessing routines.

4.2.1 Equilibrium Preprocessing

In this part of our computational model, the equilibrium poloidal flux on an RZ -grid (intermediate cylindrical system in figure 3.1) as well as the major radius and the toroidal magnetic field in the center is read from an “g-file” (computed by a 2D-equilibrium code, e.g. EFIT). The full magnetic field is reconstructed as well as the poloidal and toroidal fluxes. The field lines are integrated to calculate the safety factor q .

This basic information is used to calculate the “effective radius” for our cylindrical model. The definition of the poloidal flux is [26]:

$$\Psi_{\text{tor}} = \iint_S \mathbf{B} \cdot d\mathbf{S}, \quad (4.16)$$

$$\Psi_{\text{tor}} = 2\pi\psi_{\text{tor}}. \quad (4.17)$$

The quantity S is the toroidal cross section area limited by the flux surface. The effective radius is defined as the radius of a circle with area $S = r^2\pi$. In simple terms, we get for the toroidal flux

$$\Psi_{\text{tor}} \approx B_{\text{ref}}S,$$

where B_{ref} is the toroidal field at the magnetic axis. Finally, the definition of the effective radius is:

$$r = \sqrt{\frac{2\psi_{\text{tor}}}{B_{\text{ref}}}}. \quad (4.18)$$

4.2.2 Profile Preprocessing

The experimental profiles our model needs as input are density n_e , electron and ion temperature T_e, T_i as well as toroidal rotation velocity v_t ⁶. Because of quasi-neutrality we can assume $n_i \approx n_e$, thus we need only one density. The electron quantities n_e and T_e are measured with THOMSON scattering diagnostics that have lines of sight in the core and at the edge of the plasma⁷. In this method, laser light is scattered by the plasma resulting in a broadening of the spectrum from which the electron temperature can be obtained. The density is related through the scattered power [6]. The ion quantities T_i and v_t can be measured by charge exchange recombination spectroscopy (CXRS). One uses the fact that neutral beam atoms can exchange their electrons with impurities in the plasma, leaving the latter one in an excited state, measuring the photons emitted afterwards [45].

These diagnostics give single measurements distributed in time which have to be translated into profiles over any flux surface label. This is done with a free-knot-spline fit over the measured data from a time interval symmetric around the time we want to consider. The tool used for this at AUG is called AUGPED. The result are four profiles given on the normalized poloidal flux radius ρ_{pol} , which can be used for further modelling (figure 4.5). The quantity ρ_{pol} is defined by the poloidal flux as

$$\rho_{\text{pol}}^2 = \frac{\Psi_{\text{pol}} - \Psi_a}{\Psi_s - \Psi_a}, \quad (4.19)$$

where Ψ_a is the poloidal flux on the magnetic axis and Ψ_s the poloidal flux on the separatrix. Thus, we call ρ_{pol} the normalized poloidal flux radius and ρ_{pol}^2 the normalized poloidal flux. Both quantities

⁶This quantity is usually given as an angular velocity in rads^{-1} and has to be translated into a usual velocity by $v_z = R_0 v_t$, where R_0 is the big torus radius.

⁷There are other diagnostics for the electron quantities as well but for simplicity only THOMPSON scattering is considered here.

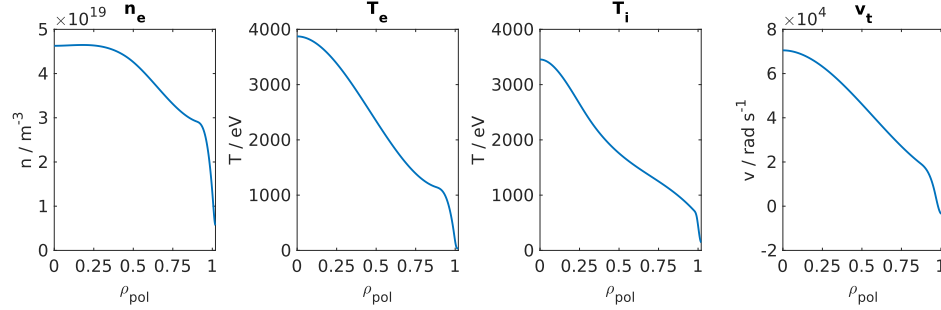


Figure 4.5. Example for raw input profiles given on ρ_{pol} . In this case, data is for AUG shot 33353 at 2325ms.

are 0 at the magnetic axis and 1 at the separatrix. For profile preprocessing we will use ρ_{pol}^2 .

“Profile Magic”: In order to use the profiles in the code KiLCA, they have to be continued outside the separatrix up to the position of the antenna (coil)⁸. This process we call “profile magic”. Figure 4.6 shows an example how “profile magic” is applied on an ion temperature profile. The idea is as follows: inside the separatrix we want to use the initial profile whereas outside we want to set it to a reasonable value. To ensure a smooth transition we can use the function “ExpCut” which is a smoothed step function,

$$\text{ExpCut}(x) = \frac{1}{1 + e^{\frac{x-x_c}{d}}}, \quad (4.20)$$

with parameters x_c , which defines the location where the value of the function is 1/2, and d which gives the characteristic width of the function. By weighting the initial profile with $\text{ExpCut}(x)$ and the end value with $1 - \text{ExpCut}(x)$, we get the desired result. The parameters x_c and d have to be chosen carefully to not modify the profile too strongly.

The whole process of “profile magic” may seem a bit questionable. Our justification is that only the very edge of the profiles is affected. The cylindrical approximation used by KiLCA approaches its end of validity at the edge anyways, so we only have to consider results for modes which are sufficiently far away from the edge.⁹

Safety Factor Profile Extension: The next profile KiLCA needs as an input is the safety factor q . The general behaviour of q is that it diverges at the separatrix which makes it hard to continue outside. Therefore, this has to be done in a more sophisticated way that includes the calculation of the magnetic field. Thus, we start with the radial force balance in cylindrical coordinates (3.7),

$$4\pi\partial_r p = -\frac{B_\theta^2}{r} - \frac{1}{2}\partial_r B^2, \quad (4.21)$$

where the first term describes magnetic stress and the second one magnetic pressure. With the expression for the safety factor (3.3),

$$q = \frac{rB_z}{RB_\theta},$$

we can write the absolute magnetic field as

⁸Because the antenna is already outside the separatrix it is better to do this in our effective radius variable defined by (4.18).

⁹In most cases this means that (m, n) modes (9, 2) and (10, 2) are not considered and the effect of mode (8, 2) may be questioned.

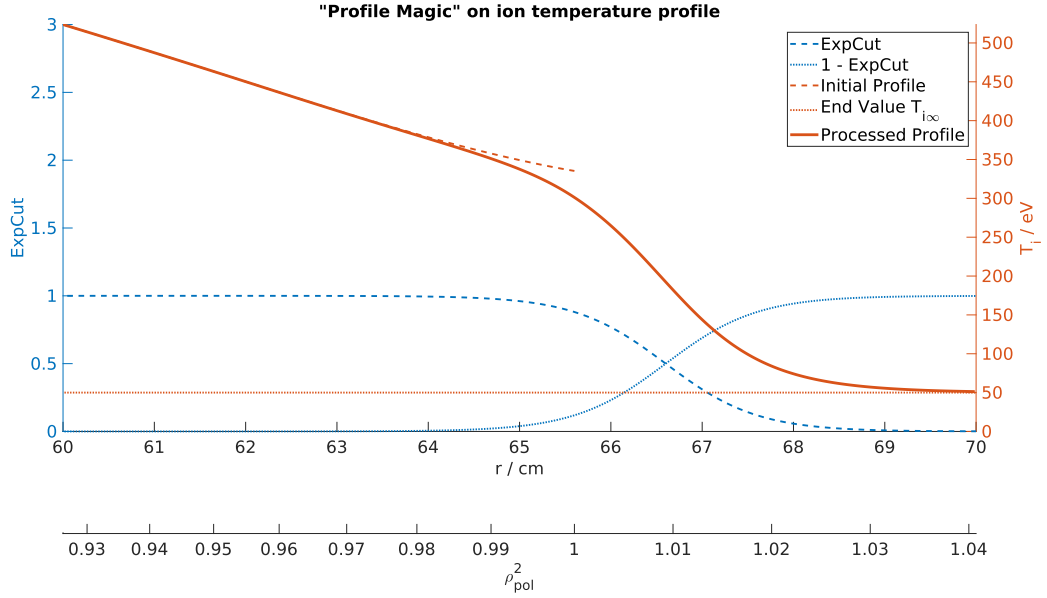


Figure 4.6. Example on the application of “profile magic” on an ion temperature profile. The initial profile is given up to $\rho_{\text{pol}}^2 = 1$ ($r \approx 65.6$ cm, separatrix) and has to be continued up to the position of the antenna ($r_a = 70$ cm). Normalized poloidal flux > 1 in this figure is calculated by linear extrapolation from the inside of the separatrix up to the antenna.

$$\begin{aligned} B^2 &= B_\theta^2 + B_z^2, \\ &= B_\theta^2 \left[1 + \left(\frac{Rq}{r} \right)^2 \right]. \end{aligned} \quad (4.22)$$

Now we rewrite the term representing magnetic stress in (4.21),

$$\frac{B_\theta^2}{r} = \frac{B^2}{r \left[1 + \left(\frac{Rq}{r} \right)^2 \right]} = \frac{rB^2}{R^2q^2 \left[1 + \left(\frac{r}{Rq} \right)^2 \right]} = \frac{rB^2}{R^2q^2g},$$

where we introduce an abbreviation for the last brackets,

$$g = 1 + \left(\frac{r}{Rq} \right)^2. \quad (4.23)$$

Re-inserted into (4.21) we obtain the following ODE for the absolute square of the magnetic field:

$$\partial_r B^2 + \frac{2r}{R^2q^2g} B^2 = 8\pi \partial_r p. \quad (4.24)$$

Equation (4.24) is solved with a RUNGE-KUTTA 113 solver, giving B^2 and further B_θ^2 through (4.22). B_z is then obtained using the safety factor.

After the magnetic field has been calculated, the currents are obtained via AMPÉRES law (3.6). Now “profile magic” is again applied. Our physical arguments are that outside the separatrix there is almost vacuum and we can assume the currents to go to zero (vacuum \rightarrow no particles \rightarrow no currents). Thus,

we extend the currents continuously to zero up to the position of the antenna, integrate them to get the magnetic field, and further calculate the new safety factor. The result contains a “smooth kink”¹⁰ in q as one can see in figure 4.7.

Poloidal Velocity & Radial Electric Field: These quantities complete the set of input profiles for KiLCA and are taken from neoclassical theory [21, 41]¹¹:

$$V^\theta = \frac{ckB_\varphi}{e\sqrt{g}B^2} \frac{dT_i}{dr}, \quad (4.25)$$

$$E_r = \frac{1}{en} \frac{dp_i}{dr} + \frac{\sqrt{g}B^\theta}{c} (V^\varphi - qV^\theta). \quad (4.26)$$

The quantity k is a neoclassical coefficient that links the poloidal flow with the ion temperature gradient¹² which is calculated for each shot and time with the code NEO-2 [41, 46, 47]. These formulas are for general geometry and contain the covariant component of the toroidal field B_φ , the contravariant component of the poloidal field B^θ and both flow velocities V^φ, V^θ as well as the metric determinant \sqrt{g} . We have to apply them to our large aspect ratio system defined in section 3.1 where $\hat{B}_\varphi \approx B_z$. The metric tensor is diagonal with components

$$g^{rr} = 1, \quad g^{\theta\theta} = r^2, \quad g^{\varphi\varphi} = R^2, \quad g = r^2 R^2. \quad (4.27)$$

Thus, we get the physical components as

$$\begin{aligned} B_\varphi &= R\hat{B}_\varphi \approx R\hat{B}_z, & B^\theta &= \frac{B^\varphi}{q} \approx \frac{1}{qR}\hat{B}_z, \\ V^\varphi &= \frac{1}{R}\hat{V}_\varphi \approx \frac{1}{R}\hat{V}_z, & V^\theta &= \frac{1}{r}\hat{V}_\theta. \end{aligned}$$

By insertion into (4.25), we get the poloidal flow velocity:

$$\hat{V}_\theta = \frac{ck\hat{B}_z}{eB^2} \frac{dT_i}{dr}. \quad (4.28)$$

$$\approx \frac{ck}{eB} \frac{dT_i}{dr}. \quad (4.29)$$

In the second line one can make an approximation that the magnetic field is dominated by the toroidal component $\hat{B}_z \approx B$. The next step is to rewrite the electrical field. The last two terms in (4.26) are

$$\begin{aligned} \frac{\sqrt{g}B^\theta}{c} (V^\varphi - qV^\theta) &= \frac{r\hat{B}_z}{qc} \left(\frac{1}{R}\hat{V}_z - \frac{q}{r}\hat{V}_\theta \right), \\ &= \frac{r\hat{B}_z\hat{V}_z}{Rqc} - \frac{\hat{B}_z\hat{V}_\theta}{c}. \end{aligned}$$

This can be inserted back into (4.26) to obtain an expression for E_r (and an approximation for $\hat{B}_z \approx B$):

¹⁰The possible effects of this kink are coming from the current that is needed to produce it. For real safety factor profiles up to the separatrix ($q \rightarrow \infty$) the current needed to sustain such a q -profile in cylindrical geometry would be infinite too. This means that the electron flow velocity becomes larger than the thermal velocity which would lead to many unphysical features. Therefore one has to “saturate” the growth of q near the separatrix. Therefore, q in KiLCA is different to the one in reality.

¹¹To avoid mistakes in calculations we write c (speed of light) again.

¹²We take ion quantities because our measured toroidal rotation v_t is given for ions.

$$E_r = \frac{1}{en} \frac{dp_i}{dr} - \frac{k\hat{B}_z^2}{eB^2} \frac{dT_i}{dr} + \frac{r\hat{B}_z\hat{V}_z}{R_0cq}, \quad (4.30)$$

$$\approx \frac{1}{en} \frac{dp_i}{dr} - \frac{k}{e} \frac{dT_i}{dr} + \frac{rB\hat{V}_z}{R_0cq}. \quad (4.31)$$

After this exercise in coordinate transformations, we again only use physical coordinates and omit the hat on all quantities. Additionally we switch back to our notation,

$$v_\theta \equiv \hat{V}_\theta, \quad v_z \equiv \hat{V}_z. \quad (4.32)$$

Examples for both, v_θ and E_r profiles can be seen in figure 4.7.

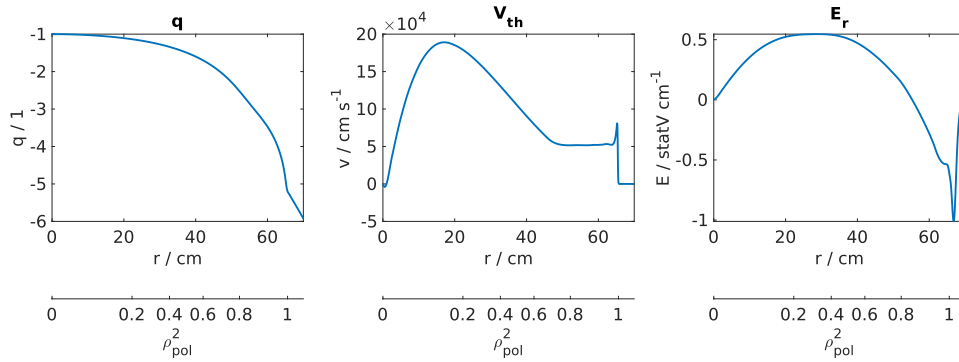


Figure 4.7. Calculated profiles of safety factor q , poloidal velocity v_θ and radial electric field E_r for AUG shot 33353 at 2325ms.

4.2.3 Accounting for Effects of Toroidal Geometry

Our straight cylinder model completely neglects effects of toroidal geometry, especially the coupling of toroidal modes which can change amplitudes of resonant magnetic fields and thus the quasilinear diffusion coefficients. To account for these factors, the previous model in [21] used so-called *spectral factors*¹³ W_{mn} for rescaling of the diffusion coefficients,

$$D_{e22}^{\text{tor}} = D_{e22}^{\text{cyl}} |W_{mn}|^2, \quad (4.33)$$

$$W_{mn} = \frac{A_{\theta,mn}^{\text{realistic}}}{A_{\theta,mn}^{\text{vac}}}, \quad (4.34)$$

$$A_{\theta,mn}^{\text{vac}} = \frac{rR_0}{n} B_r^{\text{vac}}. \quad (4.35)$$

The index mn indicates that each quantity is separately computed for each mode number. The perturbed poloidal vector potential for vacuum is calculated from the radial magnetic field in vacuum (KiLCA) whereas the realistic one was taken from the FOURIER decomposition of the vacuum field of the RMP coil¹⁴.

In the new improved model we introduce rescaling coefficients C_{mn} to account for mode coupling in toroidal geometry. We do this by taking parallel currents in cylindrical geometry and divide them

¹³These are the absolute squared of the earlier mentioned *form factors* (3.52).

¹⁴This was done over the angles of symmetry flux coordinates associated with the realistic unperturbed equilibrium field.

by parallel currents from an iMHD code in toroidal geometry. Because iMHD cannot handle singular currents (chapter 2), these currents are usually added externally in the equations to achieve ideal shielding.

We take the former from KiLCA and the latter ones from the code GPEC [42, 43, 44]. The new rescaling of the diffusion coefficients is then:

$$D_{e22}^{\text{tor}} = D_{e22}^{\text{cyl}} |C_{mn}|^2, \quad (4.36)$$

$$C_{mn} = \frac{I_{\parallel,mn}^{\text{GPEC}}}{I_{\parallel,mn}^{\text{KiLCA}}}. \quad (4.37)$$

The scaling is chosen according to (4.37), because due to linear theory we have $\tilde{B}_r \sim I_{\parallel}$ and due to quasilinear theory $\tilde{B}_r^2 \sim D_{e22}^{\text{QL}}$. Together we then have the influence of I_{\parallel}^2 in the diffusion coefficients. With (4.36) we scale out the factor of the parallel currents by KiLCA and weight the amplitudes for the different modes by the parallel currents of GPEC¹⁵.

Calculation of the total resonant parallel current within KiLCA: Since in KiLCA the geometry is given by nested cylinders, all we have to do is to integrate the parallel current over an annulus centered at the location of the resonant surface $r_{s,mn}$ (defined by (3.4)):

$$I_{\parallel,mn}^{\text{KiLCA}} = 2\pi \int_{r_{s,mn}-d_{mn}}^{r_{s,mn}+d_{mn}} r J_{\parallel,mn}(r) dr. \quad (4.38)$$

The quantity d_{mn} is the resonant layer width which has to be estimated. This is done by doing a nonlinear fit with a gaussian centered around $r_{s,mn}$ and taking five times the standard deviation σ_s (figure 4.8),

$$d_{mn} \approx 5\sigma_s. \quad (4.39)$$

This works well because the parallel current is quite small throughout the whole plasma, whereas near resonant surfaces it gets locally concentrated (sheet current). The only limitation on this is at the very edge where the resonant current may overlap with the current in the antenna. This is not really a problem since our model is in trouble anyways at these locations.

4.2.4 Estimation of the Anomalous Diffusion Coefficient

By now the bifurcation criterion was always estimated by using the “universal constant” $D_{e22}^a \approx 10^4 \text{ cm s}^{-1}$ for the anomalous diffusion coefficient. To make this more realistic we introduce an estimation based on heat fluxes in the plasma.

The plasma is heated with NBI and electron/ion cyclotron resonance heating E/ICRH (on AUG only NBI + ECRH). The input power in the plasma is then the difference between the total heating power and the power lost by radiation:

$$P_{\text{inp}} = P_{\text{heat}} - P_{\text{rad}}. \quad (4.40)$$

The total heat flux in the plasma is then given by the power going through a flux surface,

¹⁵This assumes, that the coefficients linking \tilde{B}_r with I_{\parallel} and D_{e22}^{QL} stay almost the same in cylindrical as well as toroidal geometry.

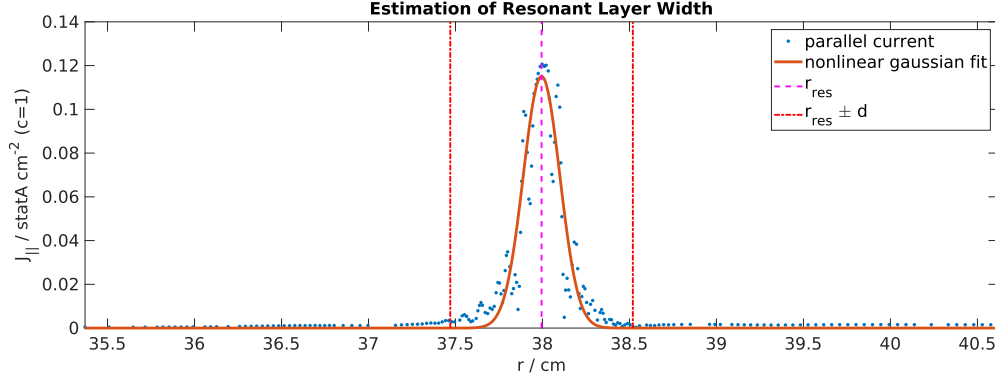


Figure 4.8. Estimation of resonant layer width by fitting a Gaussian through the parallel current. The figure is just a sketch and does not belong to a real experimental shot.

$$Q_e = \frac{P_{\text{inp}}}{S}, \quad (4.41)$$

where the flux surface can be either roughly estimated by concentric tori with circular cross sections,

$$S \approx 4\pi^2 R_0 r, \quad (4.42)$$

or calculated from the flux tube volume¹⁶,

$$S = \frac{dV}{dr}. \quad (4.43)$$

Now we assume the heat flux comes from diffusion done by electrons (4.4),

$$Q_e \approx -n D_{e22}^a \frac{dT_e}{dr}, \quad (4.44)$$

where D_a is the anomalous diffusion coefficient we are searching for. Consequently we get our final estimation by distributing the input power to electrons and ions evenly:

$$D_{e22}^a \approx -\frac{P_{e,\text{inp}}}{Sn \frac{dT_e}{dr}}, \quad (4.45)$$

$$P_{e,\text{inp}} \approx \frac{1}{2} (P_{\text{heat}} - P_{\text{rad}}). \quad (4.46)$$

An example can be seen in figure 4.9. This model is still not perfect as it completely neglects convective heat transport and distributes the heat evenly to ions and electrons.

¹⁶This is calculated in our field line integration method described above (section 4.2.1).

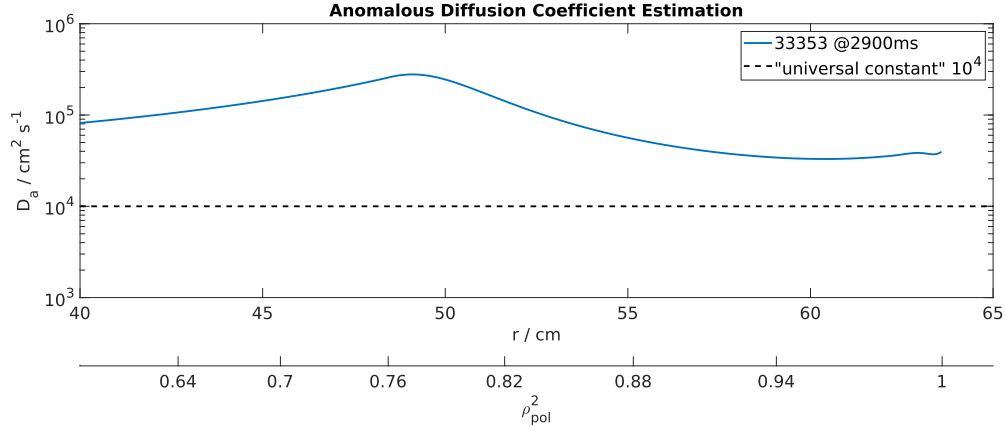


Figure 4.9. Example for the estimation of the anomalous diffusion coefficient for AUG shot 33353 at 2900ms. The new estimation is always higher than the previously used “universal constant” of $10^4 \text{ cm}^2 \text{ s}^{-1}$.

4.3 Application on AUG Shots

Here we will apply the model described in the previous sections to some selected AUG shots. In particular we will use shot 33120 which investigated ELM mitigation at low collisionality and shot 33353 which was used for the optimisation of ELM suppression. The corresponding time traces for the divertor current, D_α -radiation and coil currents can be seen in figure 4.10 and 4.11. For both shots we select two different time slices which have qualitative different behaviour. For shot 33120, 5500 ms is *ELM suppression* and 5635 ms is *ELMy* (bifurcation back to unreconnected state). For shot 33353, 2325 ms is *ELM mitigation* and 2900 ms is *ELM suppression* (bifurcation forward to reconnected state)¹⁷.

The data for these time slices was gathered as follows: Equilibria were of type EQH, which is automatically computed by the code CLISTE at AUG. Coil currents come from the MAW diagnostics and were used in GPEC. Profiles were handfitted with free-knot-spline fits by us using the tool AUPED at AUG. Raw data came from CXRS for T_i and v_t ¹⁸, and from core and edge THOMPSON scattering for T_e and n_e . The preprocessed profiles we used for all four time slices can be seen in figures 4.12-4.15. All computations in this thesis have been done for toroidal mode number $n = 2$ which dominates the coil spectrum in all AUG shots considered here.

4.3.1 Investigation of Bifurcation Thresholds

The main results of the application of our model on the specified AUG shots can be seen in figure 4.16 and 4.17. Time slices where we see suppression in the time traces, are linked with a bifurcation on mode $m = 6$ which is roughly on top of the pedestal of the total pressure profile. Modes in the core ($m = 4, 5$) seem to have only little effect, whereas modes at the edge ($m = 7, 8$) are always below the threshold¹⁹. For the ELMy case (shot 33120, 5635 ms), all modes are below the threshold for bifurcation whereas for the ELM mitigation case (shot 33353, 2325 ms), only mode $m = 5$ is in a bifurcated state.

¹⁷The labelling of the time slices was done according to comments of W. Suttrop

¹⁸CXR Box Spectroscopy NI Box 1 and Toroidal edge CXRS.

¹⁹Mode $m = 9$ as well, but we do not trust this mode because it is too close to the edge. Already mode $m = 8$ may be questioned.

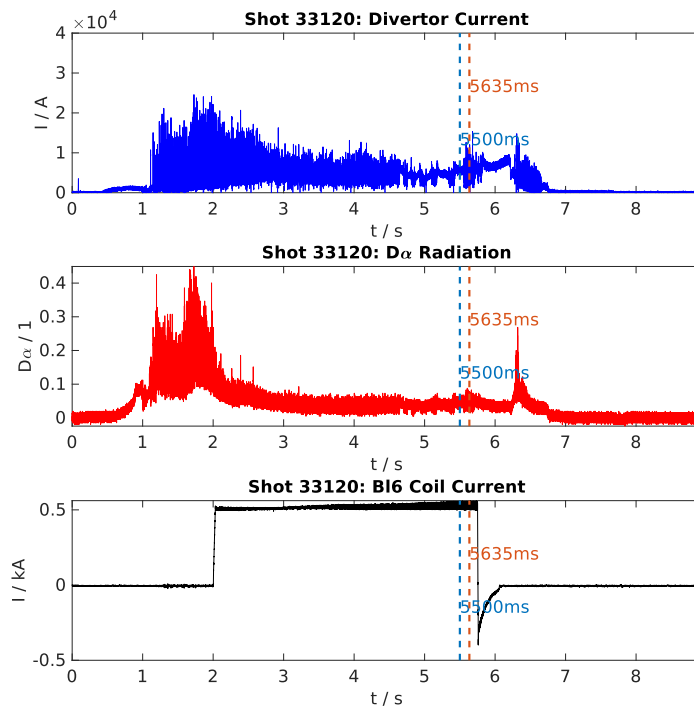


Figure 4.10. Divertor current, D_α radiation and the coil current for the BI6 coil for AUG shot 33120. Dashed lines show the time slices considered.

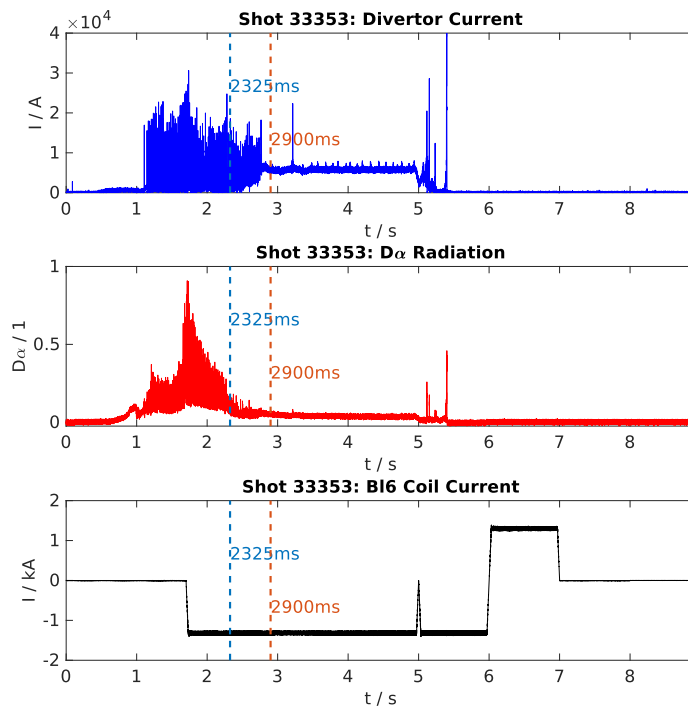


Figure 4.11. Divertor current, D_α radiation and the coil current for the BI6 coil for AUG shot 33353. Dashed lines show the time slices considered.

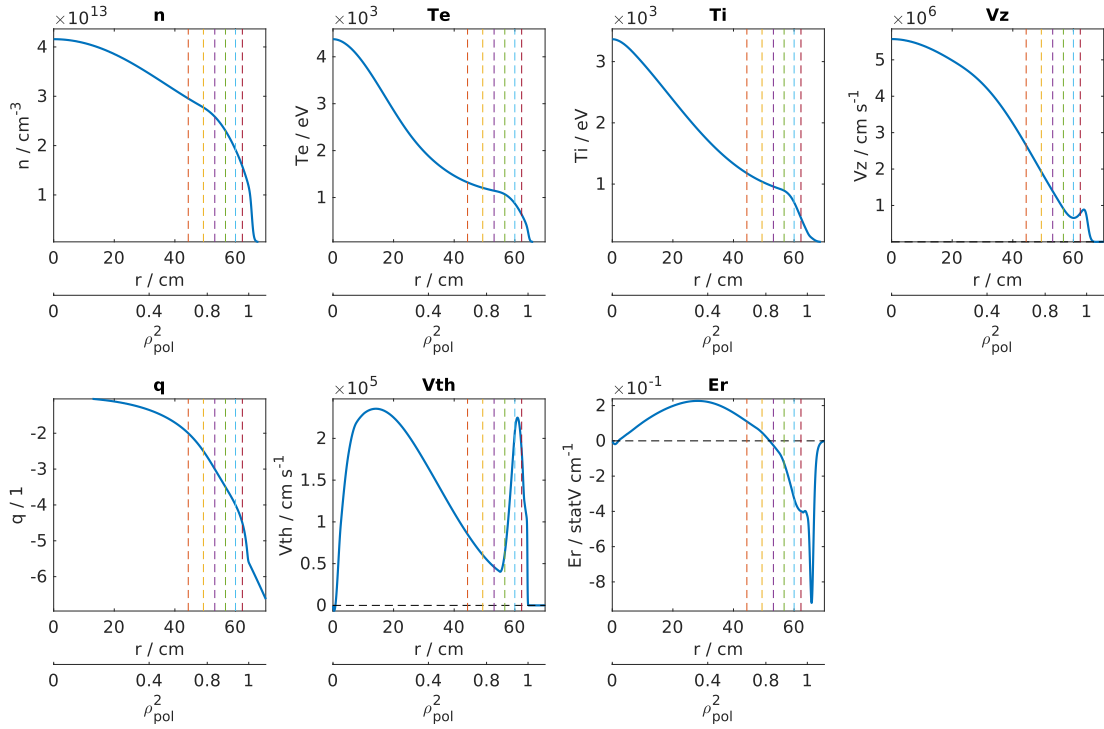


Figure 4.12. Profiles used for shot 33120 at time 5500 ms. Colored lines correspond to the location of resonances for modes $m = 4, 5, 6, 7, 8, 9$.

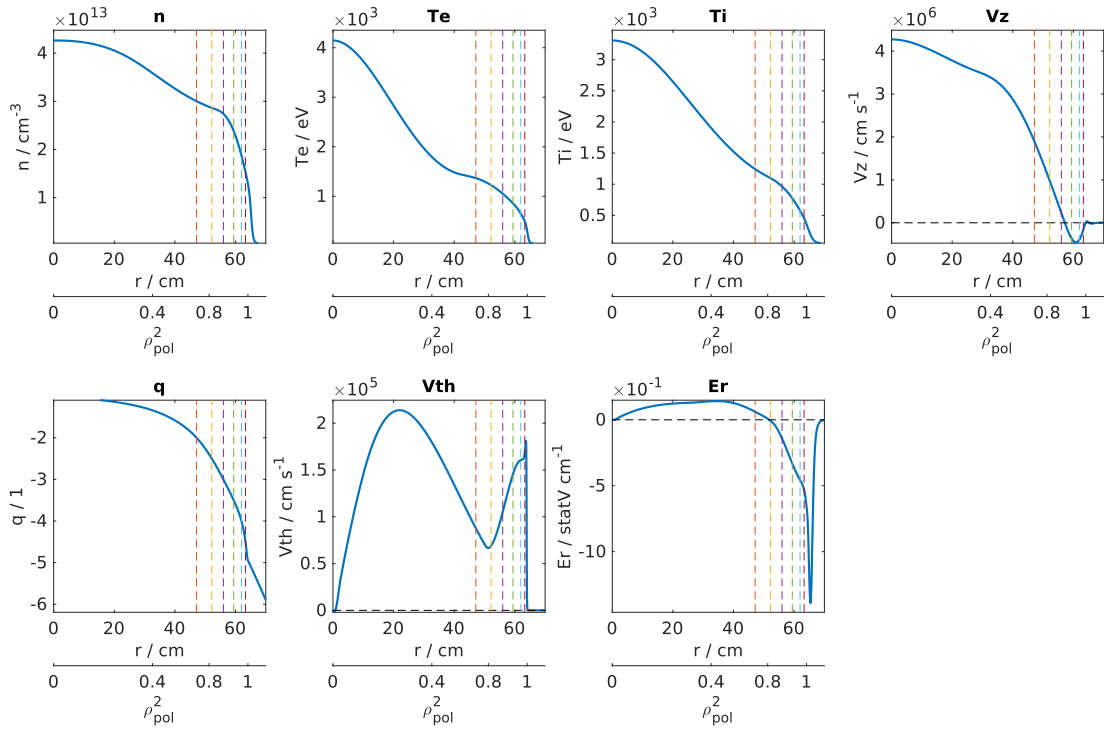


Figure 4.13. Profiles used for shot 33120 at time 5635 ms.

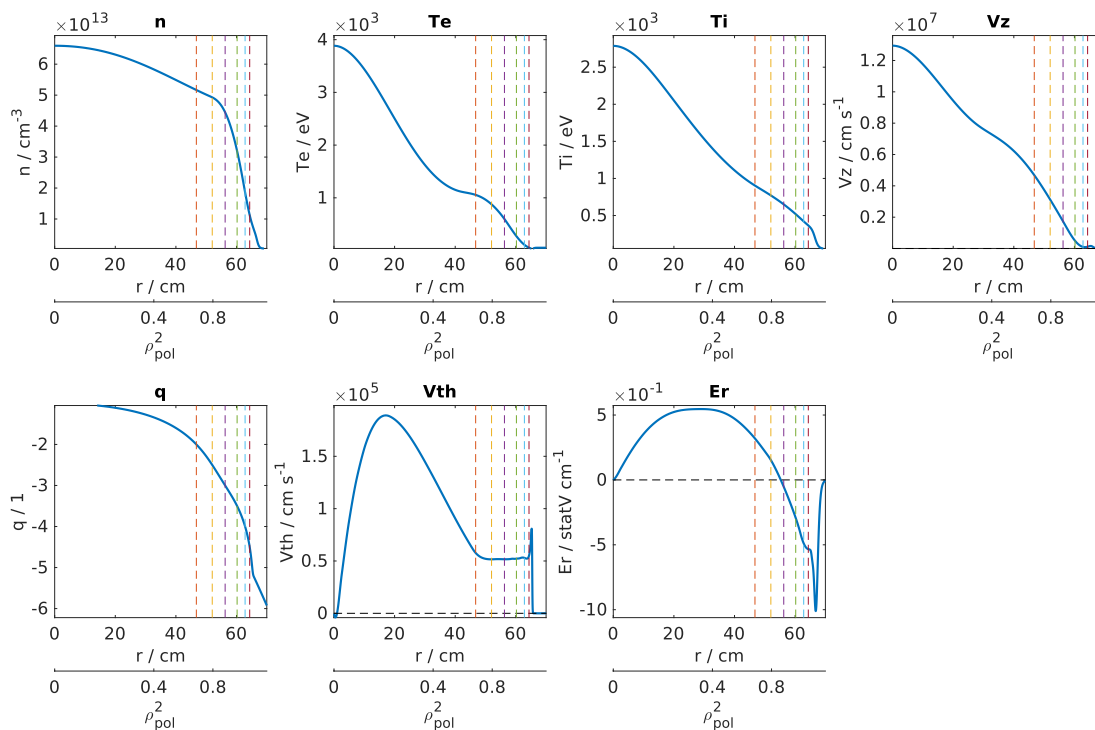


Figure 4.14. Profiles used for shot 33353 at time 2325 ms.

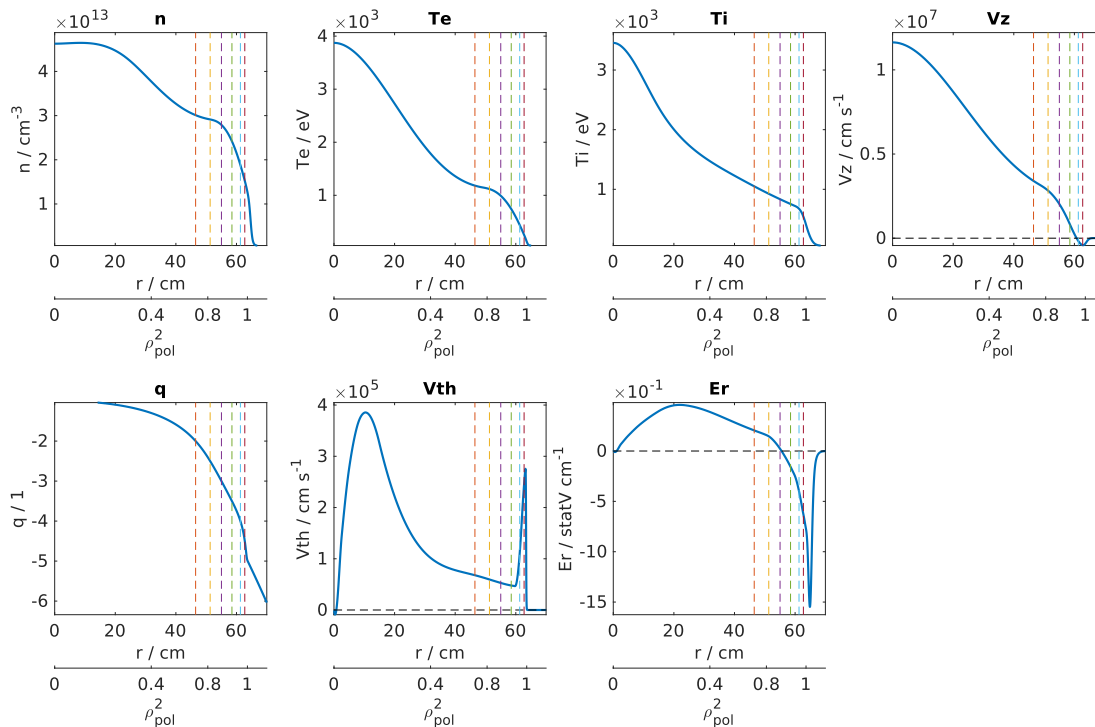


Figure 4.15. Profiles used for shot 33353 at time 2900 ms.

This could indicate a difference between ELM suppression, ELM mitigation and ELMy: In the first case, we have a bifurcated mode at the pedestal top, in the second one the bifurcated mode is further away from the pedestal top but still in its vicinity and finally for the third one, no mode is bifurcated.

Furthermore, if one looks carefully at the profiles (figures 4.12-4.15) one can see a link between the location of the zero of the electric field ($v_{E \times B}$ resonance) and the bifurcation of mode $m = 6$. At time slices where ELM suppression is observed, the electric field has its zero very close to the purple line ($m = 6$ resonance). This may indicate that the $v_{E \times B}$ resonance is more important than the fluid resonance in these experiments.

Regarding the rescaling of the quasilinear diffusion coefficients, these computations have also been done without the account of mode coupling. Generally, the cylindrical model overestimates the effect of modes at the edge by a factor of 10 – 100, whereas for modes in the core there are only slight corrections. The usage of an estimated anomalous diffusion coefficient makes it harder for modes to reach the bifurcation threshold in our model but still we see that the threshold can be exceeded.

4.3.2 Effect of Different Profiles

In the implementation of the whole model it became very clear that the exact form of the input profiles have a great impact on the overall outcome. To investigate this further, we decided to qualitatively study the effect of a change in the input profiles for one particular shot and time. Therefore we took the input profiles from a run with the old model (*reference*) and compared them with the profiles used in this thesis for AUG shot 33353 at time 2900 ms (*new*, figure 4.15). The equilibrium was taken the same and in the preprocessing we did exactly the same for both sets of profiles. The difference between the two sets of input profiles can be seen in figure 4.18. We then chose to exchange all profiles individually as well as a combination of the profiles from THOMPSON scattering (T_e, n) and from CXRS (T_i, v_t). This gives a total of eight different runs, which results can be seen in figure 4.19.

First we can discuss the differences in the two sets of profiles. In general we have very similar profiles for the temperatures and the density. The toroidal velocity in contrast is similar at the edge but approaches a value about twice as high as in the new case. Additionally, both temperature profiles from the reference run have unphysical behaviour at the magnetic axis. By using these profiles one usually assumes poloidal symmetry along each direction in the tokamak which does not allow for a kink in the center. Apart from these differences, there are many local differences at the positions of the resonance, especially different gradients in all quantities. Out of this alone, one can expect strong dependencies of the quasilinear diffusion coefficients on the exact form of the profile.

By looking at the result one can indeed see great differences from the toroidal velocity profiles, especially for modes which are further inside the plasma where the difference in v_t is larger. This has been investigated, and we found out that the change in toroidal velocity profile incidentally shifted the location of the fluid resonance very close to mode $m = 6$. This fits with the enormous increase of the quasilinear diffusion coefficient for this mode. The other profiles have little impact on modes $m = 4, 5$ further inside and on mode $m = 8$ at the very edge (remember: we do not trust mode $m = 9$). The biggest impact can be seen for modes $m = 6, 7$ which are of particular interest for the bifurcation threshold as already mentioned.

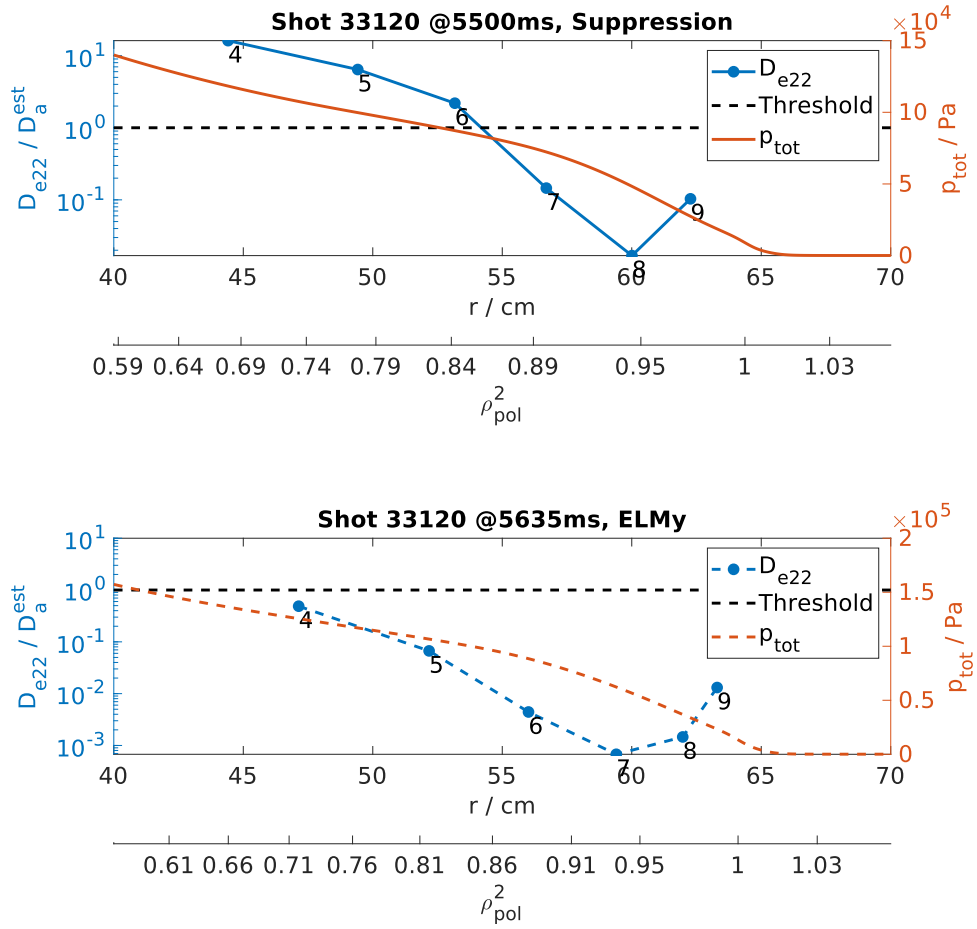


Figure 4.16. Resonant diffusion coefficients D_{e22} ($\equiv D_{e22, mn}^{\text{QL}}$) weighted with the corresponding estimated anomalous diffusion coefficients D_a^{est} ($\equiv D_{e22, mn}^{\text{a}}$) (left y-axis) together with the bifurcation threshold (dashed line). The total pressure profile is given on the right y-axis to show where modes are located relative to the pedestal. Each subplot corresponds to AUG shot 33120 but is given on a different time slice. A comment on the type of the shot is given in the title.

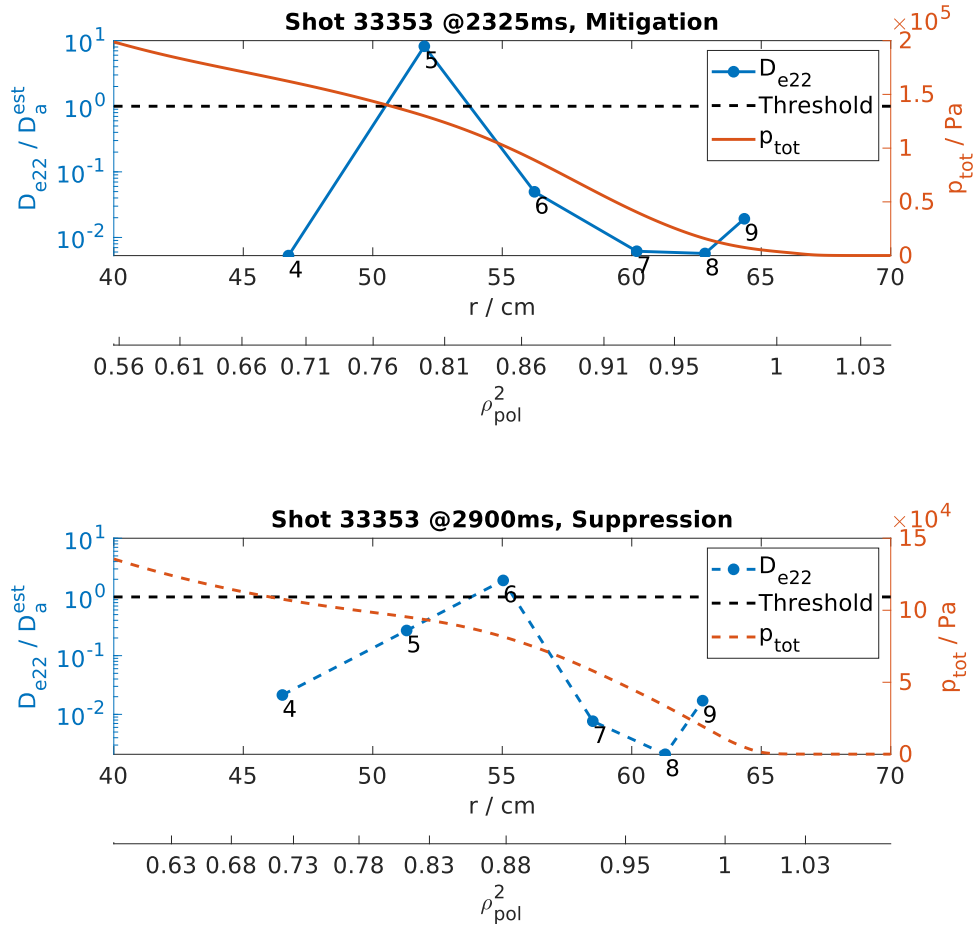


Figure 4.17. Resonant diffusion coefficients D_{e22} ($\equiv D_{e22, mn}^{\text{QL}}$) weighted with the corresponding estimated anomalous diffusion coefficients D_a^{est} ($\equiv D_{e22, mn}^a$) (left y-axis) together with the bifurcation threshold (dashed line). The total pressure profile is given on the right y-axis to show where modes are located relative to the pedestal. Each subplot corresponds to AUG shot 33353 but is given on a different time slice. A comment on the type of the shot is given in the title.

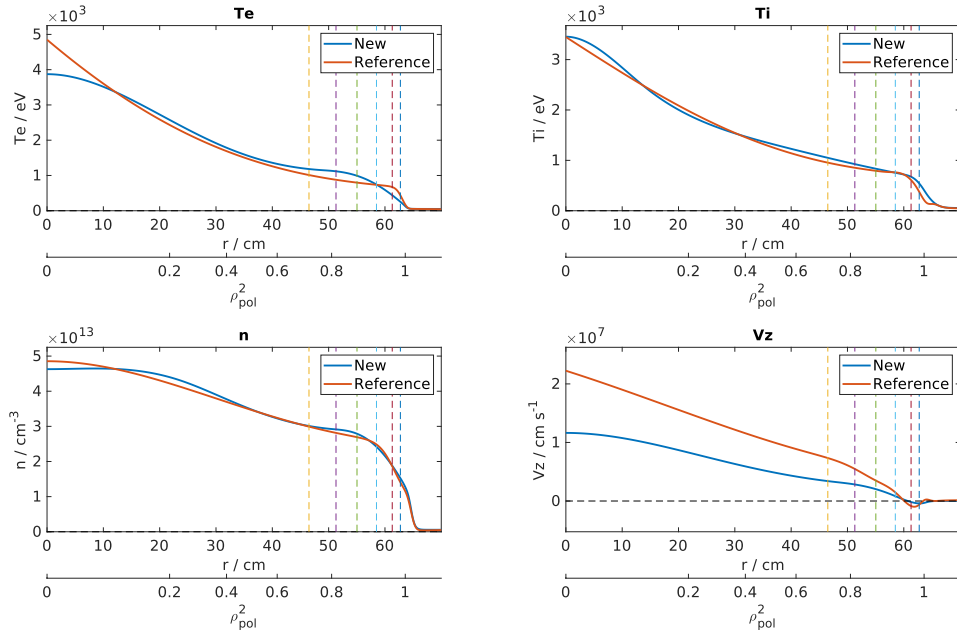


Figure 4.18. Comparison of both sets of preprocessed input profiles from experiment for AUG shot 33353 at time 2900 ms.

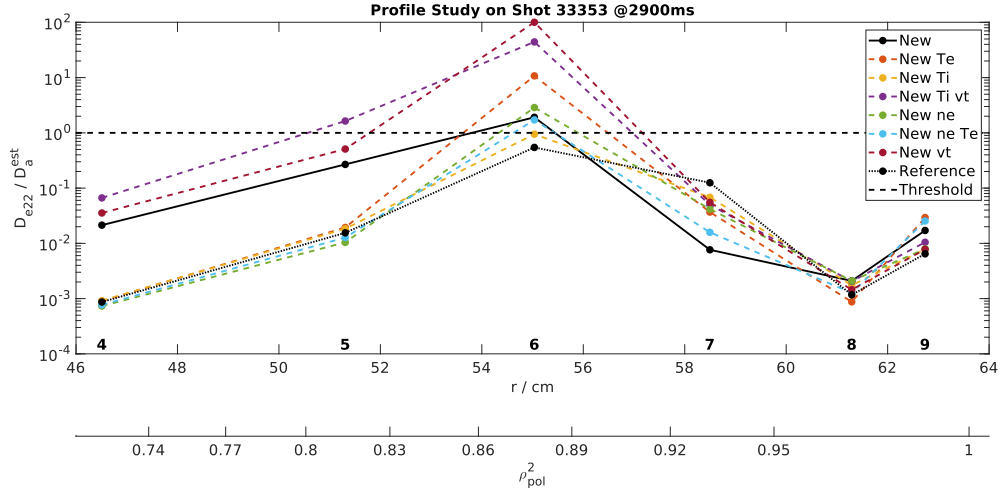


Figure 4.19. Ratio of quasilinear diffusion coefficient D_{e22} ($\equiv D_{e22, mn}^{QL}$) and D_a^{est} ($\equiv D_{e22, mn}^a$) for different combinations of the input profiles from figure 4.18 (AUG shot 33353 at time 2900 ms). The total difference between the set of profiles is given by both black lines.

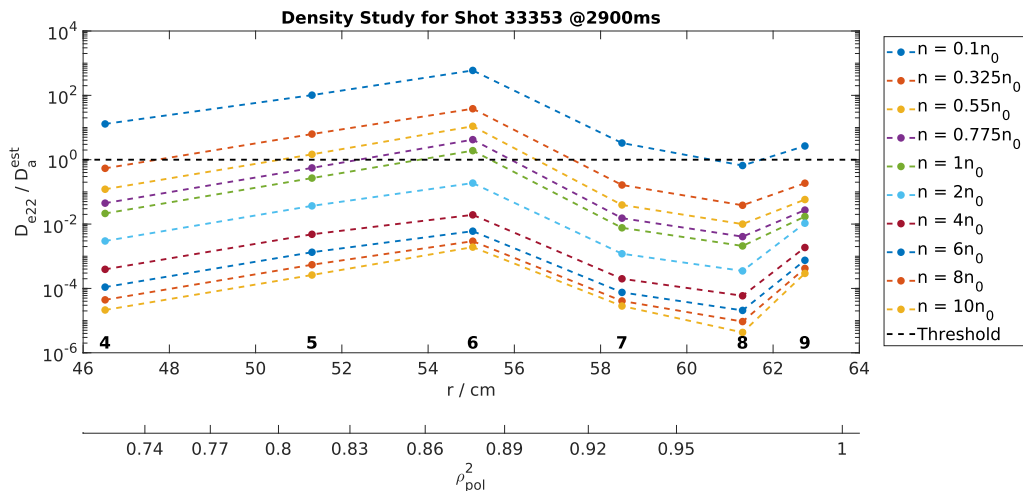


Figure 4.20. Calculation for AUG shot 33353 at time 2900 ms with different densities. Plotted is the ratio of D_{e22} ($\equiv D_{e22, mn}^{QL}$) and D_a^{est} ($\equiv D_{e22, mn}^a$). Density variation was made by scaling the initial density by the factor indicated in the legend. Colors reappear for the different runs but the order is strictly monotonically decreasing from top to bottom with higher density.

4.3.3 Density Scaling

One particular behaviour of interest is the dependence of the bifurcation threshold on density. We study this by a qualitative calculation: We only scale the density after postprocessing by a certain factor and do recomputations of the quasilinear diffusion coefficients. The dependence on the fluid resonances is not affected as the density appears in both, numerator and denominator of the diamagnetic velocity (1.12) and thus scales out.

The result can be seen in figure 4.20. Based on this plot, one can clearly see a threshold in density for the bifurcation of mode $m = 6$ to occur. This will be further discussed in the next section.

4.3.4 Combined Density and Electron Temperature Scaling

Based on the crude calculation in the previous section (and inspired by fig. 15 in [14]), we did these calculations again but with a scan over density and electron temperature²⁰ combined. We calculated the pedestal density and electron temperature by simply taking these values from the profiles where the total pressure profile has a minimum near the pedestal. The results for the most interesting mode ($m = 6$) can be seen in figure 4.21.

One can clearly see that the density threshold for the bifurcation still exists. Additionally, there are effects of the electron temperature which would let us expect to still find ELM suppression at high pedestal densities with very low pedestal electron temperatures and vice versa. Further, empirical limits for the pedestal density and electron temperature from [14] are shown. The density limit is represented very well by this qualitative calculation whereas the temperature limit is far off. This

²⁰The effect of temperature on the bifurcation is more peculiar as for the density and cannot be described as easily.

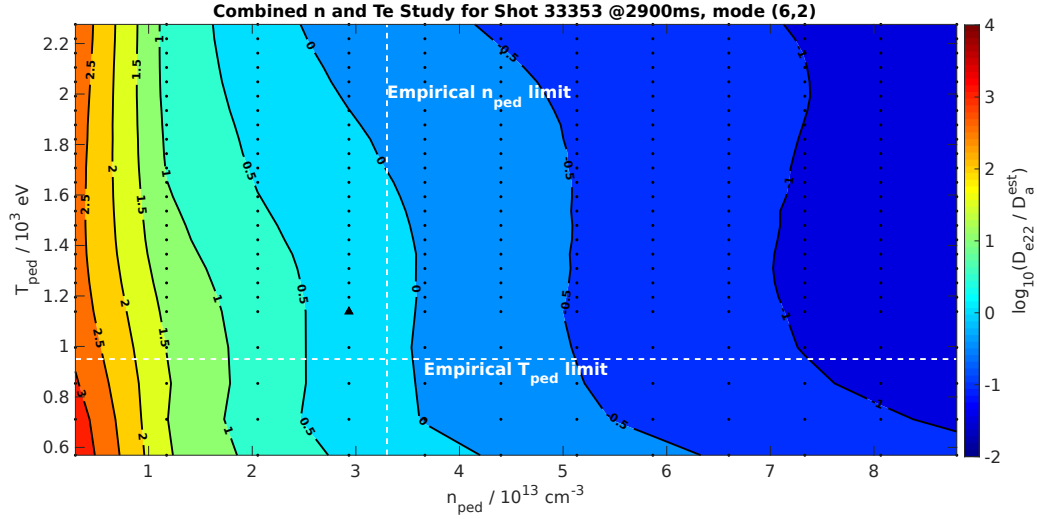


Figure 4.21. Calculation for AUG shot 33353 at time 2900 ms for different pedestal densities and electron temperatures. The triangle (▲) indicates the original runs, small black dots (•) show the calculated points. Based on this, contour lines were calculated by 2D interpolation. The line “0” shows the threshold for bifurcation. In white, empirical pedestal density and electron temperature limits from [14] have been included as dashed lines. The notation in the plot slightly differs from the text by: D_{e22} ($\equiv D_{e22, mn}^{QL}$) and D_a^{est} ($\equiv D_{e22, mn}^a$).

can be seen especially when looking at the initial point of ELM suppression which is outside of the empirical limits. However, this has a very simple explanation. In [14], also profiles were shown and one can see that the electron temperature used there is smaller by around 0.2 keV which would shift the initial point back inside the empirical bounds but furthermore would completely change the temperature scaling of figure 4.21 as the scale is based on this value.

Chapter 5

Conclusion

5.1 Summary

One of the main goals of this thesis was to present an overview of the theory of the interaction of RMPs with plasma. This has been done by starting with the effect of an internal formation of a current sheet that results in the breakdown of the iMHD equations at the inner layer, the location of the sheet current. The inclusion of resistivity in this inner layer “heals” the problem but introduces a finite growth rate for the so-called tearing instability that leads to the formation of magnetic islands.

Further, the large aspect ratio limit for a tokamak was presented and the same theory was applied to this cylindrical system. In contrast to tearing mode theory, external magnetic perturbations produced by an antenna outside the plasma were included (instead of an internal current sheet). This external perturbations in vacuum produce resonances at positions where the safety factor has a rational value given by the ratio of the integer toroidal and poloidal mode numbers. These resonant layers were not treated with a resistive model but with a more advanced kinetic treatment with the code KiLCA. The application of KiLCA resulted in a plasma response that suppressed the growth of magnetic islands at the resonant layers, the external perturbation was shielded by the plasma.

Finally, the quasilinear kinetic estimation of the bifurcation threshold was introduced. The bifurcation of a resonant mode from the shielded state to an unshielded state was qualitatively explained and the effect of resonances was emphasized. A bifurcation criterion based on the ratio of the quasilinear electron heat diffusion coefficient and the corresponding anomalous diffusion coefficient was established. The former model of [21] was discussed and the novelty of this work was presented. This includes the accounting for poloidal mode coupling and a better estimation of the anomalous diffusion coefficient. Finally, applications on experimental AUG shots were made.

5.2 Discussion and Further Suggestions

The application of the new quasilinear kinetic model in cylindrical geometry with accounting of mode coupling indicates that ELM suppression can be linked to bifurcated modes only on top of the pedestal. For further confidence, more experimental shots have to be processed. Nevertheless, it became a bit more unlikely that other modes (especially inside the pedestal) may be important. Recent work of HU, et al. [48], used a similar approach but with a nonlinear resistive two-fluid model instead of our kinetic one (both in cylindrical geometry). They also applied the code GPEC to compute the plasma response in toroidal geometry but used the magnitude of the perturbed field at the plasma edge together with transport coefficients from the code TRANSP for the nonlinear resistive evolution. Based on that, they computed what we called the *critical perturbation magnitude* (4.8) as a bifurcation criterion. Upon application on experimental shots on the DIII-D tokamak they came to a similar conclusion that bifurcated modes on top of the pedestal may be important for ELM suppression. Regarding the evolution of profiles their model is more advanced as it includes nonlinear evolution which we can only plan for the future. Regarding plasma response, we use a more complete model with the kinetic treatment.

Even though the results for the bifurcation threshold look promising, they must be taken with care. The study on the effect of different profiles has qualitatively shown that the result depends strongly on the form of the input profiles. Thus, only a big enough statistical basis, based on a variety of different shots and time slices can improve the confidence in our model.

The qualitative results of the effect of density and electron temperature scaling, show that there is a clear upper threshold in density for the bifurcation to occur. For the electron temperature the situation is more complicated but there is also an indication that an upper threshold exists. This is in agreement with [14], except for the overall shift in electron temperature caused by different profiles. The main reason for both, density and electron temperature dependence is something that still has to be found.

Although this thesis presented some improvements of the initial model in [21], there is still a lot of room for further sophistications. An even better estimation of the anomalous diffusion coefficient which takes the exact placement of heat by NBI and ECRH as well as a better distribution to ions and electrons is in progress. The effect of different profiles must be further investigated in detail, as well as the effect of different equilibria, which has not been included in this thesis. The used equilibria were of type EQH which were automatically calculated and thus lack of the overall features of the pedestal (knee in safety factor profile). The influence of using other, hand fitted equilibria must be studied. Finally, the calculation of parallel currents to account for toroidal geometry by GPEC could be replaced with a recently developed code at our institute [49]. This will give us the possibility to further improve our model, as this code can be fully integrated into the chain of computations.

Overall, the presented model in this thesis has shown that it correlates with experiment and that it can (with further refinement and verification) be used to find parameters in which ELM suppression is possible.

References

- [1] J. D. Lawson, *Proceedings of the Physical Society. Section B* **70**, 6, (<https://doi.org/10.1088/0370-1301/70/1/303>) (1957).
- [2] J. P. Freidberg, *Plasma Physics and Fusion Energy* (Cambridge University Press, 2007), ISBN: 978-0-521-85107-7.
- [3] M. Greenwald, *Plasma Physics and Controlled Fusion* **44**, R27, (<https://doi.org/10.1088/0741-3335/44/8/201>) (2002).
- [4] R. Aymar, P. Barabaschi, Y. Shimomura, *Plasma Physics and Controlled Fusion* **44**, 519, (<https://doi.org/10.1088/0741-3335/44/5/304>) (2002).
- [5] F. Wagner *et al.*, *Proceedings of the Physical Society. Section B* **49**, 1408, (<https://doi.org/10.1103/PhysRevLett.49.1408>) (1982).
- [6] J. Wesson, *Tokamaks* (Oxford University Press, Inc., New York, 1997), ISBN: 0-19-856293-4.
- [7] H. R. Wilson, *Fusion Science and Technology* **57 (Issue 2T)**, 174, (<https://doi.org/10.13182/FST10-A9408>) (2010).
- [8] A. Kallenbach *et al.*, *Nuclear Fusion* **48**, 085008, (<https://doi.org/10.1088/0029-5515/48/8/085008>) (2008).
- [9] A. Loarte *et al.*, *Physica Scripta* **2007 (T128)**, 222, (<https://doi.org/10.1088/0031-8949/2007/T128/043>) (2007).
- [10] T. C. Hender *et al.*, *Nuclear Fusion* **32**, 2091, (<https://doi.org/10.1088/0029-5515/32/12/I02>) (1992).
- [11] T. E. Evans *et al.*, *Physical Review Letters* **92**, 235003, (<https://doi.org/10.1103/PhysRevLett.92.235003>) (2004).
- [12] T. E. Evans *et al.*, *Nature Physics* **2**, 419, (<https://doi.org/10.1038/nphys312>) (2006).
- [13] W. Suttrop *et al.*, *Physical Review Letters* **106**, 225004, (<https://doi.org/10.1103/PhysRevLett.106.225004>) (2011).
- [14] W. Suttrop *et al.*, *Nuclear Fusion* **58**, 096031, (<https://doi.org/10.1088/1741-4326/aace93>) (2018).

- [15] R. Fitzpatrick, *Physics of Fluids B: Plasma Physics* **3**, 644, (<https://doi.org/10.1063/1.859863>) (1991).
- [16] A. H. Boozer, *Physics of Plasmas* **3**, 4620, (<https://doi.org/10.1063/1.871585>) (1996).
- [17] F. L. Waelbroeck, *Physics of Plasmas* **5**, 4040, (<https://doi.org/10.1063/1.1607324>) (2003).
- [18] R. Fitzpatrick, *Physics of Plasmas* **5**, 3325, (<https://doi.org/10.1063/1.873000>) (1998).
- [19] R. Nazikian *et al.*, *Physical Review Letters* **114**, 105002, (<https://doi.org/10.1103/PhysRevLett.114.105002>) (2015).
- [20] R. J. Goldston, P. H. Rutherford, *Introduction to Plasma Physics* (IOP Publishing Ltd, 1995), ISBN: 0-7503-0325-5.
- [21] M. F. Heyn *et al.*, *Nuclear Fusion* **54**, 064005, (<https://doi.org/10.1088/0029-5515/54/6/064005>) (2014).
- [22] M. Becoulet *et al.*, *Nuclear Fusion* **52**, 054003, (<https://doi.org/10.1088/0029-5515/52/5/054003>) (2012).
- [23] H. P. Furth, J. Killeen, M. N. Rosenbluth, *The Physics of Fluids* **6**, 459, (<https://doi.org/10.1063/1.1706761>) (1963).
- [24] J. P. Freidberg, *Ideal MHD* (Cambridge University Press, 2014), ISBN: 978-1-107-00625-6.
- [25] J. D. Huba, *NRL Plasma Formulary* (Naval Research Laboratory, 2016), (<https://www.nrl.navy.mil/ppd/content/nrl-plasma-formulary>).
- [26] W. D. D'haeseleer, W. N. G. Hitchon, J. D. Callen, J. L. Shohet, *Flux Coordinates and Magnetic Field Structure* (Springer-Verlag Berlin Heidelberg New York, 1991), ISBN: 3-540-52419-3.
- [27] H. P. Furth, P. H. Rutherford, H. Selberg, *The Physics of Fluids* **16**, 1054, (<https://doi.org/10.1063/1.1694467>) (1973).
- [28] A. H. Glasser, J. M. Greene, J. L. Johnson, *The Physics of Fluids* **18**, 875, (<https://doi.org/10.1063/1.861224>) (1975).
- [29] A. H. Glasser, J. M. Greene, J. L. Johnson, *The Physics of Fluids* **19**, 567, (<https://doi.org/10.1063/1.861490>) (1976).
- [30] P. H. Rutherford, *The Physics of Fluids* **16**, 1903, (<https://doi.org/10.1063/1.1694232>) (1973).
- [31] R. B. White, D. A. Monticello, M. N. Rosenbluth, B. V. Waddell, *The Physics of Fluids* **20**, 800, (<https://doi.org/10.1063/1.861939>) (1977).
- [32] T. S. Hahm, R. M. Kulsrud, *The Physics of Fluids* **28**, 2412, (<https://doi.org/10.1063/1.865247>) (1985).

- [33] R. Fitzpatrick, *Nuclear Fusion* **33**, 1049, (<https://doi.org/10.1088/0029-5515/33/7/I08>) (1993).
- [34] R. Carrera, R. D. Hazeltine, M. Kotschenreuther, *Physics of Fluid* **29**, 2617, (<https://doi.org/10.1063/1.865682>) (1986).
- [35] H. R. Wilson, *Fusion Science and Technology* **49 (Issue 2T)**, 155, (<https://doi.org/10.13182/FST06-A1115>) (2006).
- [36] R. B. White, *The Theory of TOROIDALLY CONFINED PLASMAS* (Imperial College Press, 2001), ISBN: 1-86094-277-6.
- [37] M. F. Heyn *et al.*, *Nuclear Fusion* **48**, 024005, (<https://doi.org/10.1088/0029-5515/48/2/024005>) (2008).
- [38] F. W. J. Oliver, D. W. Lozier, R. F. Boisvert, C. W. Clark, *NIST Handbook of Mathematical Functions* (Cambridge University Press, 2010), ISBN: 978-0-521-19225-5.
- [39] M. F. Heyn, I. B. Ivanov, S. V. Kasilov, W. Kernbichler, *Nuclear Fusion* **46**, 159, (<https://doi.org/10.1088/0029-5515/46/4/S07>) (2006).
- [40] I. B. Ivanov, M. F. Heyn, S. V. Kasilov, W. Kernbichler, *Physics of Plasmas* **18**, 022501, (<https://doi.org/10.1063/1.3551740>) (2011).
- [41] S. V. Kasilov, W. Kernbichler, A. F. Martitsch, H. Maassberg, M. F. Heyn, *Physics of Plasmas* **21**, 092506, (<https://doi.org/10.1063/1.4894479>) (2014).
- [42] J.-K. Park, A. H. Boozer, A. H. Glasser, *Physics of Plasmas* **14**, 052110, (<https://doi.org/10.1063/1.2732170>) (2007).
- [43] J.-K. Park *et al.*, *Physics of Plasmas* **16**, 056115, (<https://doi.org/10.1063/1.3122862>) (2009).
- [44] J.-K. Park, A. H. Boozer, J. E. Menard, S. P. Gerhardt, S. A. Sabbagh, *Physics of Plasmas* **16**, 082512, (<https://doi.org/10.1063/1.3206668>) (2009).
- [45] I. H. Hutchinson, *Principles of Plasma Diagnostics* (Cambridge University Press, 2002), ISBN: 978-0-521-80389-2.
- [46] A. F. Martitsch *et al.*, *Plasma Physics and Controlled Fusion* **58**, 074007, (<https://doi.org/10.1088/0741-3335/58/7/074007>) (2016).
- [47] W. Kernbichler *et al.*, *Plasma Physics and Controlled Fusion* **58**, 104001, (<https://doi.org/10.1088/0741-3335/58/10/104001>) (2016).
- [48] Q. M. Hu *et al.*, *Physics of Plasmas* **26**, 120702, (<https://doi.org/10.1063/1.5134767>) (2019).
- [49] P. Lainer, *Master's Thesis* (Graz University of Technology, Institute for Theoretical and Computational Physics, 2019).